MOLECULAR TOOLBOX FOR CHARACTERIZING, PREVENTING, AND TREATING HUMAN RESPIRATORY SYNCYTIAL VIRUS INFECTIONS

A Dissertation
Presented to
The Academic Faculty

By

Daryll Vanover

In Partial Fulfillment
Of the Requirements for the Degree
Doctor of Philosophy in Biomedical Engineering

Georgia Institute of Technology and Emory University

May 2018

MOLECULAR TOOLBOX FOR CHARACTERIZING, PREVENTING, AND TREATING HUMAN RESPIRATORY SYNCYTIAL VIRUS INFECTIONS

Approved by:

Dr. Philip Santangelo, Ph.D., Advisor
Department of Biomedical Engineering
Georgia Institute of Technology

Dr. Peng Xi, Ph.D.
Department of Biomedical Engineering
Georgia Institute of Technology

Dr. Krishnendu Roy, Ph.D.
Department of Biomedical Engineering
Georgia Institute of Technology

Dr. Elizabeth Wright, Ph.D.
Department of Pediatrics
Emory University

Dr. Brandon Dixon, Ph.D.
Department of Biomedical Engineering
Georgia Institute of Technology

Date Approved: March 29, 2018

ACKNOWLEDGEMENTS

This Ph.D. work would not have been possible without the support and guidance from other current and former members of the Santangelo lab. I would like to thank my advisor, Dr. Philip Santangelo, for all of his years of encouragement and mentorship throughout my undergraduate and graduate careers. I would like to acknowledge Dr. Chiara Zurla from the Santangelo lab, who has been there for me as a mentor and teacher since I joined the lab in 2010 as an undergraduate. I would like to recognize Dr. Aaron Lifland, a Santangelo Lab alumnus, for all of his assistance and mentorship before he graduated from the lab and for his more recent help with the Vutara imaging system. I would also like to thank all of my friends and family for their encouragement and support throughout all of these years. I would like to acknowledge Emmeline Blanchard, my partner in crime, who sat next to me and put up with my antics over the last several years. Specifically, I would like to recognize my grandmother, Margaret Conner, for her unconditional wisdom and love, and who will attend my commencement at 97 years of age. I want to thank my mother, Patty, and my father, Mark, who have unconditionally pushed and supported me throughout my life. Finally, I want to thank the love of my life - my wife, Christine - who was there to laugh or cry with me through all of this, and to whom this work is dedicated.

TABLE OF CONTENTS

LIST OF TABLES

LIST OF FIGURES

LIST OF SYMBOLS AND ABBREVIATIONS

AAV	Adeno-associated virus
aPali	Anchored palivizumab
ATCC	American Type Culture Collection
aVHH	Anchored variable domain of heavy chain antibody
C16	Imidazole-oxindole
CLEM	Correlated light and electron micrscopy
ConA	Concanavalin a
cryoEM	Cryo-electron microscopy
DAF	Decay accelerating factor
DAPI	4',6-diamidino-2-phenylindole
DMEM	Dulbecco's Modified Eagle Medium
DNA	Deoxyribonucleic acid
dSTORM	Direct stochastic optical reconstruction microscopy
EM	Electron microscopy
FBS	Fetal bovine serum
FDA	Food and Drug Administration
FPALM	Fluorescence Photoactivation Localization Microscopy
GFP	Green fluorescent protein
GPI	Glycosylphosphatidylinositol
HPA	*Helix pomatia* agglutinin
HPLC	High performance liquid chromatography
HBSS	Hank’s balanced salt solution
IACUC	Institutional Animal Care and Use Committee
IM	Intramuscular

IVT	*In vitro* transcribed
IFN	Interferon
MOI	Multiplicity of infection
MTRIP	Multiply labeled tetravalent RNA imaging probe
PBS	Phosphate buffered saline
PCR	Polymerase chain reaction
PEI	Polyethylenimine
PFA	Paraformaldehyde
PFU	Plaque forming units
PKR	Protein kinase R
PLA	Proximity ligation assay
PRR	Pattern recognition receptor
qRT-PCR	Quantitative real time polymerase chain reaction
rgRSV	Recombinant respiratory syncytial virus expressing GFP
RNA	Ribonucleic acid
RNP	Ribonucleoprotein
RSV	Respiratory syncytial virus
RSV F	Respiratory syncytial virus fusion protein
RSV G	Respiratory syncytial virus glycoprotein
RSV M	Respiratory syncytial virus matrix protein
RSV N	Respiratory syncytial virus nucleoprotein
SBA	Soybean agglutinin
sPali	Secreted palivizumab
STORM	Stochastic optical reconstruction microscopy
sVHH	Secreted variable domain of heavy chain antibody
TEM	Transmission electron microscopy

UTR	Untranslated region
WGA	Wheat germ agglutinin
VR	Viromer Red

SUMMARY

RSV remains one of the leading causes worldwide of acute lower respiratory tract infections. Despite continued effort, no vaccine exists and prophylaxis is limited to high-risk populations due to cost and limited efficacy of broadly neutralizing antibodies. Additionally, much of the general biology surround RSV replication and assembly is incomplete. The overall goal of the work presented here was to identify: 1) new targets for RSV therapeutics by analyzing RSV filament assembly (structures critical to high RSV titers), and 2) novel prophylactics against RSV to prevent infection. First, we developed a live-cell labeling method using a lectin, a class of proteins that bind specific glycan moieties, specific for RSV G. SBA was found to not inhibit the infectivity or replication of RSV by several metrics. We observed the first live images of RSV filament formation using this labeling technique, and critically, we found that this process can occur prior to the plasma membrane (where RSV was originally thought to assemble). This technique was then utilized to find that filament formation is microtubule and, specifically, dynein mediated. We also discovered that the loading of RSV genome into extended filaments is a microtubule-mediated process. We used synthetic, modified mRNA to express engineered broadly neutralizing antibodies to prevent RSV infection. We developed the use of both secreted and membrane-anchored palivizumab that prevents RSV infection *in vitro* and in the lungs of mice. We showed that encoding a membrane anchor on the antibodies prevents the antibody from diffusing away from the cell and blocks viral particles from entering the cell. Finally, the membrane-anchor was adapted to a highly potent RSV-neutralizing single-domain camelid antibody. The anchored VHH prevented RSV infection in mice and represents a promising new tool in the future of RSV prophylaxis.

CHAPTER 1

INTRODUCTION

Respiratory syncytial virus incidence and current therapeutics

Human respiratory syncytial virus (RSV) remains the leading cause of acute lower airway infections in children[1]. Annually, there are 33.1 million RSV cases globally in children under the age of 5, resulting in more than 3.2 million hospitalizations[1]. Despite the large worldwide burden of RSV, no effective vaccine yet exists[2].

To date, the only FDA-approved preventative therapeutic for RSV infection is Synagis produced by MedImmune, known formally as palivizumab. Palivizumab is a humanized monoclonal antibody that neutralizes RSV virion. Palivizumab is traditionally only given to immunocompromised children due to high cost, required monthly doses throughout the RSV season, and limited effectiveness. While palivizumab is fairly potent when used to inhibit RSV infection in animal models, it only reduced RSV hospitalization rate of infants of 29-32 week gestation from 5.0% to 3.1%[3,4]. The observed limited efficacy is likely due to the route of delivery of the antibody. Typically, palivizumab is delivered by intramuscular (IM) injection, and the antibody must diffuse into the bloodstream, travel to the lungs, and diffuse into the bronchoalveolar space before it can bind and inhibit RSV infection. The largest decrease in palivizumab concentration occurs in this last step, where the antibody must diffuse out of the bloodstream and into the airways of the lungs, with BAL titers dropping nearly 2000-fold from serum levels at 4 days post infection[5].

In immunocompromised individuals infected with RSV, Ribavirin, a purine analog, is the only FDA approved antiviral. A recent study indicated that oral delivery of Ribavirin is also effective, reducing cost and inconvenience[6]. However, in the vast majority of patients with RSV, only supportive care is given until the infection passes.

RSV taxonomy, structure, and life cycle

RSV belongs to the order *Mononegavirales*, family *Paramyxoviridae*, subfamily *Pneumovirinae*, and genus *Pneumovirus*; in humans, RSV is further subdivided into antigenic subgroups A and B. As such, the RSV virion has a pleomorphic morphology containing a non-segmented single-stranded negative-sense RNA genome. This genome contains 10 genes encoding for 11 proteins. These include the fusion glycoprotein (F), the major/attachment glycoprotein (G), the viroporin (SH), the nucleoprotein (N), the phosphoprotein (P), the RNA-dependent RNA polymerase (L), two nonstructural proteins (NS1 and NS2), the matrix protein (M), and two M2 variants that are alternate reading frames of the M2 gene (M2-1 and M2-2)[7].

RSV F is one of three encoded glycoproteins (alongside RSV G and SH) and is necessary for viral fusion with the cellular membrane and subsequent entry into host cells. Once virions are internalized, the RSV L, along with RSV N and P, transcribes viral genomic RNA into mRNA, which encode viral proteins. Viral transmembrane proteins are post-translationally glycosylated and transported by the secretory membrane system to the plasma membrane, where they interact with ribonucleoprotein (RNP) complexes consisting of RSV N, RSV P, potentially RSV M, and viral genomic RNA[8,9]. The virus then assembles into mature pleomorphic particles which are either spherical or filamentous[10,11].

RSV filament formation

Formation of RSV filaments, which contributes to higher viral titers, requires RSV F, RSV N, RSV P, and RSV M, potentially through their contribution to cell to cell spreading of the virus[12–15]. Several studies demonstrated that the RSV M dimerizes and binds to the cytoplasmic tail of RSV F, and thus plays a major role in the production of filamentous virions[16,17]. RSV M also appears to be responsible for the maturation and elongation of RSV filaments[18]. Additionally, RSV M has been shown to assemble into filamentous structures *in vitro*[19]. Even though there has been significant emphasis on the roles of RSV

F and M during filament formation, the steps leading to filament assembly are not clear. Some reports hypothesized that RSV might utilize a second maturation pathway, where virions bud into intracellular vesicles forming filaments, but these findings have not been confirmed or further investigated[20,21].

A variety of host-cell factors, particularly cytoskeleton components, have been implicated in RSV filament formation, however, our understanding of their mechanistic role is limited. Both ß-actin and actin-associated proteins were found in sucrose gradient-purified RSV preparations[22]. Additionally, actin was found to be primarily involved with virion egress, but has also been implicated in filament production[23,24]. Indeed inhibition of RhoA, an actin modulatory kinase, results in a shift to more spherical virion morphologies, and disruption of the actin network, which also leads to halting of RSV filament motion[13,25]. Microtubules have also been shown to play a key role in the assembly of progeny RSV[23]. In contrast, other groups have suggested that filaments can form independently of the host-cell cytoskeleton[12].

Current RSV filament imaging techniques

Previous studies have investigated the various viral and cellular components necessary generate viral filaments[10,12,17,18,26–28]. The majority of these studies completed their work in fixed cells and were unable to analyze the dynamics of filament assembly as it was occurring. To date, two studies of viral filament dynamics on live cells have been performed[25,26]. The imaging of RSV filament dynamics using molecular beacons by Santangelo *et al.* gave insight into the flexibility and motion of viral filaments, but only after they had formed[25]. Additionally, RSV filament formation was studied live on caveolar membranes, providing useful insights on the role of endocytic proteins in filament formation[26]. However, this imaging was performed indirectly using fluorescent caveolin as a marker for the filaments.

Rationale

Clearly, there exists a need for novel therapeutics to prevent and treat RSV. Therefore, the overarching goals of this thesis were to: 1) investigate the basic biology of RSV filament assembly, much of which is still unknown, and 2) engineer new therapeutics to prevent RSV infections. To accomplish these goals, three aims were originally proposed:

1. Characterize the mechanisms governing RSV filament formation by labeling RSV G with lectins in live infected cells.
2. Develop gold-conjugated lectins to enable high-resolution RSV G localization studies using cryo-electron microscopy (cryoEM).
3. Prevent the fusion of RSV in a murine model using intra-tracheal aerosol delivery of IVT mRNA encoding membrane-anchored neutralizing antibodies.

The work of this thesis completed the first and third aims (Chapters 2 and 3, respectively), and several steps were taken to complete the second aim, detailed in Chapter 4. First, conjugation of lectins to gold nanoparticles was checked with HPLC and darkfield imaging. Additionally, cryoEM necessitates a maximum sample thickness of 500-700 nm[29]. Because of this, cells must be plated very sparse, which can affect both cell and viral growth. To combat this, cell monolayers were infected for 24 h before being lifted into suspension using trypsin, and the infected cells were plated at lower confluency. Additionally, due to the strict maximum thickness requirement, thin cell lines (less than 500-700 nm thick on the edges of the cell) must be chosen for study using cryoEM. Because glycosylations can vary dramatically between different cell lines, the lectins used for study were assessed on Beas2B and A549 cells, both used extensively in RSV EM research[30]. Finally, if cryoEM is not feasible for any reason, direct stochastic optical

reconstruction microscopy (dSTORM), a super-resolution localization imaging technique, was tested as an alternative.

Imaging modalities

In this thesis, several imaging techniques were utilized which will be briefly described. The live-cell imaging performed in the studies presented here (and many of the fixed-cell experiments) was completed using a spinning disk confocal microscope. Spinning disk confocals afford a very fast frame rate with minimal out-of-focus light, but are still limited to, at best, 180 nm lateral and 500 nm axial resolution due to the diffraction of light[31]. To obtain sub-diffraction limited images of RSV in future work, we will turn to either EM (or cryoEM), or dSTORM. EM involves using a high-intensity electron beam (with a much smaller diffraction limit than visible light) as an illumination source, with electron-dense particles, such as gold, to enhance contrast. Because EM requires intact cellular ultrastructure, strong chemical fixatives are used in the staining process. These fixatives can alter structures and introduce artifacts that must be addressed when making biological conclusions[32]. CryoEM aims to eliminate these artifacts by flash freezing a biological sample to preserve the native structures, and can achieve resolutions on the order of single angstroms[33]. However, as mentioned previously, CryoEM has very strict requirements for cell thicknesses. Finally, dSTORM uses high power lasers alongside chemically modified buffers, which create an anoxic environment to deactivate and reactivate fluorophores[34]. The centroids of these individual “blinks” are then found, calculated, and the software reconstructs the image after several thousand frames are collected. This results in an improved axial resolution of approximately 20 nm over the 200 nm resolution of diffraction limited confocal microscopy.

Safety of therapeutic mRNA compared to virus and DNA

Several DNA based therapeutics have been evaluated in preclinical and clinical trials, however, thus far, no DNA based product has been approved for human use. There

are several contributing factors responsible for this delay, the most critical of which is safety. DNA is a pathogen associated molecular pattern that activates the innate immune response by triggering intracellular DNA pattern recognition receptors (PRRs), thereby initiating the interferon signaling pathway[35–38]. While mRNA therapeutics can also be sensed by endosomal and cytosolic PRRs, using chemically modified bases during the *in vitro* transcription process can mask the mRNA from these sensors. Use of DNA therapeutics also provokes concerns of integration into the host genome, and while this effect has been found to be minimal so far, potential integration must continue being monitored for each antigen expressed by the DNA[39,40]. Although single-stranded mRNA recombination is possible in rare circumstances, mRNA never interacts directly with the genome[41,42]. Additionally, studies indicate that anti-DNA antibodies are typically produced in response to vaccination by DNA, but are not expressed in sufficient quantity or duration to cause disease[43,44]. Finally, the vehicle used for nucleic acid delivery can invoke either an immune response or inflammatory toxicity or both[45–48]. While this effect is desirable in the case of vaccination against the encoded antigen, eliciting an immune response can inhibit expression of directly therapeutic proteins not intended to produce long-term immunity. Moreover, multiple studies have shown that detectable expression from naked mRNA is possible and that more protein is produced during peak expression than naked plasmid DNA[49–51].

One method of efficiently delivering nucleic acid based therapies is to use modified viruses. Although several viral families have been studied for gene therapy application, adeno-associated viruses (AAV) are the most prominent, in part due to being replication deficient and minimally pathogenic[52–54]. Microarray studies have shown that AAV vectors are weak activators of the innate immune system and do not invoke a strong type I interferon (IFN) response[55]. However, because AAV and other viral vectors do elicit an adaptive immune response against the virus, consecutive dosing is a nontrivial hurdle[56–

[58]. While the majority of vaccines are given through consecutive doses, a memory immune response against AAV would limit the ability to do so and not allow for other immunizations using AAV vectors. Additionally, since humans are a natural host for AAV, large portions of the population have neutralizing antibodies against subtypes of the virus: from 30 to 70% of the population in the case of AAV type 2 down to 15 to 35% of the population for AAV type 8[59,60]. While AAV vectors are efficient and safe delivery agents of nucleic acids, their use is limited to a single dose and they are ineffective for a large portion of the population that has pre-existing immunity.

As mentioned above, mRNA has several distinct advantages over DNA as a gene transfer modality. Specifically, mRNA expression is: 1) safer due to its transient expression and localization apart from the genome, 2) more rapid due to only needing to enter the cytosolic compartment before expression can begin, and 3) can often transfect cells that are difficult to transfect with DNA. However, cellular PRRs in the innate immune response system have adapted to detect exogenous mRNA as a response to microbial infection[61–64]. This detection can result in upregulation of proinflammatory cytokines and PKR (Protein kinase R) activation, which can lead to translational arrest and reduced protein expression[65]. The most common and, currently, efficient method of evading PRR activation is substituting one or more of the RNA bases for chemically modified nucleosides[66,67]. In our work, we linearize a plasmid DNA template encoding the mRNA sequence using restriction enzymes followed by IVT with a T7 mScript kit (Cellscript) and ATP, GTP, CTP, and N1-methyl-pseudouridine-5'-triphosphate (m1Y).

Rapid expression of mRNA delivered therapeutics

In addition to being safer than DNA for human therapeutic use, mRNA also produces protein faster than DNA[51,68]. This is predominately due to two factors: 1) DNA requires translocation into the nuclear envelope, which is an inefficient and slow process compared to cytosolic delivery, and 2) transcription is required before protein can be

produced from DNA, while mRNA can be translated as soon as it is presented in the cytosol.

Potential for simple, inexpensive, off-the-shelf protection

Live-attenuated and inactivated vaccines, as well as nanoparticles and lipoparticles, often require refrigeration or freezing for storage and transport. Naked nucleic acid therapeutics have no such limitation. Both DNA and mRNA can readily be lyophilized and shipped and stored at ambient temperature with minimal degradation, especially if kept under sealed anhydrous and anoxic conditions[69]. The therapeutic nucleic acid can then be briefly rehydrated in water before being delivered to the individual.

Previous applications of mRNA therapeutics in the lung

To date, expression of therapeutic proteins from mRNA in the lung has been used to treat a variety of diseases *in vivo*. First, expression of surfactant protein B (SP-B) in the lungs of congenital SP-B deficient mice increased hematocrit and survival rates in transfected mice[70]. However, the nature of mRNA means that this protein expression is only transient, and as such using mRNA to encode congenital deficiencies is not a long-term solution. To combat this, researchers have used mRNA to transiently express site-specific nucleases to alter the genome of transfected cells in the lungs of SP-B deficient mice, prolonging their life[71]. Additionally, therapeutic proteins to successfully alleviate allergic responses have also been delivered by aerosolized mRNA into the lungs of mice[72]. Together, these studies demonstrate that mRNA expression of therapeutic proteins in the lungs is both feasible and successful in treating disease in mice.

CHAPTER 2

STUDY THE MECHANISMS GOVERNING RSV FILAMENT FORMATION BY LABELING RSV G WITH LECTINS IN INFECTED CELLS

The work presented here is from Vanover D, Smith DV, Blanchard EL, Alonas E, Kirschman JL, Lifland AW, Zurla C, Santangelo PJ. **"**RSV glycoprotein and genomic RNA dynamics reveal filament assembly prior to the plasma membrane." *Nature Communications* (2017, doi:10.1038/s41467-017-00732-z).

Background

Respiratory syncytial virus (RSV) remains the leading cause of acute lower respiratory infections worldwide in children under five years of age and leads to roughly 3 million hospital admissions each year[73]. Despite the high global incidence rate of infected patients, no effective vaccine yet exists[2]. While various treatments are being actively investigated, the cellular events that occur during RSV assembly are poorly understood.

RSV is a member of the *Paramyxoviridae* family and contains a single-stranded negative-sense RNA genome that encodes for 11 proteins. The RSV fusion protein (RSV F) is one of three encoded glycoproteins and is necessary for viral fusion with the cellular membrane and subsequent entry into host cells. Once virions are intracellular, the large (RSV L) polymerase, working with the RSV nucleoprotein (RSV N), and phosphoprotein (RSV P), transcribes viral genomic RNA into mRNA, which encode viral proteins . Viral transmembrane proteins are post-translationally glycosylated and transported by the secretory membrane system to the plasma membrane, where they interact with ribonucleoprotein (RNP) complexes consisting of RSV N, RSV P, potentially RSV matrix protein (RSV M), a structural protein, and viral genomic RNA[8,9]. The virus then assembles into mature pleomorphic particles which are either spherical or filamentous[10,11]. Formation of these filaments requires RSV F, RSV N, RSV P, and RSV M, and has been found to

contribute to higher viral titers, potentially through their contribution to cell to cell spreading of the virus[12–15]. Some reports hypothesized that RSV might utilize a second maturation pathway, where virions bud into intracellular vesicles forming filaments, but these findings have not been confirmed or further investigated[20,21]. Several studies demonstrated that the RSV M dimerizes and binds to the cytoplasmic tail of RSV F, and thus plays a major role in the production of filamentous virions[16,17]. RSV M also appears to be responsible for the maturation and elongation of RSV filaments[18]. Additionally, RSV M has been shown to assemble into filamentous structures *in vitro*[19]. Even though there has been significant emphasis on the roles of RSV F and M during filament formation, the steps leading to filament assembly are not clear.

A variety of host-cell factors, particularly cytoskeleton components, and viral proteins have been implicated in RSV filament formation, however our understanding of their mechanistic role is limited. Both ß-actin and actin-associated proteins were found in sucrose gradient-purified RSV preparations[22]. Additionally, actin was found to be primarily involved with virion egress, but has also been implicated in filament production[23,24]. Indeed, inhibition of RhoA, an actin modulatory kinase, results in a shift to more spherical virion morphologies, and disruption of the actin network, which also leads to halting of RSV filament motion[13,25]. Microtubules have also been shown to play a key role in the assembly of progeny RSV[23]. In contrast, other groups have suggested that filaments can form independently of the host-cell cytoskeleton[12].

The viral G protein is a highly glycosylated 90 kDa transmembrane protein, primarily responsible for the attachment of RSV to the host cell [74–76]. Though not required for the production of infectious RSV or virus-like particles, RSV G is necessary for full infectivity and is found on the membrane of mature filaments [21,77,78]. Additionally, RSV G interacts with both RSV M and F protein, which appears to be required for complete virion assembly [79,80]. During initial virus entry, RSV glycoproteins have been shown to internalize

via clathrin-mediated endocytosis, whereas caveolin is heavily incorporated into the envelope of mature RSV filaments [26,81–83]. RSV G was also found to be cleaved in the Vero cell line during endosomal recycling, and has been implicated in the maturation and egress of RSV[8,10,82,84] . While the RSV G glycoprotein is found within progeny viral filaments and is clearly essential for virion entry into host cells, little data exists on the dynamics or trafficking of RSV G during infection, due to a lack of available reagents for tracking RSV G in live cells[85].

Previously, we have demonstrated the use of single molecule sensitive RNA probes for imaging RSV viral genomic RNA in live cells, but the lack of a method for tracking the viral transmembrane proteins precluded our ability to image viral particle formation. In order to target the G protein, we investigated the use of the lectin soybean agglutinin (SBA) for specific labeling of RSV G, and found that SBA binding did not affect RSV infectivity, replication, or formation of viral filaments. Using fluorescently-conjugated SBA, we report here that membrane bound RSV G recycles from the plasma membrane via clathrin-mediated endocytosis into vesicles. We also show that these recycling endocytic vesicles merge with intracellular vesicles containing viral genomic RNPs and eventually associate with caveolin before returning to the plasma membrane. To the best of our knowledge, this is the first live imaging of a wild-type RSV viral protein (RSV G) and genomic RNA during RSV filament formation which revealed: the dynamics of filament formation, the production of branched filamentous structures typical of late-stage infections, the importance of microtubules in the assembly and loading of these filamentous structures in the cytosol, and the halting of this rapid motion once these structures merge with the plasma membrane. Together, these results change our understanding of RSV filament assembly and loading prior to the membrane and open new avenues for research and RSV therapeutics.

Fluorescent SBA conjugates specifically bind RSV G

RSV G was previously found to contain N-acetylgalactosamine (GalNAc) side chains, which interact specifically with various lectins[86]. We first analyzed the localization of Alexa Fluor 488 conjugated SBA (SBA-488) in cells infected with the A2 strain of human RSV with respect to RSV G and RSV F. Immediately prior to infection, SBA was delivered to cells at 4 °C, in order to minimize non-receptor mediated endocytosis. Upon infection for 24 hours, both RSV G and RSV F colocalized with SBA-488, with minimal background in mock-infected controls (Figure 2.1A). In addition, the SBA-488 signal in both the membrane and filaments was higher in infected cells than in control cells (Figure 2.1B), which indicated that a large portion of glycoprotein was present in the membrane (Figure 2.1A). Due to previous reports describing the binding of RSV F and RSV G in solution, we opted to examine a reduced system, using microscopy and expression of individual viral proteins, instead of an immunoprecipitation assay to demonstrate the specificity of SBA for RSV G[87]. Vero cells were transfected with *in vitro* transcribed (IVT), modified mRNA that encodes for either RSV F or RSV G[88]. We then labeled the cells with SBA-488 before fixing and immunostaining, without permeabilization, for RSV F and G (Figure 2.1C). While transfection with RSV F did not alter background SBA staining, cells transfected with RSV G showed a marked increase in SBA staining relative to untransfected control cells, due to the heavy glycosylation of the RSV G protein. SBA colocalized in cells transfected with RSV G and not with RSV F, as indicated by both the Pearson's correlation coefficient and Mander's colocalization coefficient (Figure 2.1D). A Pearson's correlation value much greater than 0 indicates a significant positive correlation between RSV G and SBA. The significantly higher Mander's coefficient indicates that a much larger percentage of the RSV G signal contains SBA signal, while very little of the RSV F signal contains SBA. The expressed RSV G and RSV F both localized to the plasma membrane, evidenced by the distribution of the viral proteins across the cell

(Figure 2.1C) and by the layer of protein occupying a higher imaging plane than the nuclei of the cells (Figure 2.1E). Overall, these results indicate that SBA can be used to specifically label RSV G, supporting previous lectin-binding studies to RSV glycoproteins[86].

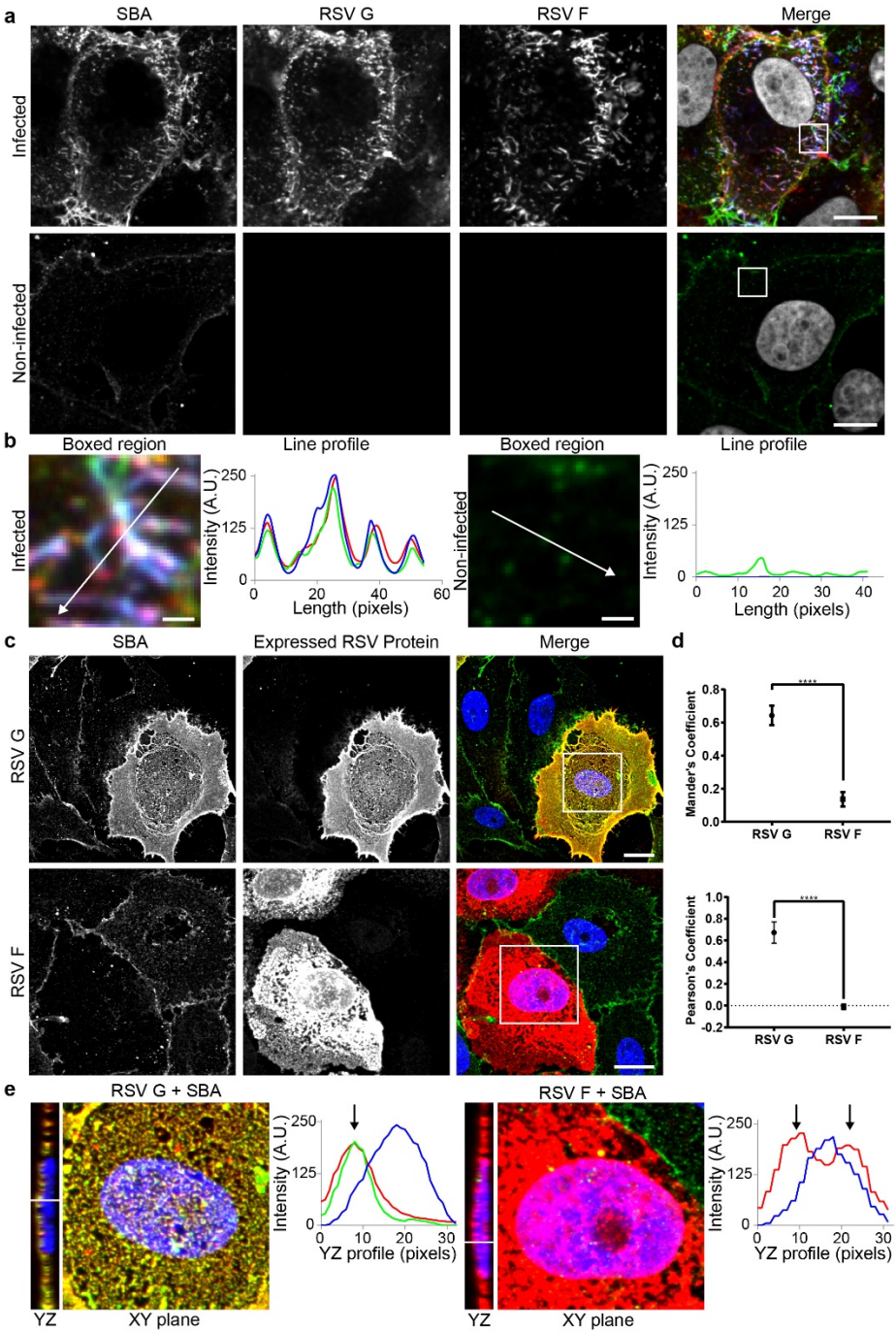

Figure 2.1. SBA selectively binds RSV G. (A) Vero cells infected (top) or mock-infected (bottom) for 24 h with RSV A2 at an MOI of 1 were labeled with SBA-488 at 4 ºC (green) before being fixed and stained for RSV G (red), RSV F (blue), and nuclei (gray). Extended focus image is shown. Scale bar represents 10 µm. **(B)** Enlarged cropped images from the white boxed regions from part **(A)** with intensity profiles showing colocalization along the direction of the white arrow. Scale bar represents 1 µm. **(C)** Cells transfected for 24 h with RSV G (top) and RSV F (bottom) mRNA were labeled with SBA-488 at 4 ºC (green) before being fixed and stained without permeabilization for RSV G or RSV F (red) and nuclei (gray). Extended focus image is shown. Scale bar represents 15 µm. **(D)** Mander's colocalization coefficient and Pearson's correlation between RSV G or RSV F and SBA.

Dotted line indicates 0 correlation. *n*=16 cells per group. Error bars represent 95% confidence interval. Asterisks indicates p<0.0001 by Mann-Whitney U Test. **(E)** Enlarged cropped images from the white boxed regions from part **(C)** with YZ cross-sections (left). Intensity profiles, indicated by the white line on the YZ cross-section, show the expressed RSV protein on a higher plane than the nucleus as indicated by the arrow. Extended focus cropped images are shown.

SBA conjugates do not inhibit replication of RSV

We subsequently verified that SBA does not alter RSV replication or infectivity. First, we labeled RSV A2 virus stocks with SBA-488. Then, we isolated the filamentous and spherical viral particles and deposited them onto glass coverslips as described previously [11]. Using fluorescence imaging and colocalization analysis, we verified that SBA was bound to both filamentous and spherical particles, which also contained RSV F and RSV N (Figure 2.2A). Note that RSV infected cells generate incomplete and complete virions, as indicated by particles that contain only some of the various viral proteins[11]. To demonstrate that labeling RSV A2 with SBA-488 did not significantly inhibit viral replication, we infected cells for 24 h and stained for RSV F and RSV N (Figure 2.2B). Both cytosolic IBs and viral filaments were found, indicative of late-stage infections.

We then sought to determine the effect of SBA-labeled RSV A2 on virus infectivity. First, we bound SBA to RSV A2, similarly to assays described previously[89]. We then infected cells and measured RSV G protein synthesis relative to unlabeled RSV A2 after 12 and 24 hours via western blot (Figure 2.2C). Both the untreated and SBA-treated lysates contained similar amounts of RSV G at both time points. We quantified the amounts of protein using densitometry, and found that the differences at either time point were not statistically significant (Figure 2.2D). To further test whether SBA affects RSV infectivity, we incubated RSV virus modified to express recombinant green fluorescent protein (rgRSV-GFP) with either palivizumab or SBA and measured GFP signal via flow cytometry[90,91]. Because rgRSV-GFP has reduced permissivity compared to RSV A2, we allowed the infection to proceed for 48 h, before assaying the cells for GFP signal. SBA-labeled rgRSV-GFP or unlabeled virus infected a similar percentage of cells, while palivizumab-labeled virus abrogated any productive infection (Figure 2.2E). Last, we compared via qRT-PCR the levels of RSV N and G mRNA at 6, 12, and 24 h post-infection

(hpi) with SBA-labeled RSV and unlabeled RSV, and found no statistically significant differences (Figure 2.2F).

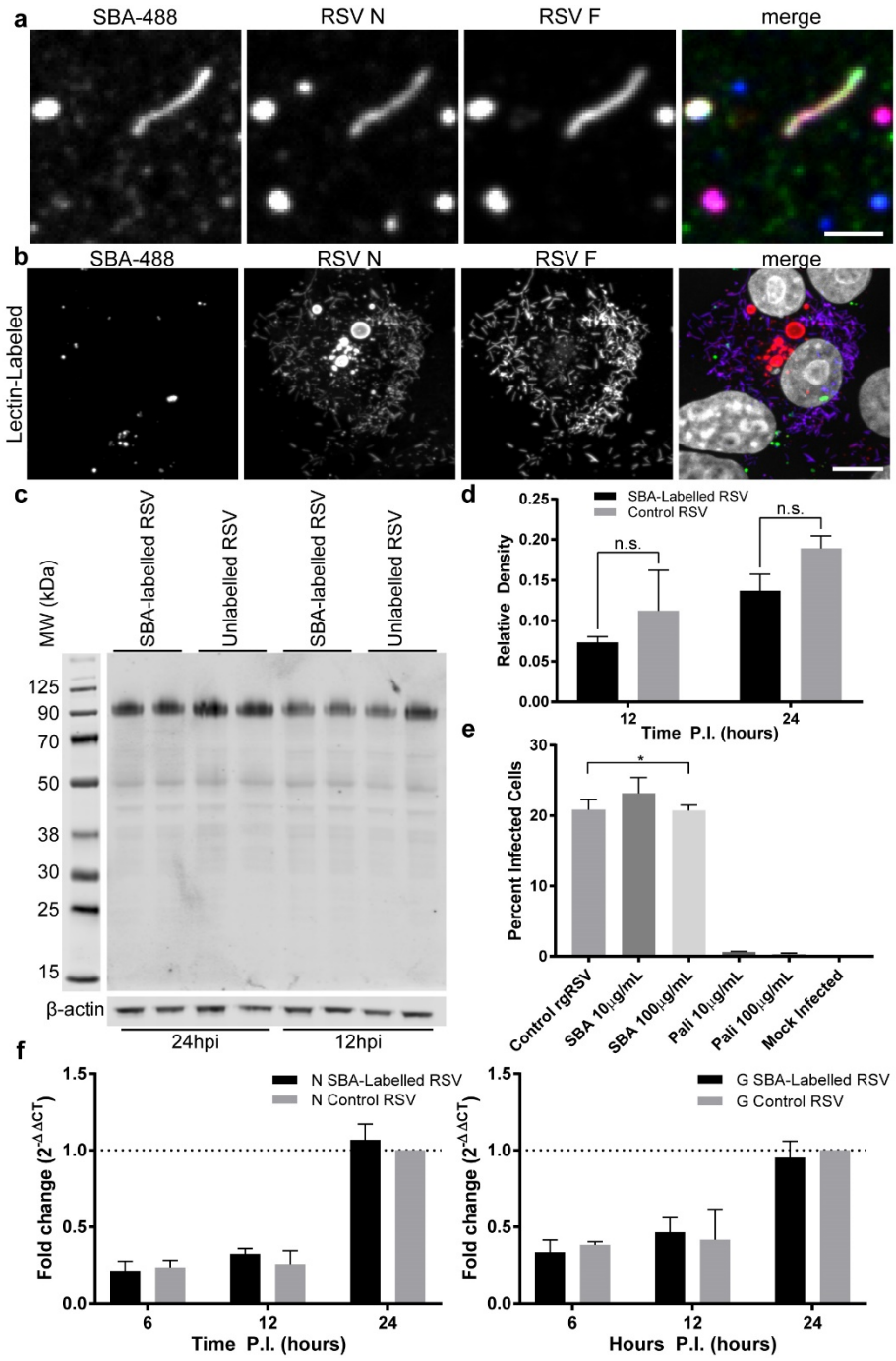

Figure 2.2. SBA binding does not inhibit RSV binding or replication. (A) SBA-488 (green) was incubated with RSV A2 stocks for 30 min before filaments were isolated onto glass coverslips. Isolated virions were fixed and stained for RSV N (red) and RSV F (blue). Scale bar represents 2 μm. **(B)** SBA-488 labeled virus (green) was used to inoculate Vero cells at an MOI of 1. At 24 hpi, cells were fixed and immunostained for RSV N (red), RSV F (blue), and nuclei (gray). Scale bar represents 10 μm. **(C)** RSV A2 was incubated with either SBA or vehicle control for 2 h at 37 ºC. Virus was then used to inoculate Vero cells at an MOI of 1. At 12 or 24 hpi, cells were lysed, and lysates were assayed by western

blotting for RSV G. ß-actin is included as a loading control. Image is representative of two independent experiments. **(D)** Replicate lanes were quantified by densitometry to compare the amount of RSV G signal from SBA-labeled or unlabeled RSV infections. There were no statistically significant differences at either time point (two-way ANOVA, $p>0.05$). **(E)** rgRSV-GFP was incubated with the indicated concentrations of either palivizumab, SBA, or vehicle control for 2 h at 37 ºC. Virus treatments and a mock treatment were then used to inoculate Vero cells at an MOI of 1. At 48hpi cells were lifted into a single-cell suspension and analyzed by flow cytometry. Data represents the mean percentage of infected cells in three independent experiments. Error bars represent standard deviation. Asterisk indicates significanct difference versus mock infection (one-way ANOVA on ranks, $p<0.05$). **(F)** Relative quantity of RSV N (left) and RSV G (right) expression via qRT-PCR upon infection of Vero cells with SBA-labeled or unlabeled RSV A2 at an MOI of 1 at 6, 12, and 24 hpi. There was no statistically significant difference at any time point (two-way ANOVA, $p>0.05$).

SBA labels RSV G without inhibiting viral protein production

Since SBA does not significantly impair the replication or infectivity of RSV A2 when bound to virions prior to infection, we next sought to investigate if we could label RSV G on cells with SBA during an infection, without impairing viral processes. Because the majority of filaments are produced between 12 and 24 hpi, we incubated RSV infected cells with SBA-488 or vehicle control 12 hours hpi and allowed the cells to incubate a further 12 hours before fixation. Cells were then stained for RSV N and RSV F (Figure 2.3A). Labeling of RSV G with SBA-488 12 hpi was specific, and especially stained viral filaments in infected cells with minimal background (Figure 2.3B).

We then verified that labeling of RSV G with SBA-488 12 hpi in live cells was not altering the amount of RSV G present in filamentous virions. To do this, we stained live, RSV infected cells with SBA-488 or vehicle control at 12 hpi, and harvested the virus at 24 hpi. Then we isolated viral filaments and deposited them onto glass and immunostained for RSV F and RSV G (Figure 2.3C). The amount of RSV G per filament was similar in SBA labeled and unlabeled RSV virions (Figure 2.3D). Finally, we verified that labeling RSV infected cells with SBA did not inhibit the release of progeny virions. We stained RSV infected cells with either SBA or vehicle control at 12 hpi, isolated the supernatant at 24 hpi, and measured the titer by plaque assay (Figure 2.3E). There was no statistically significant difference between viral titers from SBA labeled and unlabeled RSV infected cells. Overall these results indicated that SBA can be utilized to specifically label RSV G in live cells without altering viral protein expression and localization.

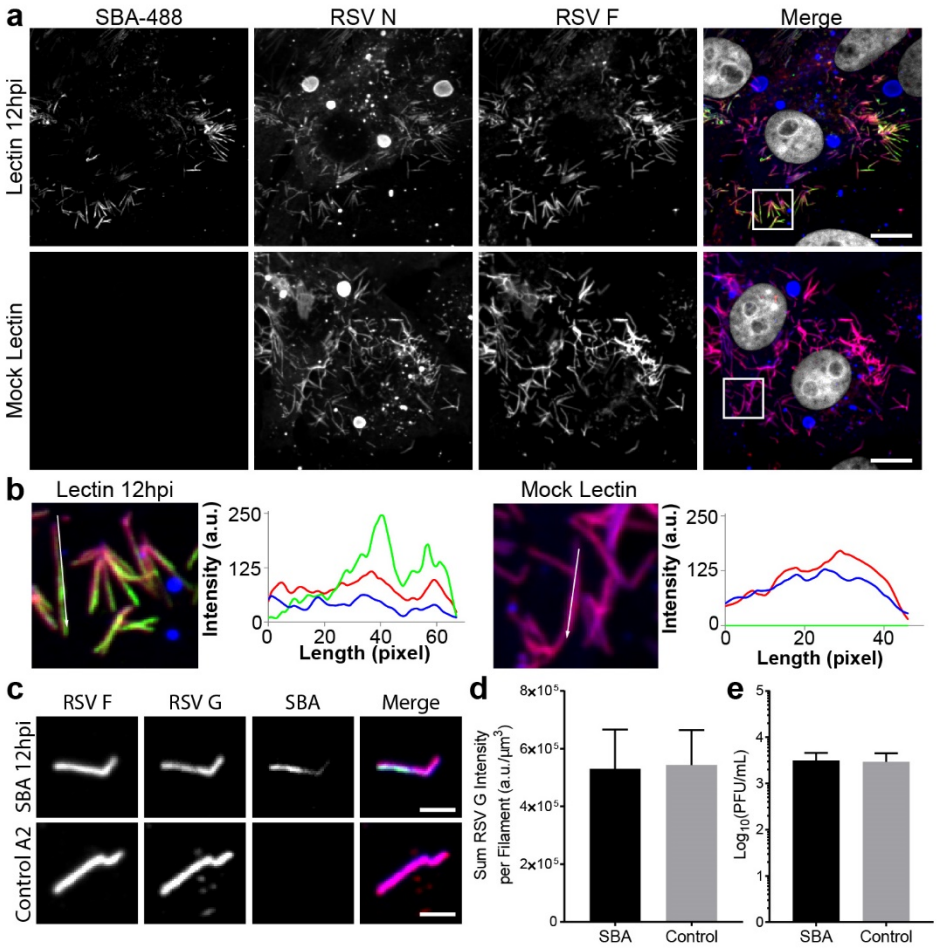

Figure 2.3. SBA allows for the visualization of RSV G dynamics in RSV infected cells. (A) Vero cells were infected with RSV A2 at an MOI of 1. At 12 hpi, cells were stained live with SBA-488 (top) or vehicle control (bottom), washed, and further incubated in complete growth media. 24 hpi, cells were fixed and immunostained for RSV N (blue), RSV F (red), and nuclei (gray). Scale bar represents 10 μm. **(B)** Enlarged cropped images from the white boxed regions from part **(A)** with intensity profiles showing colocalization along the direction of the white arrow. **(C)** Vero cells were infected with RSV A2 at an MOI of 1. 12 hpi, cells were stained live with SBA-488 (top, green) or vehicle control (bottom), washed, and further incubated in complete growth media. 24 hpi, virus was harvested. Filaments were isolated onto glass and stained for RSV F (blue) and RSV G (red) Scale bar represents 2 μm. **(D)** Mean sum of RSV G intensity per filament was quantified. 50 isolated virions were analyzed for each condition. Error bars represent standard deviation. There was no statistically significant difference between SBA-labeled and unlabeled RSV (Mann-Whitney U test, $p>0.05$). **(E)** Vero cells were infected with RSV A2 at an MOI of 1. 12 hpi, cells were stained live with SBA-488 or vehicle control, washed, and further incubated in complete growth media. 24 hpi, supernatants from single infected wells were titered by plaque assay in quadruplicate. Three wells were independently infected, stained, and assayed per treatment. Error bars represent standard deviation. There was no statistically significant difference between SBA-labeled and unlabeled RSV (Mann-Whitney U test, $p>0.05$).

RSV G recycles from the plasma membrane

To label the majority of the RSV G present during an RSV A2 infection, SBA-488 was delivered in three doses at 12, 18, and 24 hpi to the same cells before fixation 24 hpi and immunostaining for RSV F. RSV G was found in viral filaments, as expected, as well as in intracellular vesicles, both of which colocalized with RSV F (Fig. 4a). We then performed a similar experiment and delivered an Alexa Fluor 647 conjugated SBA (SBA-647) to infected cells 12 hpi first, and then, SBA-488 at 24 hpi prior to fixation and immunostaining for RSV F (Figure 2.4A). As expected, SBA labeled RSV G was found in viral filaments in both sets of cells, regardless of when it was delivered. RSV G labeled with SBA-647 delivered 12 hpi was found in intracellular vesicles rich in RSV F. Interestingly, RSV G labeled with SBA-488 delivered 24 hpi appeared in vesicles that do not colocalize with either RSV F or SBA-647 labeled RSV G. This finding suggested that RSV G is involved in a complex recycling mechanism where membrane-bound RSV G is first internalized and subsequently incorporated into viral filaments protruding from the surface. To confirm this, we delivered SBA-488 to live RSV A2 infected cells 12 hpi and immediately began imaging every 10 minutes (Figure 2.4B). Compared to the initial time-point, we observed a dramatic reduction of SBA-488 staining on the surface of the cell, and a marked increase in the brightness and number of intracellular vesicles over a period of 1 hour. This demonstrated that RSV G is rapidly endocytosed into intracellular vesicles. Together, these data indicated that membrane bound RSV G recycles from the plasma membrane into intracellular vesicles *before* being incorporated into viral filaments.

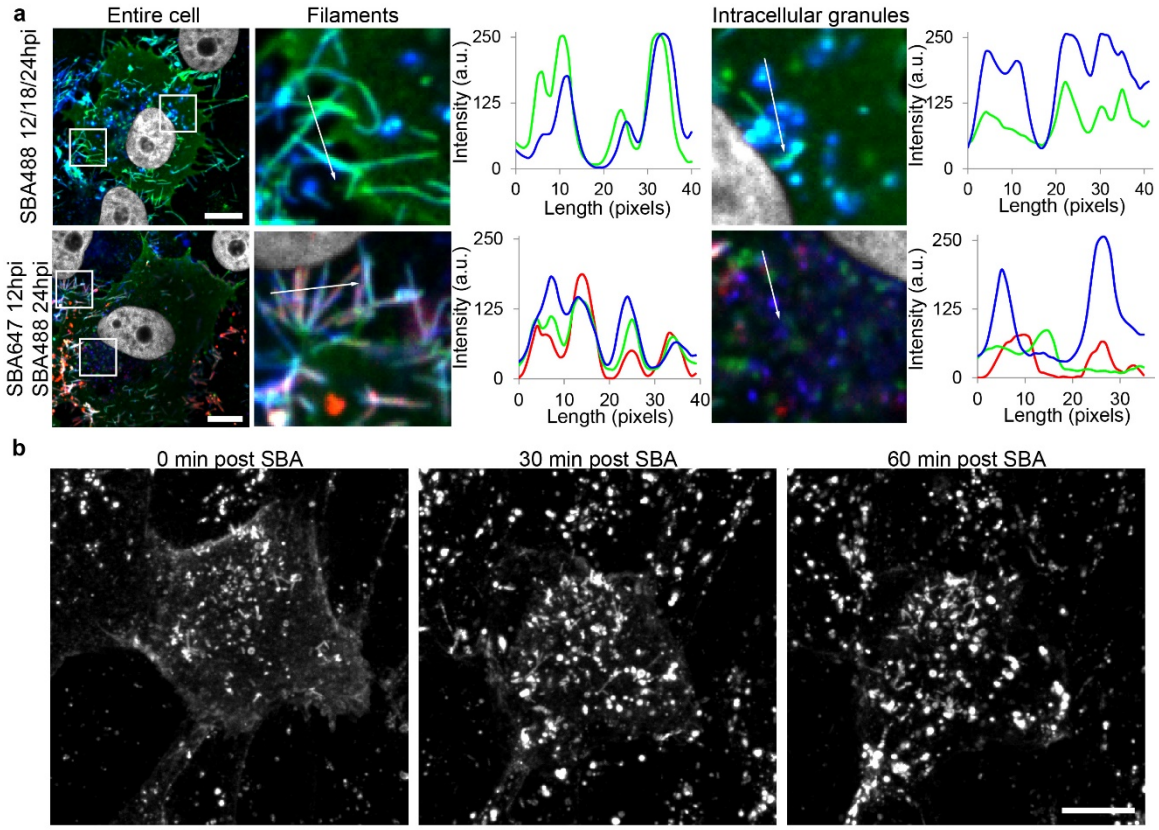

Figure 2.4. RSV G recycles from the plasma membrane into intracellular vesicles. **(A)** Vero cells were infected with RSV A2 at an MOI of 1. Cells were either labeled with SBA-488 (green) at 12, 18, and 24 hpi (top) or with SBA-647 (red) at 12 hpi and SBA-488 at 24 hpi. Cells were then fixed and stained for RSV F (blue). Enlargements of cropped images of either filaments or intracellular vesicles from the white boxed regions with intensity profiles showing colocalization along the direction of the white arrow. Scale bar represents 10 μm. **(B)** Vero cells were infected with RSV for 12 hpi before being labeled with SBA-488 (green). Immediately following SBA delivery, cells were imaged live over 1 h. Extended focus images shown. Scale bars represent 10 μm.

RSV G-containing vesicles may switch from clathrin to caveolin

We aimed to determine the mechanism by which RSV G recycles into the cell from the plasma membrane. We delivered SBA-488 to infected cells 12 hpi, fixed the cells 0, 10, 30, and 60 min after delivery, and immunostained for clathrin heavy chain (CHC) (Figure 2.5A). We found that RSV G localized to the membrane immediately post-delivery, colocalized highly with CHC 10 minutes post-delivery and appeared to be released from clathrin coated vesicles 30 to 60 minutes after delivery (Figure 2.5B). Both the Pearson's correlation and Mander's coefficient for SBA-488/CHC confirmed these observations (Figure 2.5C). This indicated that RSV G is internalized from the membrane through the clathrin endocytic system. We confirmed these results using chlorpromazine, a potent clathrin-mediated endocytosis inhibitor. We incubated RSV infected cells 12 hpi with media containing chlorpromazine for 2 hours. We then labeled RSV G with SBA-488 and incubated the cells an additional hour before fixing and staining for CHC (Figure 2.5D). In chlorpromazine treated cells, RSV G was found in large intracellular granules that did not colocalize with CHC (Figure 2.5D). These results were confirmed with Mander's colocalization analysis (Figure 2.5E). Finally, we labeled RSV G in infected cells 24 hpi before fixing and staining for caveolin and found high colocalization between RSV G and caveolin on viral filaments (Figure 2. 5F). Together, these data indicated that RSV G recycles into cells via clathrin-mediated endocytosis and over time, colocalizes with caveolin-coated vesicles during the filament formation process.

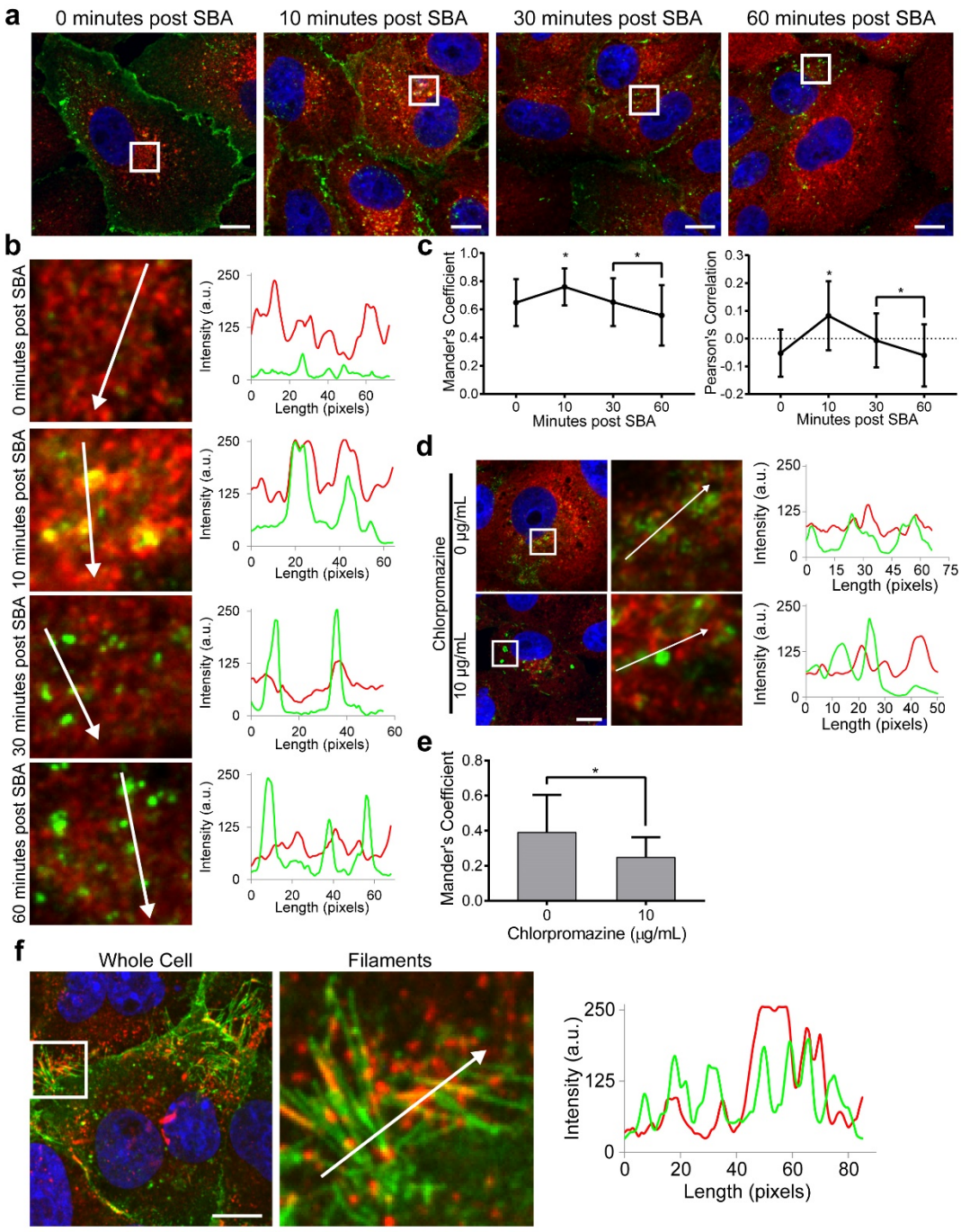

Figure 2.5. RSV G protein internalizes via clathrin and colocalizes with caveolin in viral filaments. (A) RSV infected Vero cells were stained for RSV G with SBA-488 (green). The cells were incubated at 37 ºC before being fixed and stained for CHC at the indicated time points (red). The cell nuclei were stained with DAPI (blue). Scale bar represents 10 µm. **(B)** Enlargements of cropped images from the white boxed regions in part **(A)** with intensity profiles showing colocalization along the direction of the white arrow. **(C)** Mander's colocalization coefficient and Pearson's correlation between RSV G and CHC. Dotted line indicates 0 correlation. Error bars represent standard deviation. Asterisk indicates $p<0.05$ (Mann-Whitney U test). **(D)** Infected Vero cells at 12 hpi were treated

with the indicated concentration of chlorpromazine in media for 2 hours. RSV G was labeled with SBA-488 at 4 ºC followed by a 1 h incubation at 37 ºC in media with drug. Cells were fixed and stained for CHC. Scale bar represents 10 μm. Enlargements of cropped images from the white boxed regions with intensity profiles showing colocalization along the direction of the white arrow. **(E)** Mander's colocalization coefficient between RSV G and CHC. Error bars represent standard deviation. Asterisk indicates $p<0.05$ (Mann-Whitney U test) **(F)** Vero cells were infected with RSV A2 at on MOI of 1. At 24 hpi, RSV G was labeled with SBA-488 (green) and cells were fixed and stained for caveolin (red) and nuclei (blue). Enlargement of cropped image from the white boxed region with an intensity profile showing colocalization along the direction of the white arrow. Scale bar represents 10 μm.

RSV filaments are formed via rapid vesicular distension

Next, we examined the dynamics of filament formation in living cells. We infected cells with RSV A2 and labeled RSV G with SBA-488 16hpi. After 1 h, cells were imaged live at the maximum speed of our spinning disk confocal system (Figure 2.6A). Surprisingly, we found that some of the vesicles were distending and retracting into long filament-like structures. Additionally, we noticed that some of these structures appeared to branch, as has been observed previously for RSV filaments[27]. To determine the speed of these events, we measured their length across individual movie frames and found that both the lengthening and shortening of the structures occurred at a speed ≥ 2 μm/s (Figure 2.6B). To ascertain whether these structures were viral filaments, we fixed the sample immediately after imaging and demonstrated colocalization for RSV F with SBA-488 (Figure 2.7). To examine the motion of the filaments associated to vesicles, we infected cells with RSV A2 for 12 h before labeling RSV G with SBA-488. After 1 hour, cells were imaged live every 10 minutes for 12 hours (Figure 2.6C; Figure 2.8). As expected, we found that RSV filaments extended rapidly from vesicles within a single frame. Furthermore, some of these filaments persisted for a long period of time, suggesting that they had matured from the vesicular extension and retraction phase. These results indicated that RSV filaments are formed by a rapid extension/retraction process of intracellular vesicles before reaching the plasma membrane.

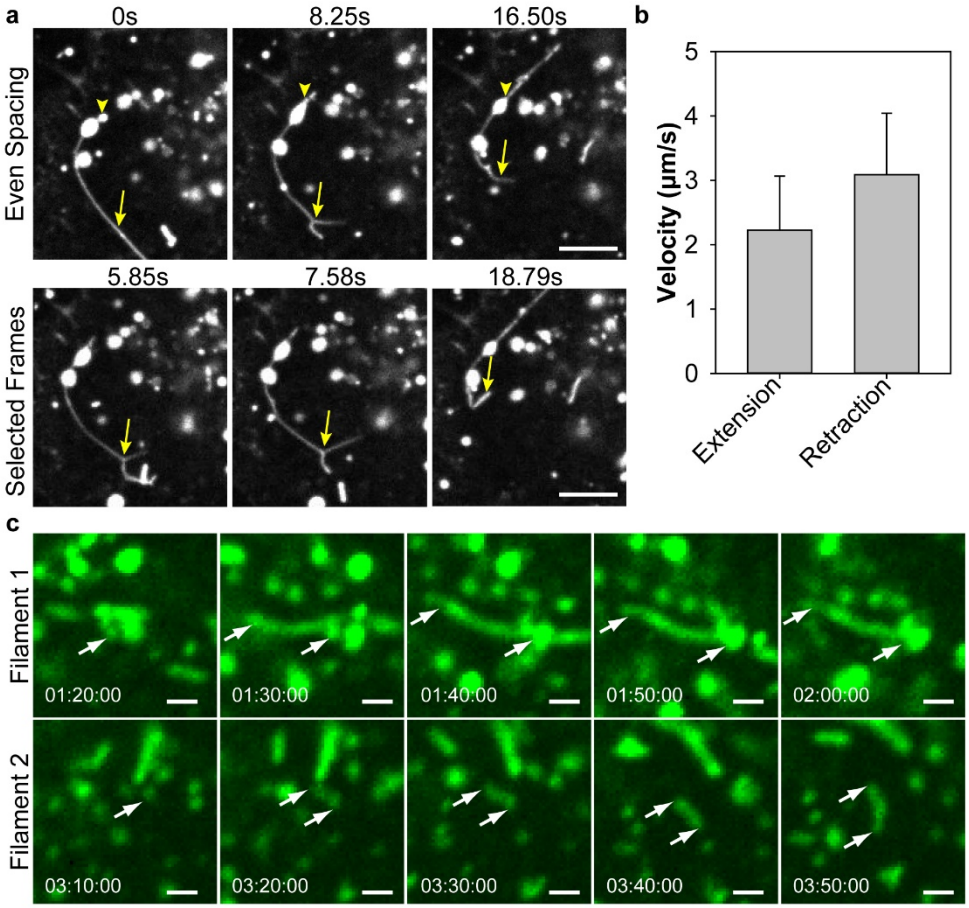

Figure 2.6. RSV filaments are formed by a rapid vesicular extension and retraction motion. (A) Vero cells were infected with RSV A2 at an MOI of 1. At 16 hpi, SBA-488 was delivered and allowed to internalize for an hour. Cells were then imaged live at 12.13 Hz. Time series are shown with either even temporal spacing (top) or as selected frames from the movie (bottom). Yellow arrowheads indicate distension of vesicles, while arrows indicate extended filaments and branched filaments. Scale bar represents 5 µm. **(B)** Individual extension and retraction events were analyzed by hand on a frame-by-frame basis to determine the mean velocity. 30 events of each type were analyzed. Error bars represent standard deviation. **(C)** Vero cells were infected with RSV A2 at an MOI of 1. After 12 h, SBA-488 (green) was delivered to the cells and allowed to internalize for 1 h before being imaged every 10 minutes. Cropped regions of two individual filaments are shown. Yellow arrows mark the two apparent ends of the filaments. Scale bars represent 1 µm.

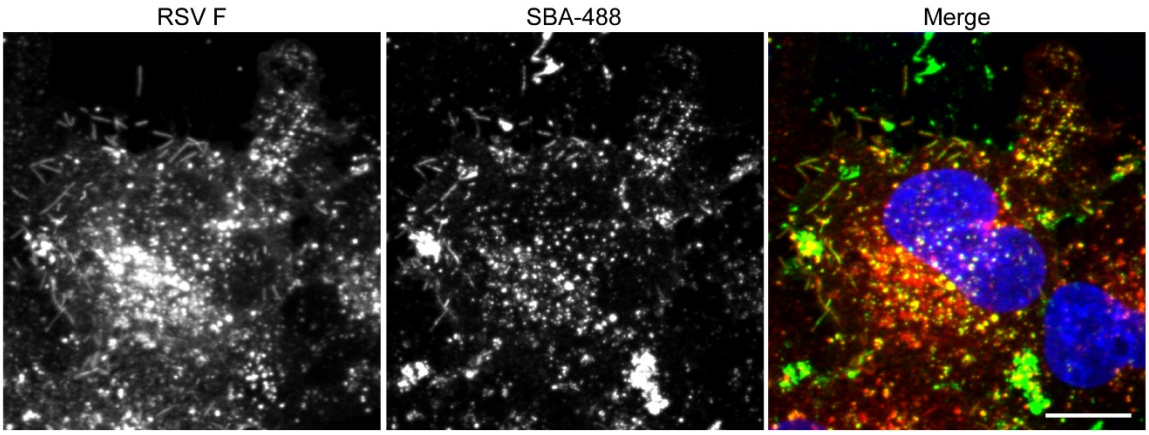

Figure 2.7. Rapidly extending RSV G are RSV filaments. To confirm that the rapidly distending SBA-488 labeled structures were RSV filaments, the set of cells described in Fig. 6 for live-cell imaging was fixed and stained for RSV F (red) and nuclei (blue). Scale bar represents 10 μm.

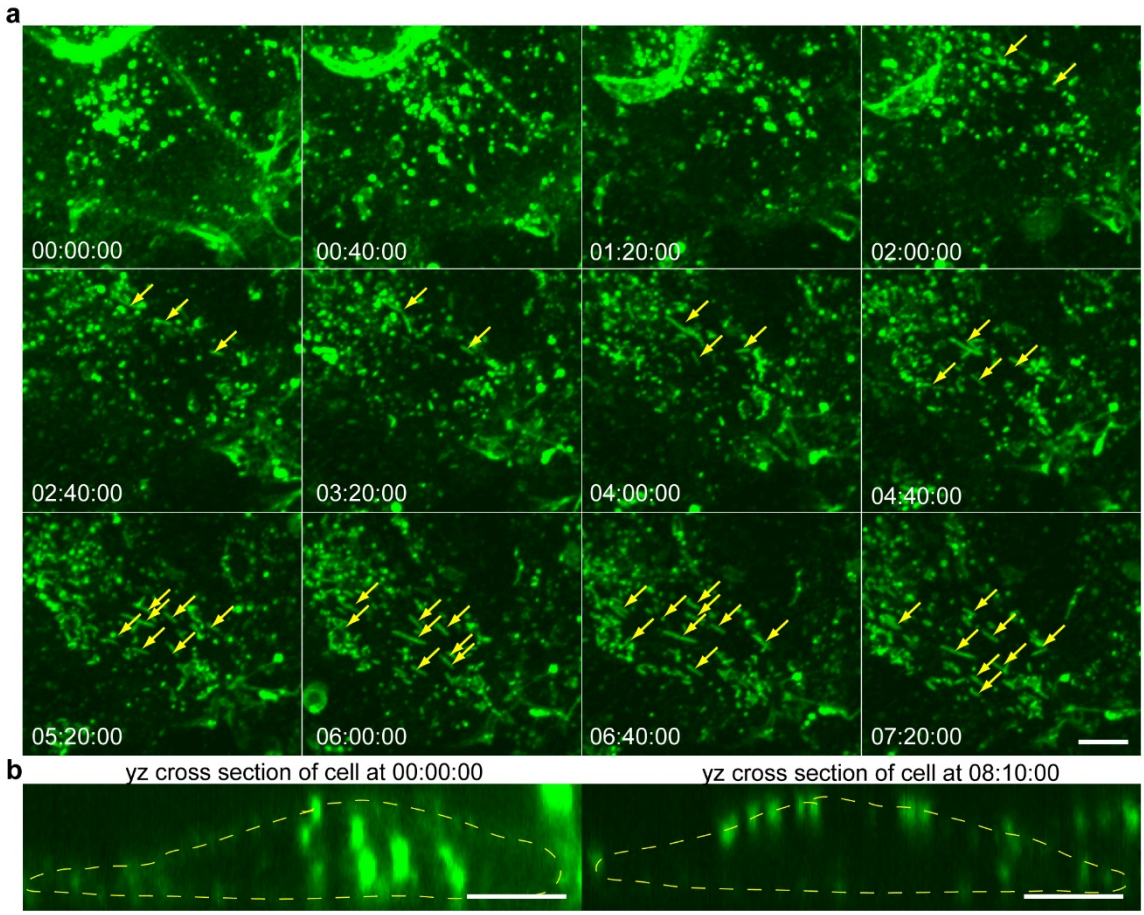

Figure 2.8. RSV filaments are of formed by extension of RSV G vesicles. (A) Vero cells infected for 12 hpi were stained with SBA-488 (green) and imaged live every 10 minutes. Yellow arrows indicate progeny RSV filaments. Scale bar represents 10 μm. Cells are representative of duplicate experiments. **(B)** Cross-sectional views of the same cell 12 hpi and 20 hpi show RSV G granules moving from the intracellular compartment to the plasma membrane during the infection. The plasma membrane is represented by the yellow dashed line. Scale bar represents 10 μm.

Microtubules mediate intracellular filament formation

Because the speed of filament extension and retraction is similar to the previously reported speed of dynein-associated structures, we hypothesized that this motion was governed by molecular motors along microtubules[92]. To investigate this hypothesis, we examined the role of the cytoskeleton and molecular motors in the vesicular extension of RSV filaments. First, we used pharmacological agents to determine which cytoskeletal elements and which molecular motors are involved in the formation of the filaments. The effects of drug treatment were verified with immunofluorescence as previously described[93]. Cells were infected with RSV A2 and stained with SBA-488 12 hpi. After 1 h, cells were imaged live, before and after drug treatment. The motion of single vesicles was analyzed via single particle tracking by computing standard deviation (SD) maps for each image time series over 30 seconds. SD maps are generated by calculating the SD of the intensities on a per pixel basis over a given time frame, resulting in a 2D image of time series data. Fast moving particles result in large intensity fluctuations and correspondingly higher values on the SD map[94,95]. This resulted in fast moving objects appearing as streaks, while slow moving objects will appear as hollow circles, representing diffusive motion over time.

While there was no change in the dynamics of filament extension when cells were exposed to the actin disruption agent cytochalasin D, all vesicular motion was halted when cells were exposed to the microtubule inhibitor nocodazole, to tetracaine, a promiscuous inhibitor of molecular motors, and to erythro-9-(2-hydroxy-3-nonyl)adenine (EHNA), a dynein-specific inhibitor (Figure 2.9A). Unexpectedly, filaments that were present prior to microtubule disruption were static and did not retract. This data suggested that microtubules were involved with the active extension and retraction motion, but not the structural stability of mature RSV filaments. To confirm these results, cells were transduced with GFP-tubulin, infected with RSV and stained with SBA-647 12 hpi.

Extending filaments were found to colocalize or be adjacent to microtubules, further supporting the observation that microtubules are involved with this motion (Figure 2.9B). Together, this data indicated that the microtubule motors are necessary for the formation of RSV filaments.

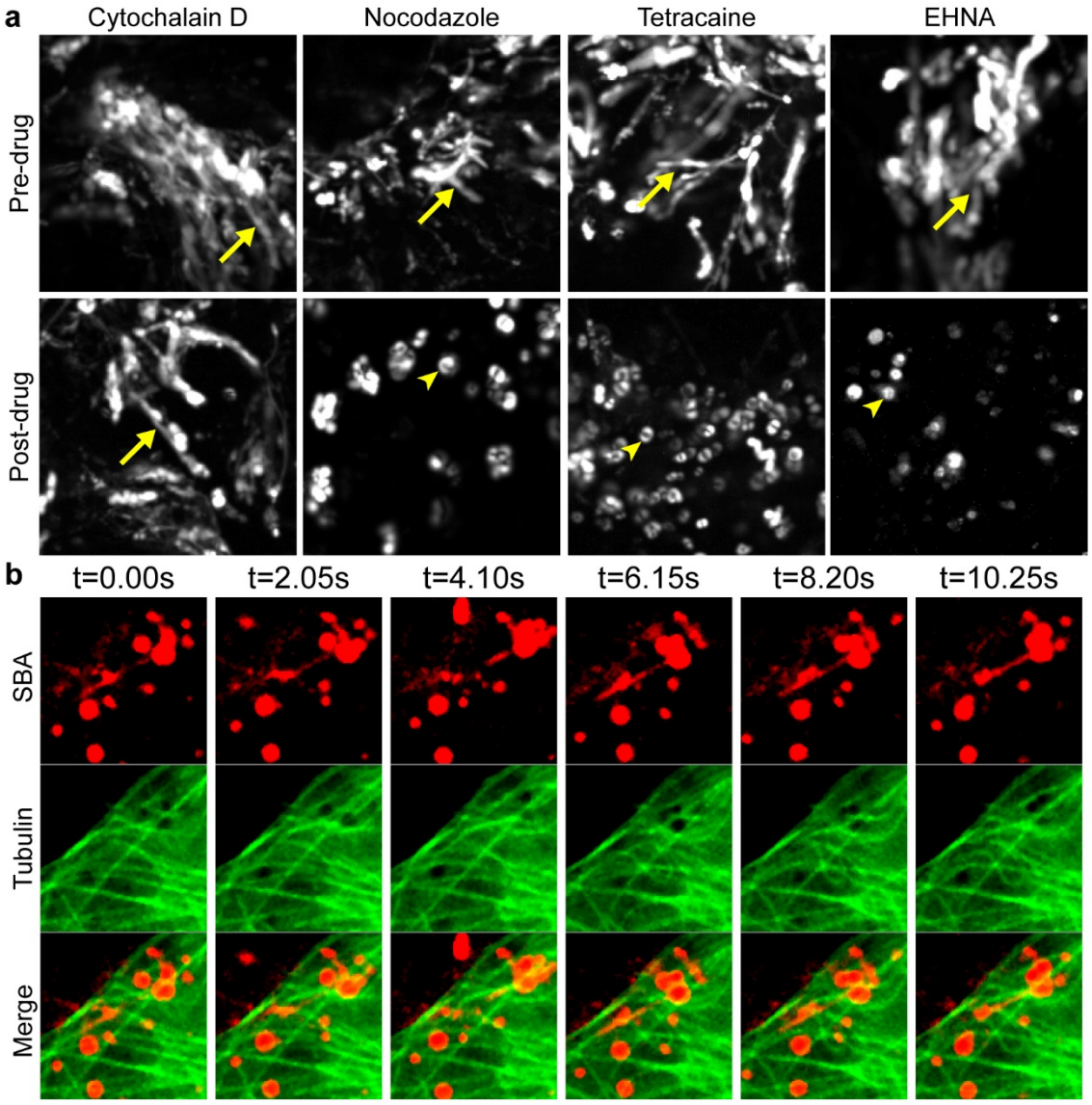

Figure 2.9. Vesicular RSV filament formation is microtubule and dynein dependent. **(A)** Vero cells were infected with RSV A2 at an MOI of 1. At 12 hpi, SBA-488 was delivered to the cells and allowed to internalize for 1 h. Cells were then imaged live briefly at 9 Hz prior to drug delivery to verify the presence vesicular filament formation. Cells were then treated with nocodazole to disrupt microtubules, cytochalasin D to disrupt actin filaments, tetracaine to inhibit molecular motors, or EHNA to inhibit dynein before being imaged live again. Data is presented as SD maps over 30 s of imaging. Yellow arrows indicate fast motion, shown as streaks, while yellow arrowheads indicate slow motion, shown as hollow circles. Scale bars represent 5 μm. **(B)** Tubulin-GFP (green) was expressed in Vero cells overnight prior to infection with RSV A2 at an MOI of 1. At 12 hpi, SBA-647 (red) was delivered and allowed to internalize for 1 h. Cells were then imaged live at 4.9 Hz. Scale bar represents 3 μm.

RNP granules merge with intracellular glycoprotein vesicles

Currently, RSV F and RSV G, among other viral proteins, are thought to accumulate on the plasma membrane prior to genomic RNP trafficking, through an unknown mechanism, to the membrane where mature virions assemble [15,83,96]. Because we observed that the formation of filaments takes place in the cytosol, as indicated by the involvement of microtubules and motors, we sought to investigate the spatial distribution of RSV M, RSV N, and RSV P relative to the connected vesicles and filaments observed in our live cell imaging experiments. Since these structures are lost upon permeabilization with 0.2% Triton X-100, we utilized 0.1% saponin to preserve them, as previously described[21]. RSV infected cells were stained with SBA-488 12 hpi and were allowed to incubate for 2 hours. Vero cells were then fixed in 1% paraformaldehyde, and immunostained for RSV F and either RSV M, RSV N, or RSV P (Figure 2.10A). In each case, RSV M, RSV N, or RSV P were found predominately in intracellular vesicles, while SBA-488 and RSV F were found both in the vesicles and the attached filaments. To confirm that these results were not limited to Vero cells, the experiment was repeated in HEp-2 cells with similar results (Figure 2.10B). These data indicate that RSV M, RSV N, and RSV P are present in vesicles alongside RSV F and RSV G prior to filament formation in the cytosol.

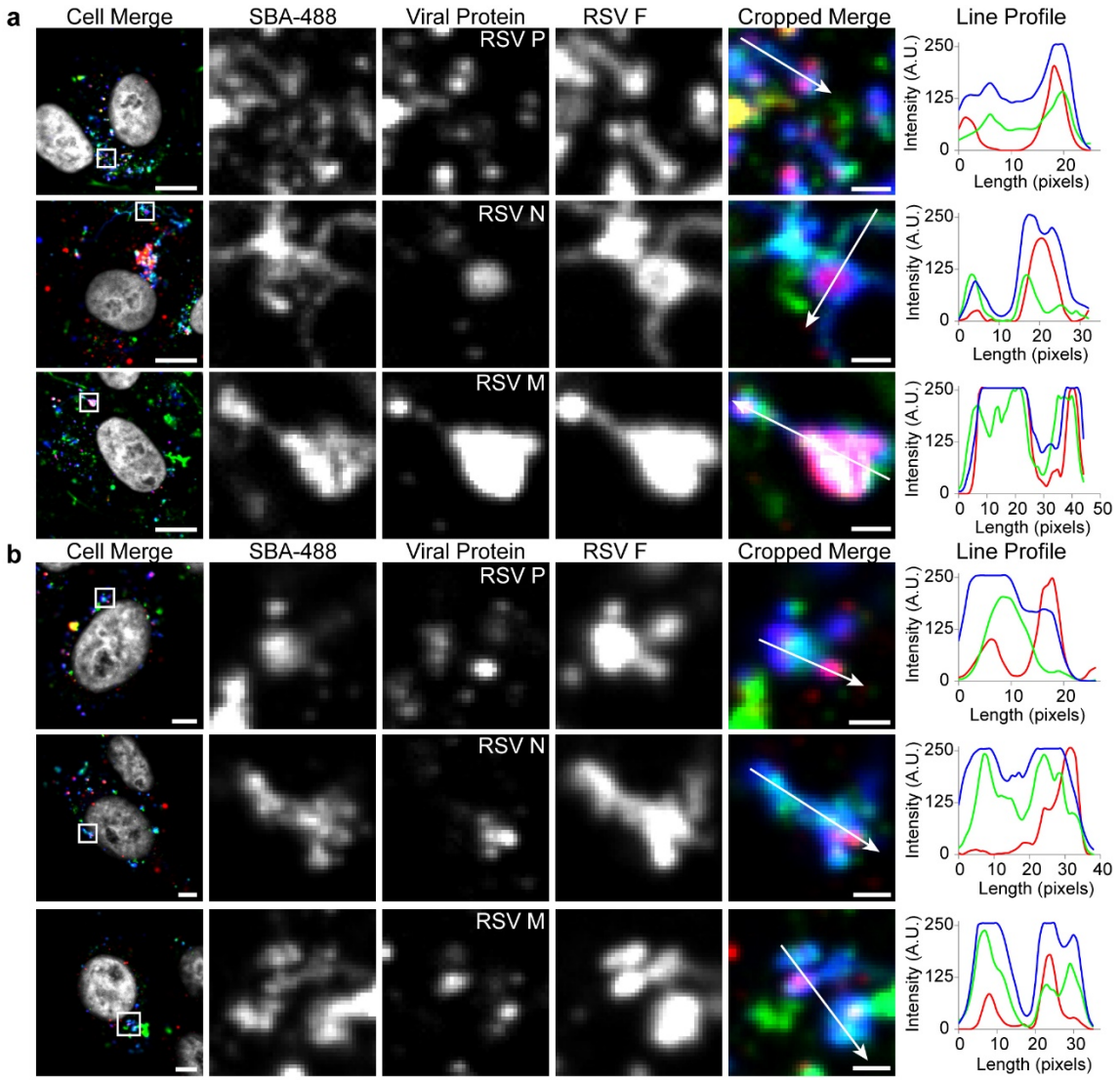

Figure 2.10. RNP granules merge with glycoprotein vesicles prior to the plasma membrane. (A) Vero cells were infected with RSV at an MOI of 1. 12 hpi, SBA-488 (green) was delivered and allowed to internalize for 2 h. Cells were then fixed with 1% PFA, permeabilized with 0.1% saponin, and stained for RSV F (blue) and either RSV P, RSV N, or RSV M, as indicated (red). Scale bar represents 10 μm in whole cell images and 1 μm in cropped images. Enlargement of cropped image from the white boxed region with an intensity profile showing colocalization along the direction of the white arrow. **(B)** The same experiment in **(A)** was repeated in SBA-488 (green) stained HEp-2 cells. Cells were stained for RSV F (blue) and either RSV P, RSV N, or RSV M as indicated (red). Scale bar represents 10 μm in whole cell images and 1 μm in cropped images. Enlargement of cropped image from the white boxed region with an intensity profile showing colocalization along the direction of the white arrow.

Using RSV N as a marker for viral RNPs, we analyzed the colocalization of SBA-488, RSV N, and RSV F in infected cells, where SBA was delivered immediately prior to fixation (Figure 2.11A). Since SBA was delivered before fixation and permeabilization, only RSV G on the plasma membrane was labeled. RSV F and RSV N were found to colocalize as early as 6 hpi and remained closely associated at every time point analyzed (Figure 2.11B). This indicated that viral RNPs and RSV F interact very early during the course of infection within the cytosol, and not only at the membrane as reported previously[24,83]. This observation was confirmed using thresholded Mander's colocalization analysis (Figure 2.11C). The percentage of RSV N containing either RSV F or RSV G remained constant during the course of an infection due primarily to the large quantity of cytoplasmic RSV N. The colocalization between RSV N or RSV F and RSV G on the plasma membrane increased only at 24hpi, indicating that, at this stage, the cytoplasmic granules have merged with the plasma membrane.

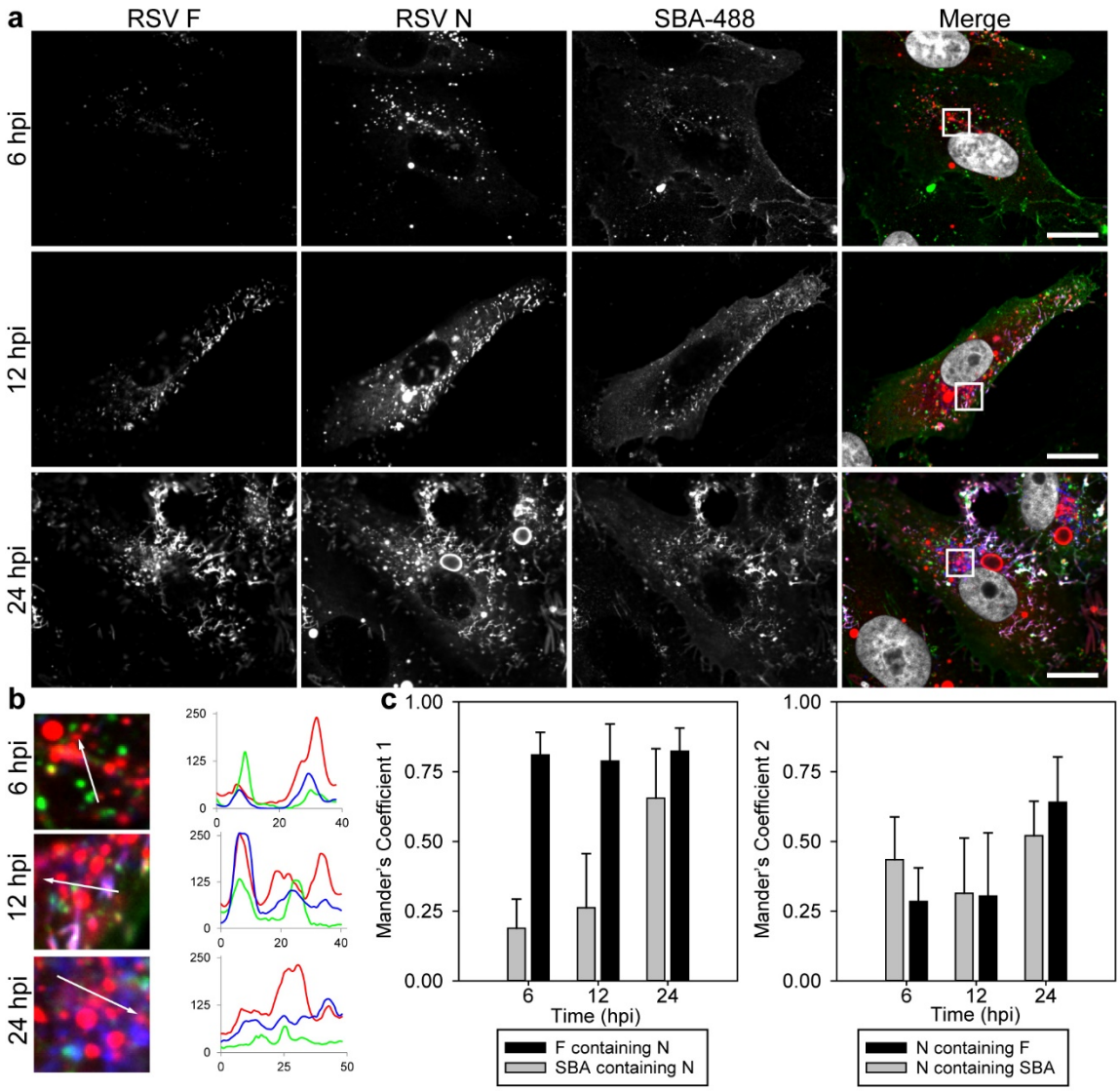

Figure 2.11. RSV RNP granules merge with RSV G granules prior to the plasma membrane. (A) Vero cells were infected with RSV A2 at an MOI of 1. SBA-488 (green) was then delivered to the cells immediately prior to fixation at the indicated time-points post-infection. Cells were then stained for RSV F (blue), RSV N (red), and nuclei (gray). Scale bar represents 15 μm. **(B)** Enlarged cropped images from the white boxed regions from part **(A)** with intensity profiles showing colocalization along the direction of the white arrow. **(C)** Mander's colocalization analysis was performed on 30 individual cells per time-point. Data is represented as the mean Mander's coefficient per cell. Error bars represent standard deviation.

Viral genomic RNA is assembled with extended filaments

Because viral RNP granules appeared to colocalize with the cytoplasmic RSV G granules at early time points prior to viral filament formation, we hypothesized that viral genomes were assembled with progeny viral filaments after filament extension instead of concurrently. To test this, we used fluorescent, multiply labeled tetravalent RNA imaging probes (MTRIPs) to label and visualize the RSV genome[11,97,98]. Cells were infected with RSV A2 for 16 h prior to delivery of MTRIPs via streptolysin O (SLO). After membrane recovery from SLO exposure, SBA-488 was delivered to the cells and allowed to internalize for 1 h before live-cell two-color imaging. Viral genomic RNA initially appeared only in bright SBA-labeled vesicles adjacent to SBA-labeled filaments (Figure 2.12A). Genomic RNAs were then rapidly localized, within 30 s, from the vesicle to the preexisting filament, as indicated by the increase of RNA signal along the filament and the corresponding decrease in the associated vesicle. This data supports our hypothesis that RSV genomes are localized to viral filaments after their extension. We then aimed to determine if microtubules were also involved with genomic RNA localization to RSV filaments. We repeated the above experiment upon treatment with nocodazole to disrupt the microtubule network and observed that the motion of all filaments and viral genomic RNAs was halted (Figure 2.12B). Together, these data suggest that RSV genomic RNAs are localized to extended filamentous virions via a microtubule dependent mechanism.

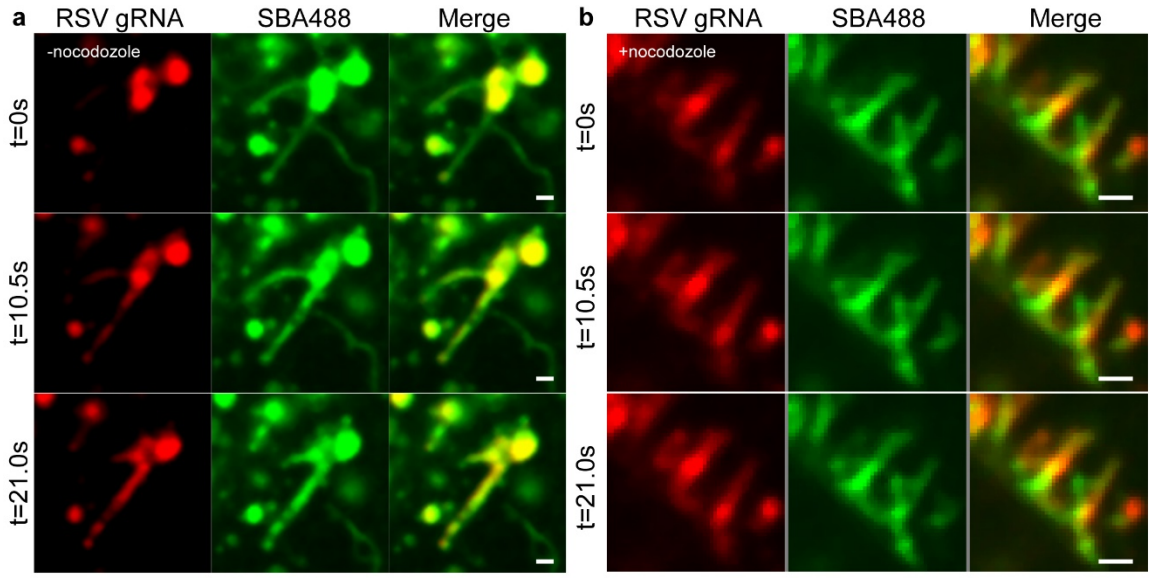

Figure 2.12. RSV genomic RNA is assembled with extended filaments. (A) Vero cells were infected with RSV at an MOI of 1. At 12 hpi, Cy3B-labeled MTRIPs (red) targeted to RSV genomic RNA were delivered at 30 nM. After membrane recovery, SBA-488 (green) was delivered and allowed to internalize for 1 h. Cells were then imaged live at 4.3 Hz. Images were smoothed with a fine rolling ball filter in Volocity. Scale bar represents 1 μm. **(B)** Vero cells were infected with RSV at an MOI of 1. At 12 hpi, Cy3B-labeled MTRIPs (red) targeted to RSV genomic RNA were delivered at 30 nM. After membrane recovery, SBA-488 (green) was delivered and allowed to internalize for 1 h. Microtubules were then disrupted using nocodazole. Cells were then imaged live at 4.2 Hz. Scale bar represents 1 μm.

Conclusion

To our knowledge, this study is the first instance of using fluorescently-conjugated lectins to image RSV glycoprotein dynamics in living cells. We demonstrated that SBA specifically binds RSV G in a manner that does not inhibit the infectivity or replication of the virus, and that SBA permits analysis of RSV G recycling and other dynamics in the context of viral infection.

The apical recycling endosome (ARE) is critical for RSV infections and specifically for the formation of filamentous virions, but the mechanism involved in the recycling of viral proteins is still unclear [8,10]. Previous evidence indicated that RSV glycoproteins internalized in host cells via clathrin-mediated endocytosis and that this event is critical for productive RSV infection. However, these were only investigated in the context of viral entry [81,82]. In this study, we labeled nascent RSV G after translation in the endoplasmic reticulum and transport to the plasma membrane through the Golgi complex. We found that RSV G recycled from the plasma membrane via clathrin-mediated endocytosis and that this mechanism might be associated with the production of RSV filaments, supporting the role of the secretory membrane system in filament formation. Future work will specifically address this issue. Additionally, these findings are substantiated by the recycling of glycoproteins of both Hendra virus and Nipah virus, two other members of the *Paramyxoviridae* family[99,100]. These results also corroborate previous studies on the role of clathrin-mediated endocytosis of both RSV G and the paramyxovirus parainfluenza virus type 5 (PIV-5) hemagglutinin-neuraminidase glycoprotein[101,102]. Additionally, our results indicate that RSV G eventually utilizes caveolin coated vesicles before incorporation into mature virions and filaments, both supporting and elaborating on previous studies on both RSV and PIV-5[83,26,103].

RSV filaments play a key role in the infectivity of the virus. Previous results, obtained analyzing fixed cells, were able to identify viral and host-cell proteins necessary

in RSV filament formation, but they were unable to investigate the dynamics of filament formation and genome localization as they were occurring [10,12,17,18,26–28]. By utilizing SBA-488 to directly label RSV G in living infected cells, we have recorded the first live images of wild-type RSV filament formation. While previous studies have observed filament formation over time, these results were obtained from imaging expressed GFP-fused host-cell factors on the plasma membrane and not by labeling viral proteins[26]. We observed a rapid distension and retraction of vesicular RSV G into viral filaments following its recycling from the membrane. This mechanism is also responsible for the production of branched filaments, which have been observed in previous findings[27]. We measured that the speed of both filament extension and retraction is greater than 2 μm/s, similar to speeds reported for dynein-mediated vesicular transport[92]. These results support earlier reports that microtubules are involved with the assembly of progeny RSV and were confirmed using cytoskeleton disrupting drugs and molecular motor inhibitors[23]. Similarly, the assembly of filamentous Influenza A was found to be mediated by microtubules- and molecular motors-dependent endocytic recycling of vesicles[104–106]. Finally, the role of microtubules in RSV filament assembly indicated that this extension process occurs in the cell cytoplasm *prior* to the plasma membrane, which supports and expands upon previous findings of RSV filaments budding into intracellular vesicles[20,21].

Currently, the dynamics or molecular determinants of RSV genomic RNA localization and loading into progeny virions are unclear[96]. In the present study, we used fluorescence microscopy to analyze the colocalization of RNP and glycoprotein granules over the course of an infection and found that RNPs and glycoprotein vesicles merged as early as 6hpi. Additionally, by using a modified fixation and permeabilization protocol to improve the preservation of the structures seen in our live-cell imaging experiments, we found that these vesicles contained multiple RSV proteins, that are implicated in filament formation, while the filamentous extensions, at early time points, only contained RSV F

and RSV G[17]. Because the ectodomain of RSV G appears to be cleaved in Vero cells during recycling, these results were confirmed in HEp-2 cells[84]. To concurrently track RSV filaments and genome in live infected cells, we utilized SBA-488 to label RSV G and fluorescent MTRIPs to target the RSV genome. We have captured the first recorded images, to our knowledge, of RSV genome loading in filaments, showing that this process occurs after the filament has formed, instead of simultaneously. We also demonstrated that this process is microtubule mediated, indicating that it occurs prior to plasma membrane, supporting and expanding on previous reports[20,21].

Collectively, our results support a new model of RSV assembly and filament production (Figure 2.13). We utilized a fluorophore-conjugated SBA to selectively label nascent RSV G in live infected cells without interfering with RSV replication. Using this method, we determined that membrane bound RSV G recycles from the membrane through clathrin-mediated endocytosis. We also suggest that during the recycling process, RSV G vesicles undergo a transfer to caveolin coated vesicles, which is retained in mature filaments. Additionally, we report that RSV filaments and branched virions are formed prior to the plasma membrane through a microtubule and dynein dependent vesicular extension and retraction motion that occurs during the recycling process. Finally, we demonstrated that RSV glycoprotein and RNP vesicles merge prior to the plasma membrane and that RSV genomic RNA is loaded into extended filamentous virions in a microtubule mediated manner. While we only describe the use of fluorescent SBA specifically label RSV G, fluorescent lectins can be screened against the glycoproteins of other viruses, possibly allowing for the study of live glycoprotein dynamics in a variety of pathogens. Our data supports a new model in the assembly and loading of RSV filaments, inspiring questions regarding RSV assembly and opening the door to the development of novel therapeutics.

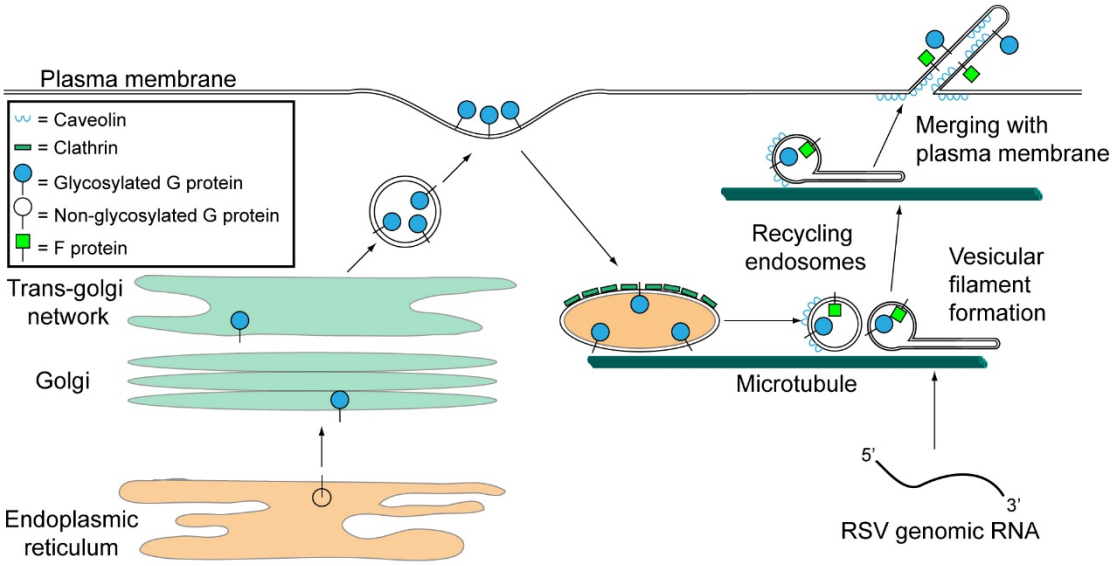

Figure 2.13. Model of RSV filament formation prior to the plasma membrane via the rapid distension of vesicles along microtubules. Progeny RSV G is initially translated into the endoplasmic reticulum before being glycosylated and transported through the golgi network to the plasma membrane. RSV G, labeled with SBA, then is endocytosed and enters the recycling endosome compartment via clathrin-coated vesicles. These vesicles, which also contain RSV F, are distended by dynein along microtubules into filamentous particles prior to being loaded with RSV genomic RNA. During this recycling process, the vesicles colocalize with caveolin. The filaments then mature by merging with the plasma membrane through an unknown process.

Methods

Viruses and Cell Lines

Vero green monkey kidney cells (American Tissue Culture Collection CCL-81) or HEp-2 human epithelial cells (ATCC CCL-23) were cultured in DMEM (Lonza) supplemented with 10% fetal bovine serum (FBS) (Hyclone) and 100 U mL^{-1} penicillin and 100 mg mL^{-1} streptomycin (Life Technologies). Cells were plated on No. 1.5 coverslips (Electron Microscopy Sciences) or 35 mm glass-bottom dishes (In Vitro Scientific) one day prior to infection. Both Vero and HEp-2 cell lines were authenticated by ATCC and were checked for Mycoplasma contamination in our laboratory. HEp-2 cells are commonly used to propagate RSV in culture.

Human RSV A2 (ATCC VR-1544) or rgRSV-GFP (a gift from Martin L. Moore's lab, Emory University) was propagated in HEp-2 cells when the cells were >80% confluent. The media was removed and cells were washed with DPBS (without Ca^{2+} and Mg^{2+}) from Lonza, and virus was added at a multiplicity of infection (MOI) of 0.1 for 1 h before adding complete medium to the inoculum. Cell-associated virus was harvested by scraping the cells when a high degree of cytopathic effects was visualized (about 90% or 96 hpi). Virus was then vortexed briefly, aliquoted, and stored at -80 ºC. Virus titers were measured via plaque assay.

SBA labeling

SBA conjugated to Alexa Fluor 488 and Alexa Fluor 647 was purchased from Life Technologies and reconstituted, stored, and used per the manufacturer's protocol. Briefly, Vero cells were washed with DPBS without Ca^{2+} and Mg^{2+} before being incubated SBA diluted in HBSS (Lonza) to a final concentration of 20 µg/mL for 10 min unless otherwise specified. For RSV G colocalization and endocytic marker colocalization experiments, cells were chilled on ice for 10 minutes and SBA was delivered at 4 ºC to minimize endocytosis and nonspecific binding. Cells were then washed twice with fresh HBSS

before being either fixed, incubated further, or imaged. For live-cell imaging of microtubules alongside SBA, BacMam tubulin-GFP (Life Technologies) was delivered per manufacturer's instructions 16 h before infection with RSV A2 at an MOI of 1.

Synthetic mRNA production and transfections

Plasmids for IVT were designed using the full length nucleotide sequences of RSV F and RSV G from RSV A2 (GenBank M74568.1). The coding region was followed by a 3' untranslated region (UTR) derived from the mouse alpha globin sequence. Sequences were codon optimized and inserted in a pMA-7 vector (Thermo Fisher Scientific, GeneArt) to be used as a template for mRNA synthesis. Plasmids were linearized with Not-I HF (New England Biolabs) overnight prior to IVT using a T7 mScript kit (Cellscript) following the manufacturer's instructions. ATP, GTP, and CTP were used alongside m1Y-5'-triphosphate (TriLink). RNAs were capped using 2'-O-Methytransferase followed by enzymatic addition of a poly-A tail, both according to the mScript kit instructions. The capped and tailed mRNAs were then purified using an RNeasy kit (Qiagen), treated with Antarctic Phosphatase for 2 hours (New England Biolaboratories), and purified again. Vero cells were transfected using a Neon electroporation system (Invitrogen) into a 24 well plate were transfected with 1 µg of synthetic mRNA encoding RSV F or RSV G, respectively, according to the manufacturer's protocol. Twenty hours post-transfection, cells were stained with SBA-488 at 4° C immediately before fixation and immunostaining without permeabilization.

qRT-PCR

Vero cells were plated the day before infection in six-well plates. RSV A2 was incubated with 100 µg/mL of either SBA or vehicle control. Cells were then infected with the different virus treatments at an MOI of 1 for 24 h. Total RNA was extracted using an RNeasy kit (Qiagen) following the manufacturer's protocol. mRNA was then isolated from total RNA using an Oligotex kit (Qiagen) following the manufacturer's protocol. cDNA

synthesis was performed using the same amount of mRNA per condition and an RT^2 First Strand kit (Qiagen) following the manufacturer's protocol. qRT-PCR was then performed in triplicate using the RT^2 SYBR Green ROX qPCR Mastermix (Qiagen) and primer sets (Table 2.1) described in Boukhvalvoa *et. al.,*[107] on a Step-One Plus real-time thermocycler (Applied Biosystems). Rhesus Macaque GAPDH primers (Qiagen) were used as a loading control. Relative quantitation was performed using the Applied Biosystems software. Infections and extractions were repeated twice.

Table 2.1. qRT-PCR primers used in Figure 2.2.

Gene	Forward Primer	Reverse Primer
RSV G	CGGCAAACCACAAAGTCACA	TTCTTGATCTGGCTTGTTGCA
RSV N	AAGGGATTTTTGCAGGATTGTTT	CTCCCCACCGTAACATCACTTG

MTRIP synthesis and delivery

MTRIP design and synthesis is described in detail elsewhere[97]. Briefly, 2'-*O*-methyl RNA/DNA chimeric nucleic acid oligonucleotides targeting the RSV A2 genome contain a 5'-biotin modification (Biosearch Technologies) and 5 internal dT amino groups. These ligands were then labeled with either Cy3B NHS ester (GE Healthcare) or DyLight 650 NHS ester (Pierce) according to manufacturer instructions. Unbound dye was removed via centrifugation in a 3 kDa spin column (Millipore) and stored at -20 ºC until use. Probes were assembled by mixing labeled oligonucleotides with Neutravidin (Pierce) at a 5:1 molar ration and allowed to react for 1 h at room temperature. Unbound oligonucleotides were filtered out by centrifugation through a 30 kDa spin column (Millipore).

MTRIPs were delivered to cells at 30 nM concentration in Opti-MEM I medium (Invitrogen) containing 0.2 U mL^{-1} activated streptolysin O (Sigma) after washing the cells with DPBS without Ca^{2+} and Mg^{2+}. The membrane was then allowed to recover in fresh growth medium for 15 min before imaging.

Antibodies

For western blot, the primary antibody used was a mouse monoclonal anti-RSV G (Abcam, Cat. No. ab94966) diluted to 2 µg/mL in Odyssey blocking buffer (LI-COR) with 0.1% Tween-20. The secondary antibodies were a donkey anti-mouse IRDye 680RD (LI-COR) and a donkey anti-rabbit IRDye 800 (LI-COR) and were diluted 1:3000 in Odyssey blocking buffer with 0.1% Tween-20.

For immunostaining, primary antibodies used were mouse anti-RSV N (Abcam, Cat. No. ab22501), human anti-RSV F (MedImmune, palivizumab), mouse anti-RSV F (Abcam, Cat. No. ab94968), mouse anti-RSV G (a gift from Ralph Tripp, clone 130-6D), rabbit anti-caveolin-1 (Santa Cruz, Cat. No. sc-894), and mouse anti-clathrin light chain (Biolegend, Cat. No. MMS-423P). The mouse anti-RSV F antibody was used only for the mRNA expression experiments in Figure 1. All primary antibodies for immunostaining experiments were used at 1 μg/mL. Secondary antibodies used were donkey anti-rabbit Cy3 (Jackson ImmunoResearch), donkey anti-human Alexa Fluor 647, and donkey anti-mouse Alexa Fluor 488 (Life Technologies). All secondary antibodies for immunostaining experiments were used at 4 μg/mL.

Immunostaining

Vero cells were fixed with 4% paraformaldehyde (PFA) (Electron Microscopy Sciences) for 10 min at room temperature before permeabilization with 0.2% Triton X-100 (Sigma) for 5 min at room temperature. For experiments in Figure 8, cells were fixed in 1% PFA for 10 minutes and permeabilized for 15 minutes in 0.1% saponin. Then, cells were blocked by incubation with 5% bovine serum albumin (Calbiochem) for 30 min at 37ºC before being incubated with primary antibody for 30 min at 37 ºC. Cells were then washed with PBS and incubated with secondary antibody for 30 min at 37 ºC. Multiple antibody labeling was performed simultaneously after checking cross-reactivity. Cell nuclei were then stained with 4',6-diamidino-2-phenylindole (DAPI) (Life Technologies), and coverslips were mounted onto glass slides with Prolong Gold (Life Technologies).

Fixed and live-cell imaging

Images for long-term infection experiments (Fig. 6b) were recorded with a Hamamatsu Flash 4.0 v2 sCMOS camera on a PerkinElmer UltraView VoX spinning disk confocal microscope mounted to a Nikon Ti-e body with a 60x, NA 1.49 CFI apochromat objective. All live-cell experiments were recorded using cells in 35mm glass-bottom dishes

with Leibovitz's CO_2 independent L-15 medium (Life Technologies) supplemented with 10% FBS. Cells and dishes were kept at 37 ºC with a Pathology Device LiveCell stage top incubation system. Images were acquired with the Perfect Focus 3 system engaged to minimize temperature drift.

All other images were acquired with a Hamamatsu Flash 4.0 v2 sCMOS camera on a PerkinElmer UltraView spinning disk confocal microscope mounted to a Zeiss Axiovert 200M body with a 63x NA 1.4 plan-apochromat objective. All images were acquired with Volocity (PerkinElmer) with Z-stacks taken in 0.2 µm increments. Cells and dishes were kept at 37 ºC during imaging by using a Chamlide TC-L live-cell stage-top environment with objective heater (Live Cell Instrument).

Drugs

After MTRIP delivery and SBA-labeling, Vero cells were incubated for 90 min with 1 µM cytochalasin D (Sigma) for actin depolymerization, for 90 min with 4 µM nocodazole (Sigma) for microtubule depolymerization, or for 15 min with 1mM EHNA (Sigma) for dynein inhibition. After incubation, live-cell imaging was performed in Leibovitz's L-15 media. Tetracaine was used to promiscuously inhibit motors at 100 µM in L-15 and cells were imaged immediately. To inhibit clathrin-mediated endocytosis chlorpromazine (Sigma) was used at 10µg/mL and was delivered 2 hours prior to SBA delivery, and cells were incubated an additional hour in media containing the drug prior to fixation.

Image processing

All colocalization and object volume analysis was performed in Volocity. Movies were exported from Volocity as TIFF files and imported into ImageJ (NIH) for STD map generation using the ZProject plugin. To obtain intensity profiles, images were exported as TIFF files into ImageJ for analysis using the RGB profiler plugin, and results were plotted in Excel (Microsoft). Linear contrast enhancements were applied to images and

videos for clarity. All image quantification and analysis was completed on unenhanced data.

Western blotting

Vero cells were plated the day before infection in six-well plates. RSV A2 was incubated with 100 µg/mL of either SBA or vehicle control. Cells were then infected with the different virus treatments at an MOI of 1 for 24 h. Cells were lysed with RIPA buffer (Pierce) containing 1x Complete Protease Inhibitor (Rosche) before being scraped and clarified by centrifugation. Protein concentration was calculated using a BCA assay (Pierce) following the manufacturer's protocol. Lysates were stored at -80 ºC until further use.

For gel electrophoresis, 12 µg of lysates were mixed with 4x SDS loading buffer (LI-COR Biosciences), boiled for 10 min at 70 ºC, chilled on ice, and loaded into wells of a Novex 10% Bis-Tris precast gel (Life Technologies) alongside a molecular weight marker (LI-COR). Gel was run in an XCell Surlock Mini Cell system (Life Technologies) in 1X MOPS running buffer (Life Technologies) at a constant 200V for 50 min. Protein was then transferred to 0.45 µm pore nitrocellulose membranes (Life Technologies) in 1x Western transfer buffer (Life Technologies) at a constant 30 V for 1 h using an XCell II Blot module (Life Technologies).

Western blots were stained using a Snap i.d. blot holder (Millipore). Nonspecific binding was blocked using Odyssey blocking solution at room temperature (LI-COR). Vacuum was then immediately applied for 20 s to remove solution. Primary antibody, including a rabbit anti-ß-actin antibody (Cell Signaling Technology, Cat. No. 8457) loading control (diluted 1:1000), was then applied and allowed to incubate for 10 min. Vacuum was then applied and the blots were washed three times with 1x PBS containing 0.1% Tween-20 (PBST). Secondary antibody was then applied and allowed to incubate for 10 min before blots were again washed three times with PBST. Blots were imaged using an

Odyssey IR scanner (LI-COR). Only linear contrast enhancements were performed for the final representative images.

Virus neutralization assay

rgRSV-GFP stocks were mixed with the indicated concentrations of SBA, palivizumab, or vehicle control and allowed to bind for 2 h on a tube rotator at 37 ºC. Vero cells were then infected at an MOI of 1 with the virus treatments or control containing only complete growth medium. 3 hpi, cells were washed with with a 40 mM sodium citrate solution containing 10 mM potassium chloride and 135 mM sodium chloride (Sigma) adjusted to pH 3.0 to eliminate any virus that had not yet internalized before being returned to complete growth medium. 48 hpi, cells were lifted into single-cell suspensions with 0.25% Trypsin (VWR) before being suspended in FACS buffer (DPBS without Ca^{2+} and Mg^{2+}, supplemented with 1% FBS and 5mM EDTA). Cells were then analyzed for GFP fluorescence with an Accuri C6 flow cytometer (BD Biosciences).

Viral filament isolation

SBA-488 (20µg/mL) was mixed with RSV-A2 stocks for 30 minutes at 37 ºC before filtration and isolation of viral filament as described previously[11]. Briefly, SBA-labeled virus was first centrifuged through 5 and 0.45 µm filters (Millipore) at 5,000 g and 4 ºC for 4 and 1 min, respectively, to remove the dead cell debris from the cell-associated RSV stock. For imaging RSV virion on glass, coverslips were coated with poly-L-lysine (Sigma) in a 24-well plate. Labeled and filtered virion were then centrifuged onto the surface of the coverslips for 30 min at 4ºC and 2,400 g. For infecting cells with SBA-labeled virus, titer was adjusted accordingly to an MOI of 1 before inoculating Vero cells.

Statistical analysis

Results were plotted and statistical analyses were performed using Prism 7 (GraphPad). Power analysis was performed to ensure adequate sample size for experiments. For two-group comparisons, the Mann-Whitney U test was performed. For

comparisons of greater than two groups, one-way ANOVA on ranks or two-way ANOVA was performed as appropriate.

CHAPTER 3

PREVENT RSV INFECTION IN MICE USING INTRATRACHEAL AEROSOL DELIVERY OF RNA-ENCODED MEMBRANE-ANCHORED NEUTRALIZING ANTIBODIES

The work presented here is from Tiwari PM*, Vanover D*, Lindsay KE, Bawage SS, Kirschman JL, Bhosle S, Lifland AW, Zurla C, Santangelo PJ. **"**Engineered mRNA-expressed antibodies prevent respiratory syncytial virus infection." *These authors contributed equally to this work. *Nature Communications* **(In Revision)**.

Background

Acute respiratory infections are responsible for the hospitalization and deaths of millions of individuals annually worldwide[1]. Current vaccine strategies are limited to inactivated, recombinant, and live-attenuated types, though nucleic acid vaccination is actively being investigated in preclinical and clinical trials[108–114]. These approaches, though very powerful, take time to take effect, limiting their utility during pandemics. Additionally, prophylaxis remains limited to antivirals and, in the case of respiratory syncytial virus (RSV), the broadly neutralizing antibody palivizumab is the only FDA approved treatment for high-risk populations. The limited application of palivizumab is likely due to its debated efficacy. Palivizumab, delivered by intramuscular (IM) injection, is present in the serum at titers 2,000 fold higher than in bronchoaveolar lavage (BAL) samples[5]. This indicates that the majority of palivizumab injected IM is not delivered to the appropriate organ compartment to neutralize the virus, which potentially explains the limited reduction in hospitalization rates observed in treated infants[3]. Therefore, there is a need for a rapidly-expressed, targeted prophylaxis technique to prevent pulmonary infections.

To date, no DNA-based therapeutics have been approved for human use due primarily to safety concerns. First, DNA-based therapeutics incite concerns of integration

into the host genome, and while this effect has been found to be minimal to date, integration must continue being monitored for each antigen expressed by the DNA[39,40]. Modified adeno-associated viruses (AAV) are a prominent vehicle for nucleic acid therapeutic delivery, in part due to being replication deficient and minimally pathogenic[52–54]. However, because AAV-based therapies are permanent and elicit an immune response, repeated dosing is not currently possible[56–58]. Moreover, this immune response would preclude the ability to deliver additional AAV-based therapeutics targeting different pathogens or additional strains.

Delivery of therapeutic-encoding mRNA, directly to the lung, aims to safely and transiently increase therapeutic protein concentration in the target organ, compared to systemic purified recombinant protein delivery, frequently administered IM[70,115,116]. Additionally, more protein is produced during peak expression following delivery of naked mRNA compared to naked plasmid DNA[51]. Still under investigation, aerosol delivery of mRNA has been shown to elicit transient protein expression that is capable of treating disease[70–72]. Targeted delivery of therapeutics to the organ of interest has the potential to minimize systemic toxicity, anti-antibody immune responses, and reduce the amount of drug required to achieve therapeutic levels.

Here, we developed a modular toolbox to express synthetic, modified mRNA and prevent viral infections in the lung. First, we expressed whole palivizumab (secreted, termed sPali) in the lung via synthetic mRNA delivery by intratracheal aerosol. Second, we linked the well characterized glycosylphosphatidylinositol (GPI) membrane anchor sequence from the decay accelerating factor (DAF) to the palivizumab heavy chain mRNA (Figure 3.1A-B)[117,118]. Anchored palivizumab was termed aPali; we expected that cells transfected with aPali would retain the immunoglobulin on the epithelial surface, increasing its concentration in the lung and improving efficacy. Finally, we demonstrated that the GPI anchor is adaptable to other constructs by linking it to a RSV-neutralizing

VHH camelid antibody (aVHH), previously demonstrated to be more potent than palivuzmab[119]. The anchored VHH also inhibited RSV infection *in vitro* and *in vivo*.

In this study, we found that mRNA-expressed anchored neutralizing antibodies, both whole and single domain: (1) are rapidly expressed and retained on the surface of transfected cells in culture and in mouse lungs, (2) prevented RSV infection *in vitro* and *in vivo*, and (3) were minimally immunogenic. Together, these technologies comprise a modular mRNA toolbox to express a variety of engineered neutralizing antibodies to prevent pulmonary infections.

aPali is anchored to the plasma membrane and prevents RSV infection in transfected cells

We first verified the assembly of whole antibodies expressed from synthetic mRNA by staining with an anti-human IgG antibody *in vitro*. The anti-human IgG antibody efficiently stained cells co-transfected with mRNAs encoding for the light and heavy chains at a 1 to 4 molar ratio. No staining was observed in cells transfected with only light chain mRNA, while cells transfected with only the heavy chain mRNA showed significantly lower staining. Therefore, we concluded that the mRNAs for both heavy and light chains were efficiently translated to form whole IgG antibody (aPali) (Figure 3.1C).

Next, to establish that the GPI membrane anchor encoded in the heavy chain sequence was functional, we transfected cells with mRNA encoding for either aPali or sPali, and compared the localization of assembled antibodies at 2, 4, 6, 12, and 24 hours post transfection, with and without Triton-X permeabilization (Figure 3.1D). Without permeabilization, strong surface staining was visible as early as 2 hours in cells transfected with aPali mRNA, indicating rapid antibody production and localization to the plasma membrane. The surface staining was strongest between 6 and 12 hours after transfection and remained so at 24 hours after mRNA delivery. In contrast, in cells

expressing sPali mRNA, membrane staining was minimal, indicating that the expressed antibodies were not localized to or concentrated on the plasma membrane.

When the localization was evaluated with permeabilization, sPali was found in the secretory membrane system from 2 to 12 hours after transfection, with a dip in intensity at 24 hours, possibly due to both the decreased mRNA expression and diffusion of sPali into the growth media. Interestingly, aPali can be observed in the secretory membrane pathway from 2 to 6 hours after transfection, but at lower concentrations, indicating a reduced accumulation in this cell compartment as well as on the plasma membrane as early as 2 hours post-delivery. Together, these data show that the GPI encoded membrane anchor is functional, and anchoring the antibody on the membrane prevents aPali diffusion into the growth media.

To demonstrate that aPali can bind and inhibit RSV infection, we transfected cells with mRNA encoding either the heavy chain, the light chain, or both the heavy and light chains. The cells were infected with RSV 24 hours after mRNA delivery; infected cells, not exposed to the mRNA, were used as a positive control. Cells were then fixed, permeabilized, and stained for aPali, RSV nucleoprotein (RSV N), and with a panRSV polyclonal antibody (Figure 3.1E). No infection was detected in cells transfected with both the heavy and light chain of aPali. This demonstrates that transfection with both chains is required for successful binding and neutralization of RSV. This was quantified by measuring the volume of RSV N signal upon infection (Figure 3.1F). In untransfected cells, RSV replicated, with the RSV N signal representing approximately 21% of the total volume per cell. In aPali transfected cells, we detected a 99% reduction in the volume of RSV N, with the residual signal likely derived from the viral particles in the inoculum. In addition, aPali mRNA transfection resulted in a 2 log reduction of infectious RSV titer via plaque assay (Figure 3.1G, Figure 3.2). Overall, these data demonstrate that aPali mRNA transfection prevents RSV infection *in vitro*.

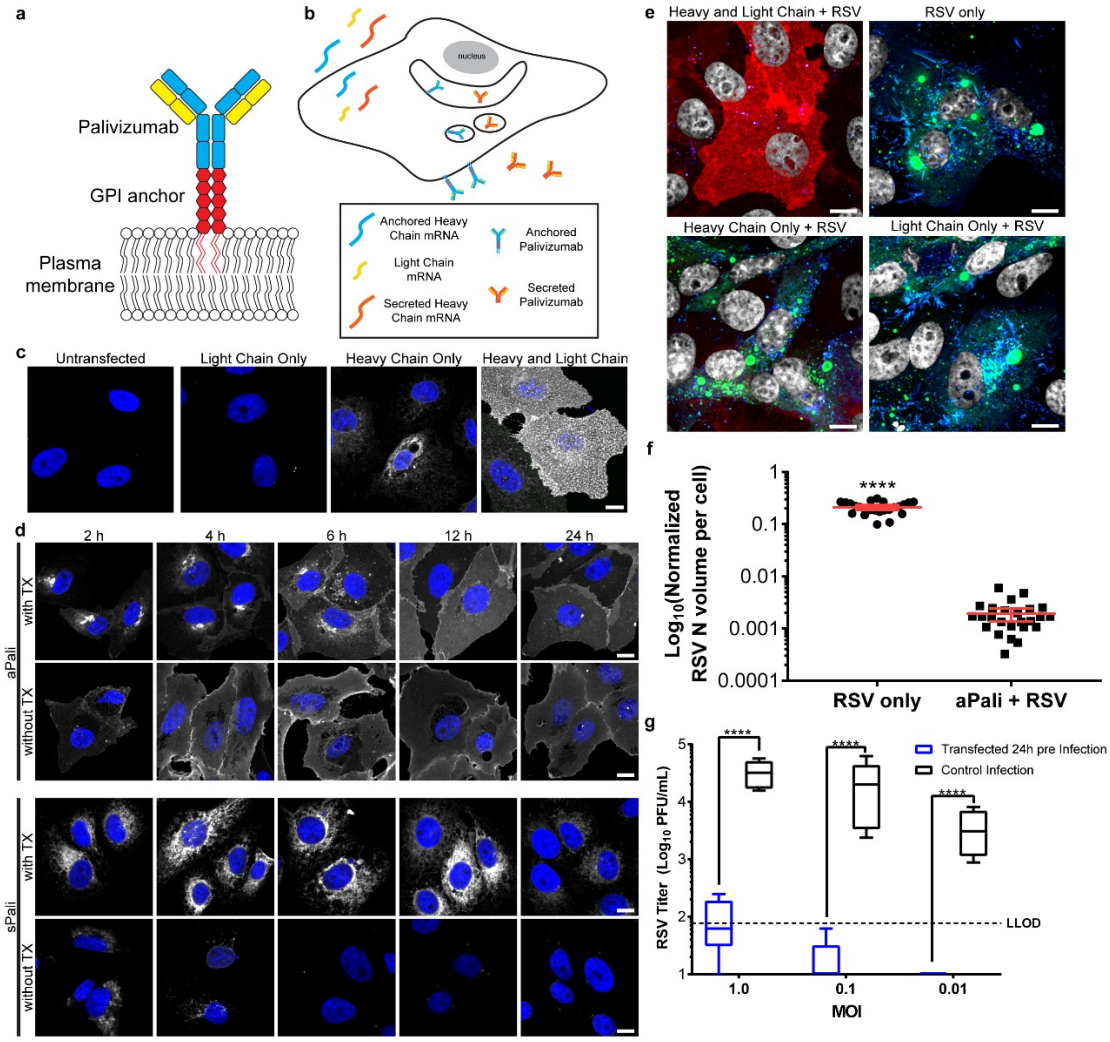

Figure 3.1. aPali is anchored to the plasma membrane and prevents RSV infection in transfected cells. (A) Schematic of aPali anchored to the plasma membrane. **(B)** Schematic of aPali and sPali mRNA delivery and expression. **(C)** Cells were transfected with vehicle control or 1 µg of either aPali heavy chain only, aPali light chain, or both the heavy and light chain mRNAs. 24 h later, cells were fixed, permeabilized, and stained with a donkey anti-human secondary antibody (white). Scale bar represents 10 µm. **(D)** Cells were transfected with 1 µg of either aPali or sPali mRNA. At 2, 4, 6, 12, and 24 hours, cells were fixed, permeabilized or not, and stained for the expressed antibody (white). Scale bar represents 10 µm. **(E)** Cells were transfected with vehicle control or 1 µg of either aPali heavy chain only, aPali light chain only, or both the heavy and light chain mRNAs. After overnight incubation, cells were infected for 24 h before being fixed and stained for RSV N (green), panRSV (blue), and aPali (red). Scale bar represents 10 µm. **(F)** Quantification of the mean volume of the RSV N signal per cell from microscopy images in part **(E)**. Error bars represent 95% confidence intervals. Asterisks indicate $p<0.0001$ (Mann-Whitney U test). **(G)** Cells were transfected with vehicle control or 1 µg of aPali and infected with RSV at MOI of 0.01, 0.1, and 1. Supernatants were collected at 24 hpi and virion titers were measured by plaque assay. Boxes represent 25th and 75th percentile along with the mean, while whiskers represent the minimum and maximum values. Dotted line represents lower limit of detection. Asterisks indicate $p<0.0001$ (one-way ANOVA of log-transformed data).

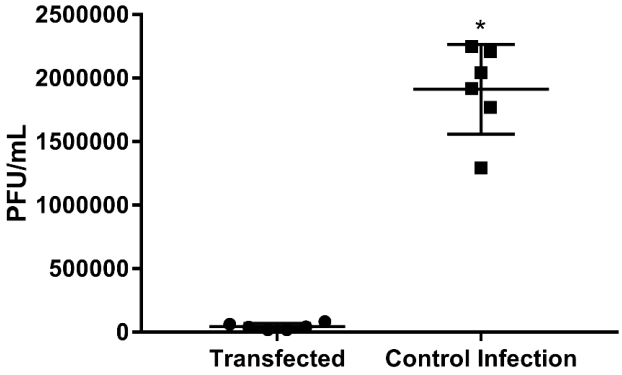

Figure 3.2 – aPali reduces RSV titer on transfected cells. Cells were transfected with 1 µg of aPali or left untransfected. After 24 h, cells were infected with 50 PFU of RSV A2. Virion titer was determined by plaque assay directly on the transfected or control cells. Error bars indicate standard deviation. Asterisk indicates $p<0.05$ (Wilcoxon test).

Mechanism of action of aPali prophylaxis evaluated by super-resolution microscopy

Next, we sought to delineate the mechanism by which aPali prevented infection of transfected cells. Conventional spinning disk confocal microscopy does not afford the necessary axial resolution to determine if RSV particles are internalized in aPali transfected cells or merely attached to the plasma membrane (Figure 3.3A). To overcome the resolution constraint, we employed a 3D direct stochastic optical reconstruction microscopy (dSTORM) system with ~20 nm lateral and ~50 nm axial resolution. We transfected cells with aPali mRNA overnight before infecting them with RSV. At 2 and 20 hpi, cells were fixed and immunostained for aPali and RSV N, with and without permeabilization. In untransfected cells infected with RSV, large inclusion bodies and long filaments were visible (Figure 3.4). In transfected cells, using dSTORM, we observed aPali at the plasma membrane along the contour of the cell (Figure 3.3B). Additionally, at 2 and 20 hpi, individual RSV virions were observed at the aPali-labeled membrane. Specifically, at both time points, single virions of ~100-300nm, the expected size of spherical-like RSV particles, were localized 180 nm (at 2 hpi) and 113 nm (at 20 hpi) above the plasma

membrane (Figure 3.3C). These results revealed that RSV particles were not internalized over time, demonstrating that the mechanism by which aPali inhibits infection is by preventing fusion and cytosolic uptake of RSV.

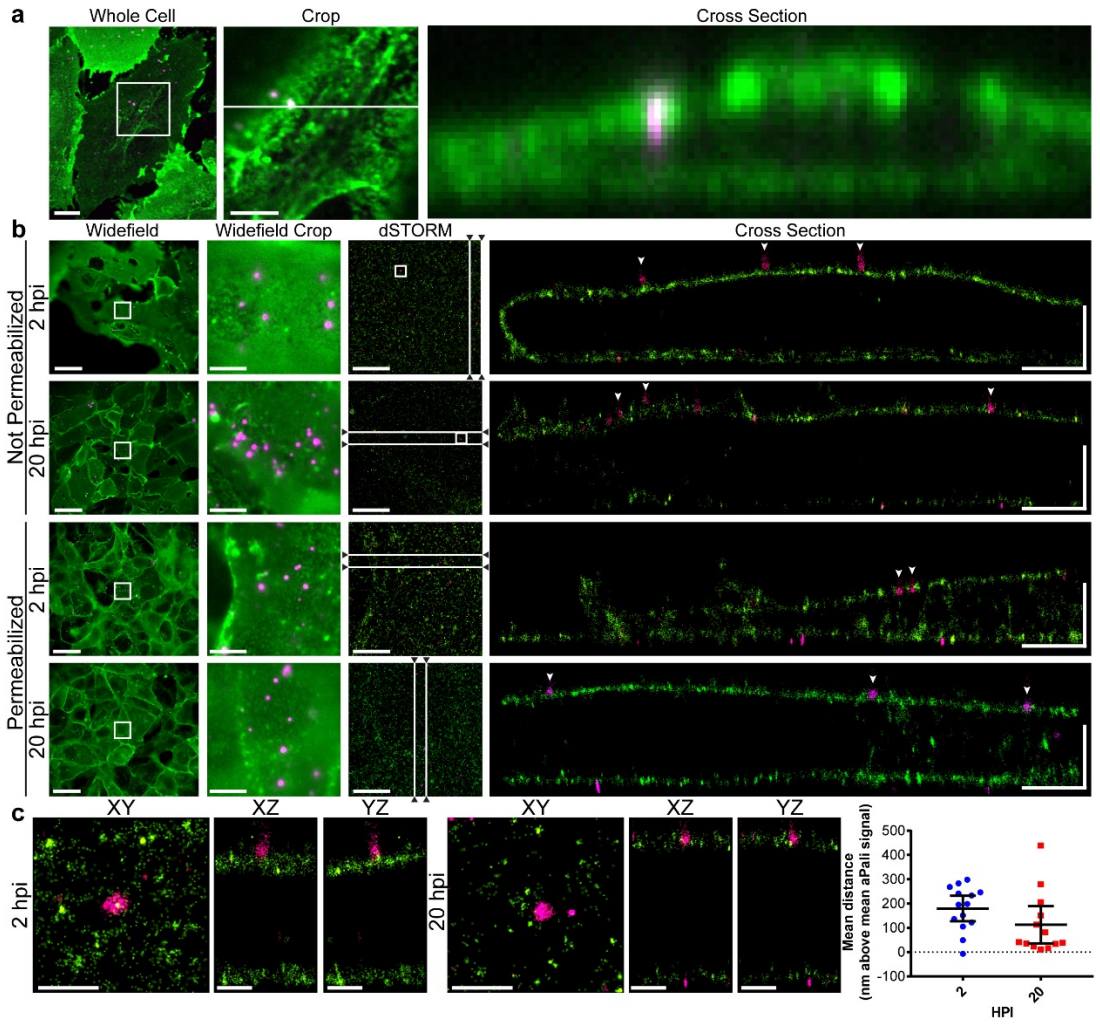

Figure 3.3. Mechanism of action of aPali prophylaxis evaluated by super-resolution microscopy. (A) Vero cells were transfected with 1 µg of aPali and infected with RSV at MOI of 1. At 24 hpi, cells were fixed, stained with anti-human secondary (green) and for RSV N (magenta) and imaged using a confocal microscope. Cropped image is a magnification of white box inset. Cross section is along the white line in the cropped image. Scale bar in whole cell represents 10 µm, while scale bar in cropped image represents 5 µm. **(B)** The same cells from part **(A)** were imaged using 3D dSTORM. Cells were fixed at either 2 or 20 hpi and permeabilized or not, as indicated. Widefield reference images were captured on the same microscope immediately prior to acquisition, with the cropped region indicating magnification of the white box. dSTORM images were acquired on the widefield cropped region. Cross section views are shown from a 2 µm slice through the XY image as indicated by the white lines. Arrowheads indicate single RSV virions. Scale bar in the widefield images represent 20 µm, while scale bars in the widefield crop and dSTORM images represent 5 µm. Scale bar "L" represents 2 µm in both directions. **(C)** Single RSV particles were cropped from white boxes in the dSTORM images from unpermeabilized cells in part **(B)**. XY views as well as XZ and YZ are shown. Scale bars represent 700 nm. Individual viral particles were isolated in software and the mean distance in the z direction between the aPali and RSV N signals per particle was determined at 2 and 20 hpi. Error bars represent 95% percent confidence interval. No significant difference was found, $p>0.05$ (Mann-Whitney U Test).

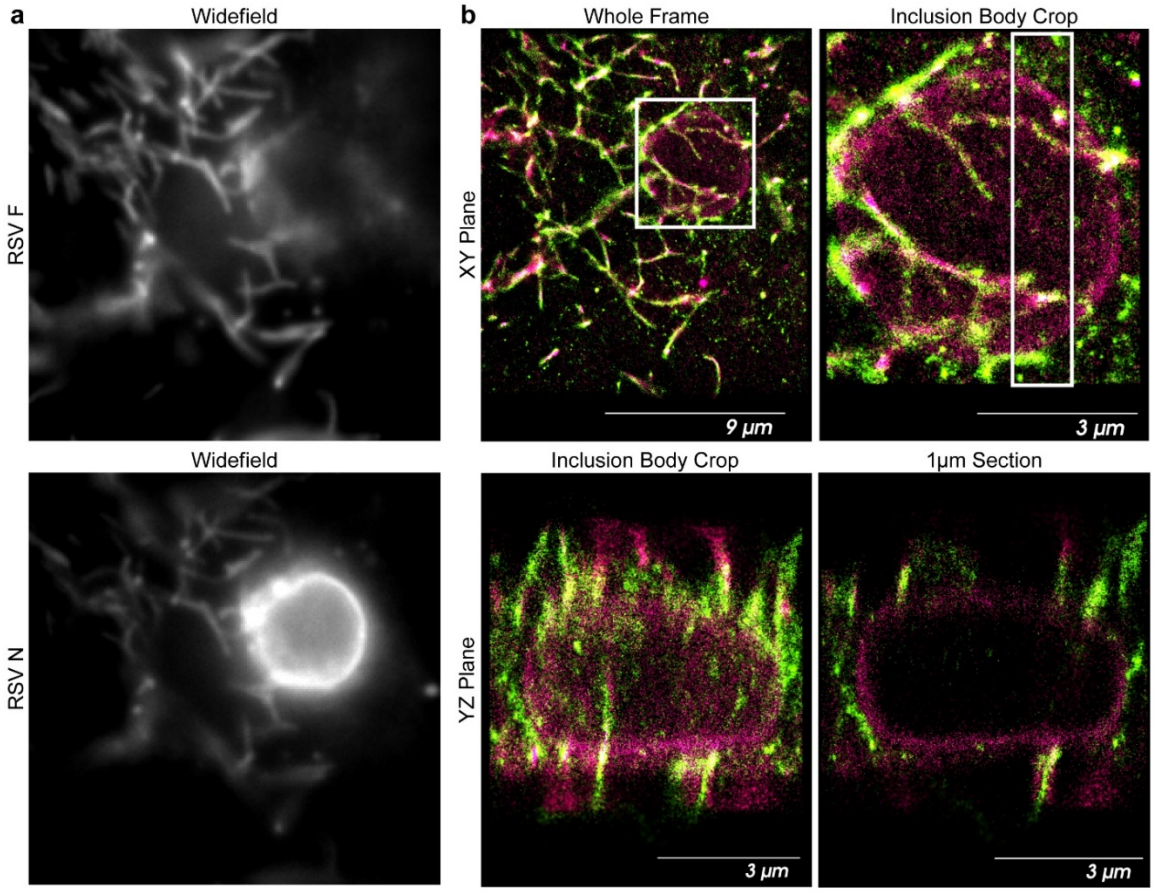

Figure 3.4. dSTORM imaging of untransfected cells infected with RSV. (A) Untransfected Vero cells were infected with RSV at MOI of 1. At 24 hpi, cells were fixed, stained with for RSV F (top) and RSV N (bottom) and imaged using the widefield function on the Vutara. **(B)** The same region from partA was analyzed using dSTORM, with RSV F pseudocolored green and RSV N pseudocolored magenta. Cropped inclusion body is indicated by the white box in the whole frame view. The section of the inclusion body is indicated by the white rectangle in the cropped image. XY (top) and YZ (bottom) cross-sections are shown.

Lung distribution of aPali mRNAs and mRNA expression in the lung epithelium

Before performing *in vivo* challenge studies, we first aimed to determine the distribution of aPali mRNA in the lung. To accomplish this, we used fluorescent multiply labeled RNA imaging probes (MTRIPs) bound to the mRNA prior to delivery[93,97]. Recently, we demonstrated that this method allowed for the tracking of exogenous mRNA using a variety of detection techniques while not significantly impacting translation[120]. We labeled aPali heavy chain mRNA with Dylight-650 MTRIPs and aPali light chain mRNA with Cy3B MTRIPs and delivered the labeled mRNA into the lungs of BALB/c mice by intratracheal aerosol. Animals were sacrificed after 4 hours and heavy and light chain mRNA distributions in the lung were analyzed by confocal microscopy. In the transfected lungs, mRNA was distributed throughout the tissue (Figure 3.5A). High magnification images confirmed that both the heavy and light chain mRNAs colocalized in discrete granules inside transfected cells (Figure 3.6A). We then analyzed the colocalization of the exogenous mRNA with either Rab5, an early endosome marker, or Rab7, a late endosome marker. We found that 24.4% of the delivered mRNA colocalized with late endosomes and 39.7% with early endosomes, indicating that some of the mRNA was still trafficking through the endosomal system of alveolar cells at 4 hours post transfection (Figure 3.6B, Figure 3.5B). Notably, since only half of the mRNA was associated with endosomal markers, a significant fraction of it was likely free in the cytosol (Fig. 3.6C).

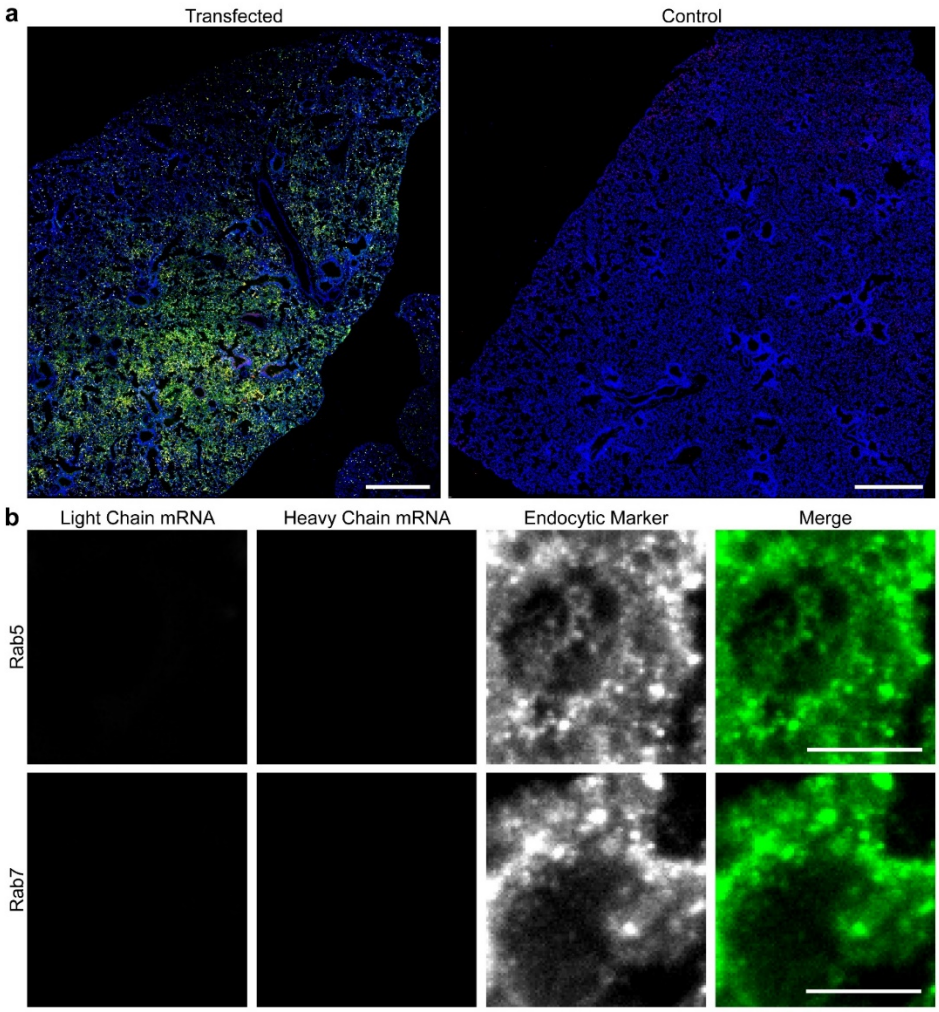

Figure 3.5. Labeled aPali biodistribution in lung lobe. (A) Cy3B labeled light chain (red) and DyLight 650 labeled heavy chain (green) mRNA was transfected into the lungs of mice (left). Saline was injected as a negative control (right). At 4 hours, lungs were excised and cryosectioned before being imaged. Scale bar represents 750 μm. **(B)** Control tissue sections from part **(A)** were stained for Rab5 or Rab7 (green) for early or late endosomes, respectively. Scale bar represents 5 μm.

Next, we assessed whether aPali mRNA was expressed and retained on the surface of transfected cells *in vivo*. We delivered aPali or sPali encoding mRNA using Viromer RED (VR), a modified form of PEI, to the lungs of BALB/c mice using intratracheal aerosol. After 4 hours lung tissue sections were stained for the expressed antibody and imaged (Figure 3.6D). Lungs transfected with aPali displayed a strong antibody signal on the apical surface of the airway epithelial cells. On the contrary, lungs transfected with sPali showed pockets of expressed antibody predominately within alveolar epithelial cells. Then, we evaluated the distribution of DyLight-680 labeled mAb palivizumab injected via IM, and studied the distribution of the antibody *in vivo* using a handheld near-infrared imager as well as with microscopy. We found that the DyLight 680-labeled antibody was present in the lung, as well as throughout the body, with the most intense fluorescent signal in the injected tibialis muscle (Figure 3.7). Next, we sought to quantify the percentage of lung cells expressing aPali upon intratracheal aerosol. We transfected mice with mRNA encoding the aPali heavy chain and a light chain sequence modified with a C terminus V5 peptide tag, included to improve detection via flow cytometry. After 24 hours, mice were sacrificed and the lungs were analyzed for V5 expression by flow cytometry. We found that in two of the transfected mice, more than 70% of the isolated lung cells were expressing aPali-V5 (Figure 3.6E). This indicated that aPali can be expressed in mice lungs and is anchored to the surface of transfected cells in the lungs.

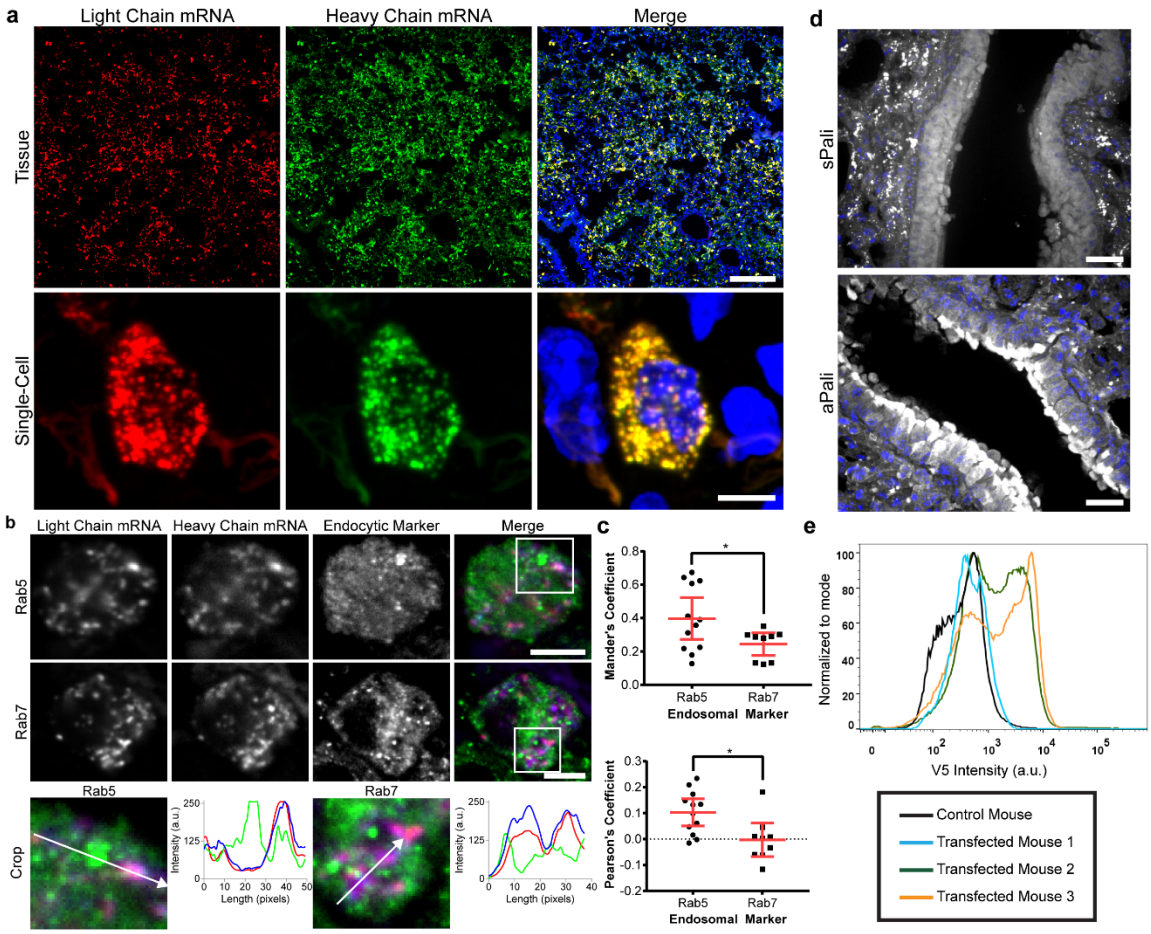

Figure 3.6. Lung distribution of aPali mRNAs and mRNA expression in the lung epithelium. (A) Cy3B labeled light chain (red) and Dylight 650 labeled heavy chain (green) mRNA was transfected into the lungs of mice. At 4 hours, lungs were sectioned and imaged on a whole tissue (top) or single cell basis (bottom). Scale bar represents either 200 μm (top) or 5 μm (bottom). **(B)** Tissue sections from part **(A)** were stained for Rab5 or Rab7 (green) for early or late endosomes, respectively. Scale bar represents 5 μm. Cropped regions are magnifications of white boxes in whole cell images with intensity profiles along the direction of the white arrow. **(C)** Mander's colocalization coefficient and Pearson's correlation between light chain mRNA and Rab5 or Rab7. Dotted line indicates 0 correlation. n ≥ 10 cells per group. Error bars represent 95% confidence interval. Asterisk indicates $p < 0.05$ by two-tailed t-test. **(D)** Mice lungs were transfected with either sPali (top) or aPali (bottom) mRNA using Viromer Red. At 4 hours, tissue sections were stained for the expressed antibody (white). Scale bar represents 25 μm. **(E)** Mice lungs were transfected with aPali heavy chain and V5 tagged light chain mRNA. Flow cytometry was performed on dissociated lungs stained for V5. Histograms of V5 intensity were normalized to the mode of intensity.

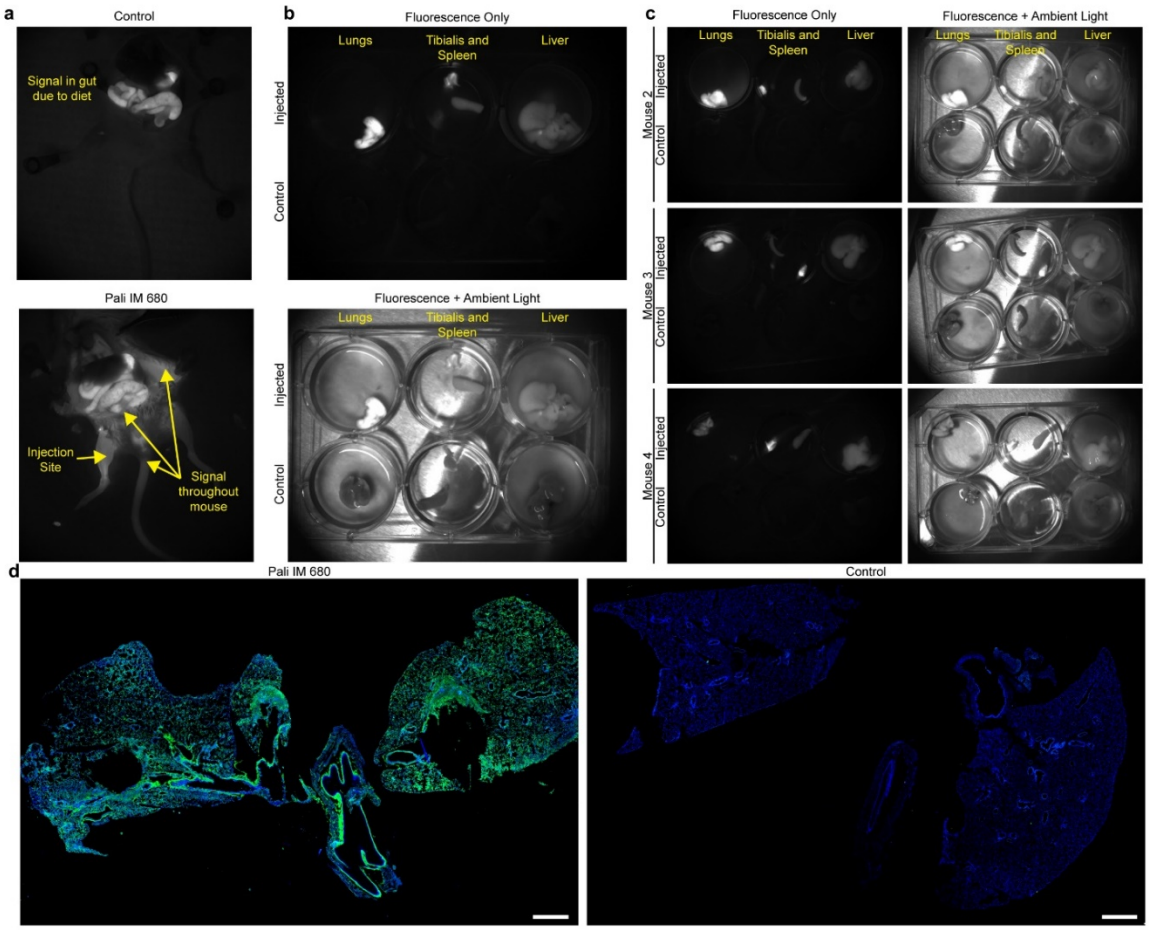

Figure 3.7. NearIR labeled palivizumab biodistribution. (A) DyLight 680 labeled palivizumab was delivered into the tibialis of mice. Saline was injected as a negative control. After 24 h, mice were sacrificed and dissected. Mice were imaged using the Fluobeam Near-IR imager. In both animals, the gut is fluorescent due to the diet. **(B)** Specific organs from injected animals, including the lungs (left), injected tibialis muscle, spleen (middle), and liver (right) were excised and imaged. Images were taken with the ambient light off (top) and on (bottom) to provide context for the control animals. **(C)** Three other mice were processed and imaged as in part **(B). (D)** DyLight 680 labeled palivizumab (green) was delivered into the tibialis of mice (left). Saline was injected as a negative control (right). At 24 hours, lungs were excised and cryosectioned before being imaged. Scale bar represents 750 μm.

Optimizing mRNA delivery vehicle and dosage

To optimize the delivery of therapeutic mRNA to the lung, we compared several mRNA formulations and doses. We first aimed to find the optimal delivery vehicle for aerosol-mediated transfection into the lungs, which would yield effective inhibition of RSV infection. We evaluated several commercially available vehicles including VR and *in vivo*-jetPEI, both PEI derivatives, as well as naked mRNA delivery in water. We transfected mice intratracheally with 40 μg of aPali mRNA, and after 24h, they were infected with RSV L19 intranasally. All three delivery vehicles significantly reduced RSV F copy numbers compared to the saline positive control (Figure 3.8A). Specifically, naked mRNA and mRNA delivered by VR reduced RSV F mRNA copy number by 91 and 96%, respectively. Additionally, only naked and VR delivered mRNA significantly reduced RSV viral titers in lung homogenate supernatants, by 75.4% and 74.2% respectively (Figure 3.8B). To determine the immunological effects of the delivery vehicles and mRNA, we measured the mRNA levels of interleukin 6 (IL-6), RANTES, and interferon gamma (IFNg) and beta (IFNb) and found that *in vivo*-jetPEI increased IFNb mRNA levels by 257-fold, commensurate with a significant decrease in body weight on days 1 and 2 post transfection (Figure 3.8C, Figure 3.9). The increase in IFNb mRNA levels indicated an increase in immune activation, which was not observed using VR or naked mRNA delivery. Finally, to investigate the extent of RSV infection, we also cryosectioned and immunostained lungs from each group using a pan-RSV polyclonal antibody. While both the saline positive control and *in vivo*-jetPEI groups yielded multiple pockets of infection throughout the lung, minimal RSV staining was observed when aPali mRNA was delivered either by VR or naked, with the latter having the more dramatic impact (Figure 3.8D). To minimize immunological risk, maximize prevention of RSV infection, and increase translational suitability, naked mRNA delivery was used for subsequent experiments.

Next, we optimized the mRNA dose by delivering 20 or 100 μg of aerosolized aPali mRNA, intratracheally. To compare the therapeutic effect of aPali mRNA to injected palivizumab, we also administered 15 mg/kg (300 μg for a 20 g mouse in 25 μl of saline) of antibody by IM injection into the tibialis muscle. At 4 dpi, mice were sacrificed and lungs were excised, processed for mRNA extraction, and total RSV F mRNA copy number was measured by qRT-PCR. We found that 100 μg of aPali mRNA significantly reduced RSV F copy number by 90% (Figure 3.8E). Remarkably, delivering 100 μg of aPali mRNA was more effective at reducing RSV replication than palivizumab given IM.

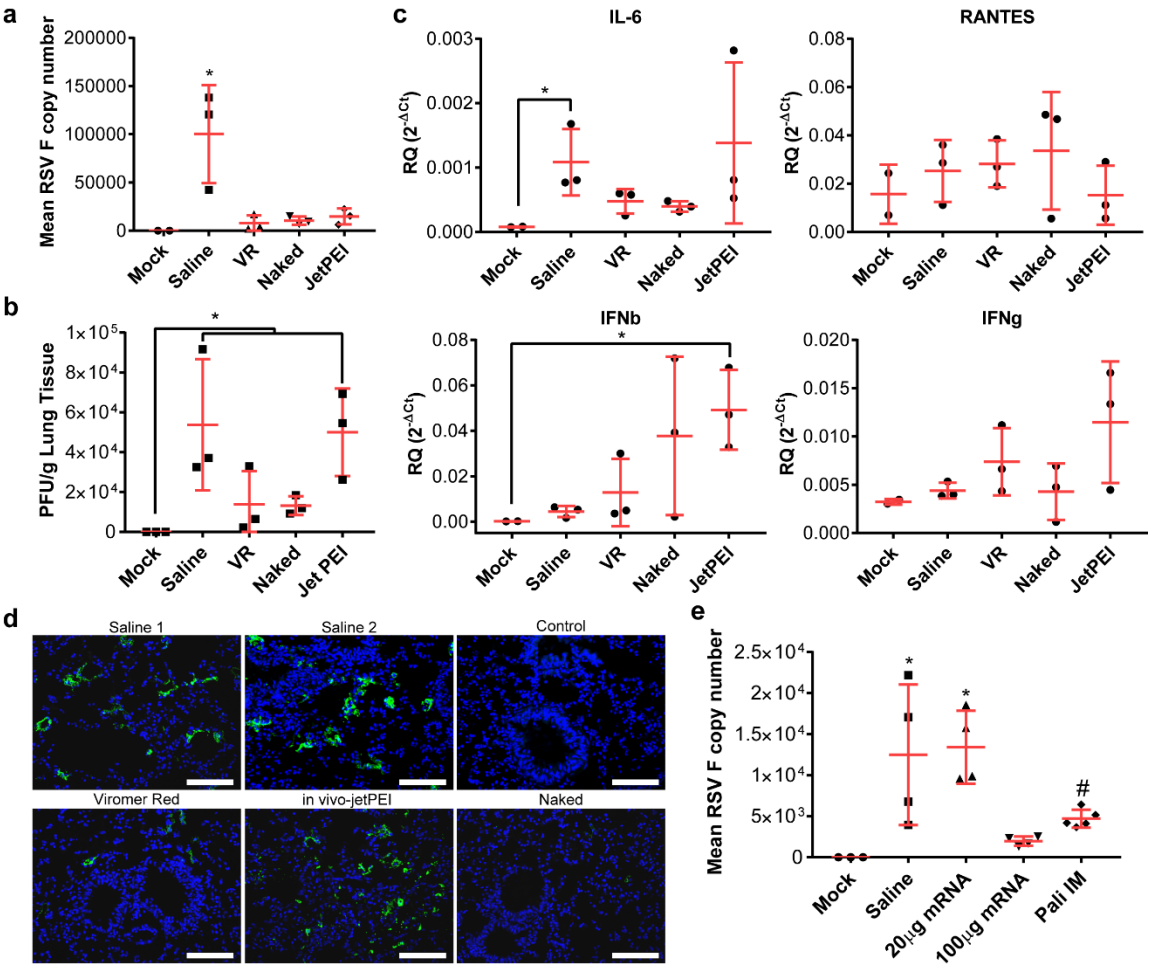

Figure 3.8. Optimizing mRNA delivery vehicle and dosage. (A) Mice lungs were transfected with 40 μg of aPali mRNA using the indicated delivery vehicles. Saline and negative controls are indicated. 24 hours later, mice were infected with RSV L19. At 4 days post infection, mice were sacrificed and lungs were excised and processed for mRNA extraction. Mean RSV F copy number was determined by qRT-PCR. Error bars represent standard deviation. Asterisk indicates $p<0.05$ (one-way ANOVA, Tukey's multiple comparisons). **(B)** The same mouse lungs from part **(A)** were processed and RSV virions were measured by plaque assay. Error bars represent standard deviation. Asterisk indicates $p<0.05$ (one-way ANOVA, Tukey's multiple comparisons). **(C)** Mice lungs from part **(A)** were analyzed by qRT-PCR for the relative quantity of mRNA for IL-6, CCL5, IFNg, and IFNb. Error bars represent standard deviation. Asterisk represents $p<0.05$ (Kruskal-Wallis, Dunn's multiple comparisons). **(D)** Mice lungs were transfected as in part **(A)**. Lungs were processed for cryosectioning and stained with panRSV antibody (green). Scale bar represents 100 μm. **(E)** Mice lungs were transfected with 0, 20, or 100 μg of aPali mRNA using the indicated delivery vehicles. Palivizumab injection IM was included as a positive control. 24 hours later, mice were infected with RSV L19. At 4 dpi, mice were sacrificed and lungs were excised and processed for mRNA extraction. Mean RSV F copy number was determined by qRT-PCR. Error bars represent standard deviation. Asterisk indicates $p<0.05$ (one-way ANOVA, Tukey's multiple comparisons). # indicates no significant difference from any group.

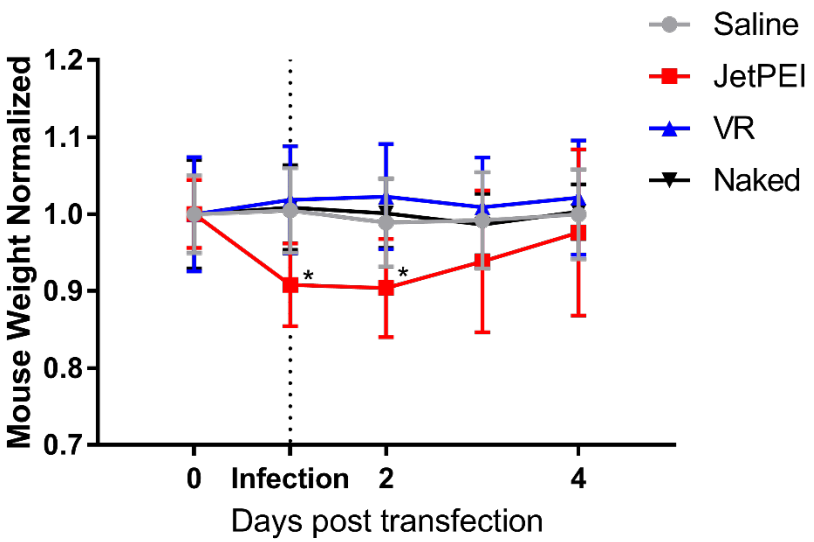

Figure 3.9. Use of in vivo-jetPEI results in rapid weight loss in transfected mice. Mice from the experiment in Fig. 4a were weighed each day after transfection. Weights were normalized by the mean of day 0 in each group. Y-axis begin at 0.7 to better show the differences in weight between the treatment groups. Error bars represent 95% confidence interval. Asterisk indicates $p<0.05$ (two-way ANOVA, Tukey's multiple comparisons).

mRNA-expressed palivizumab prevents RSV infection *in vivo* with minimal cytokine response

We then compared the RSV-neutralizing ability of aerosolized aPali mRNA and sPali mRNA (100 μg) to IM palivizumab (300 μg) and saline controls, given prophylactically. Twenty four hours post-delivery, mice were infected with RSV L19. Mice were sacrificed and lungs excised at 4 dpi and processed for cryosectioning, protein and virus collection, and RNA extraction. We found that aPali and sPali mRNA significantly reduced viral titers by 65% and 89%, respectively (Figure 3.10A), when supernatants were analyzed for virion production. As expected, palivizumab IM yielded no detectable plaques, due to free antibody neutralization of RSV virions directly in the supernatant. All treatments significantly limited RSV replication in the lung (Figure 3.10B), reducing RSV F copy number by approximately 90%. Next, the RSV infections and treatments were evaluated microscopically. We found that while bright pockets of RSV infection throughout the tissue were visible in the saline control group, aPali and sPali mRNA delivery significantly reduced the RSV staining (Figure 3.10C, Figure 3.11); specifically, aPali reduced the volume of RSV signal by more than 70% (Figure 3.10D-E). The safety of mRNA delivery to the lung was also assessed by measuring cytokine protein concentrations 5 days post transfection using a multiplexed immunoassay. None of the measured cytokines, RANTES, IL-12 p70, MIP-1α, and IL-6, were statistically different from mock transfected cells (Figure 3.12). Overall, we have demonstrated that mRNA-expressed neutralizing antibodies in the lung are an effective method of preventing RSV infection *in vivo* without inducing adverse cytokine responses.

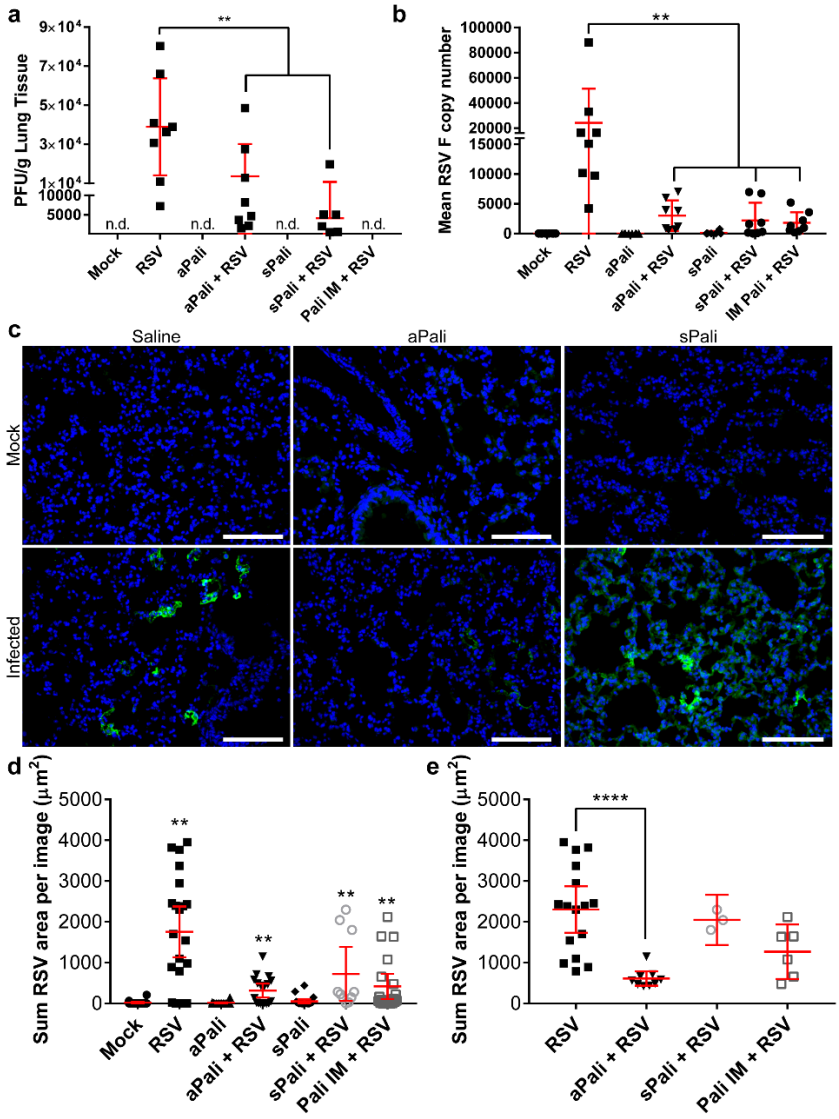

Figure 3.10. mRNA-expressed palivizumab prevents RSV infection in vivo with minimal cytokine response. Mice lungs were transfected with 100 µg of naked aPali mRNA. Saline and negative controls are indicated. 24 hours later, mice were infected with RSV L19. At 4 days post infection, mice were sacrificed and lungs were excised. A total of 10 mice were used per group, out of which, 8 were processed for mRNA, protein, and virion extraction, with 2 being prepared for cryosectioning. **(A)** Virion content of mice lung homogenate supernatants was assayed by plaque assay. Error bars represent standard deviation. Asterisk indicates $p<0.01$ (one-way ANOVA, Tukey's multiple comparisons). **(B)** Mean RSV F copy number was determined by qRT-PCR. Error bars represent standard deviation. Asterisk indicates $p<0.01$ (one-way ANOVA, Tukey's multiple comparisons). **(C)** Cryosections were stained with panRSV antibody (green). Scale bar represents 100µm. **(D)** Quantification of mean volume of RSV signal per frame from microscopy images in part **(C)**. Error bars represent 95% confidence intervals. Asterisks indicate $p<0.01$ (Kruskal-Wallis, Dunn's multiple comparisons). **(E)** For thresholded comparison, images with less than 400 μm^3 signal were excluded. Error bars represent 95% confidence intervals. Asterisks indicate $p<0.0001$ (Kruskal-Wallis, Dunn's multiple comparisons).

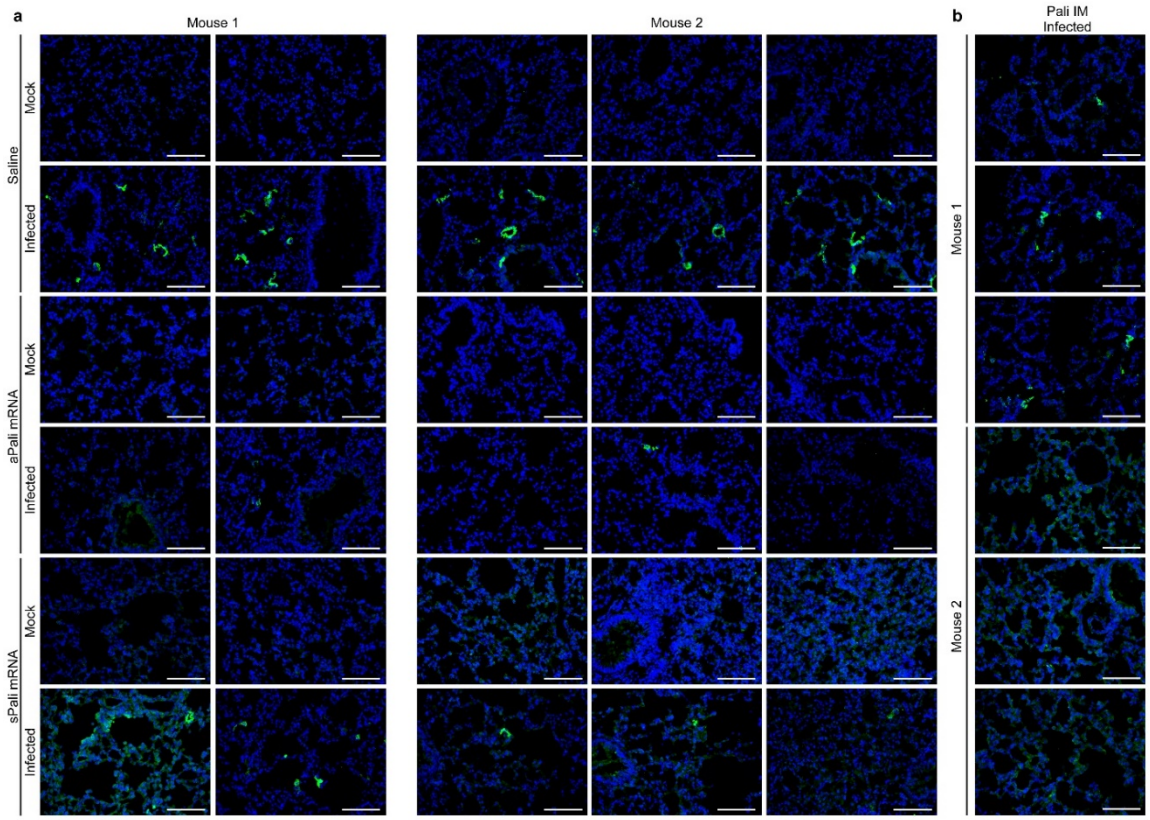

Figure 3.11. Extent of RSV infection in transfected mice. (A) Additional tissue sections were imaged from the experiment in Fig. 5d. Staining for panRSV is in green. Scale bar represents 100 μm. **(B)** Mice were injected IM into the tibialis muscle with 300 μg of palivizumab and infected with RSV L19 the next day. At 4 dpi, animals were sacrificed and lungs were excised, cryosectioned and stained with panRSV (green). Scale bar represents 100 μm.

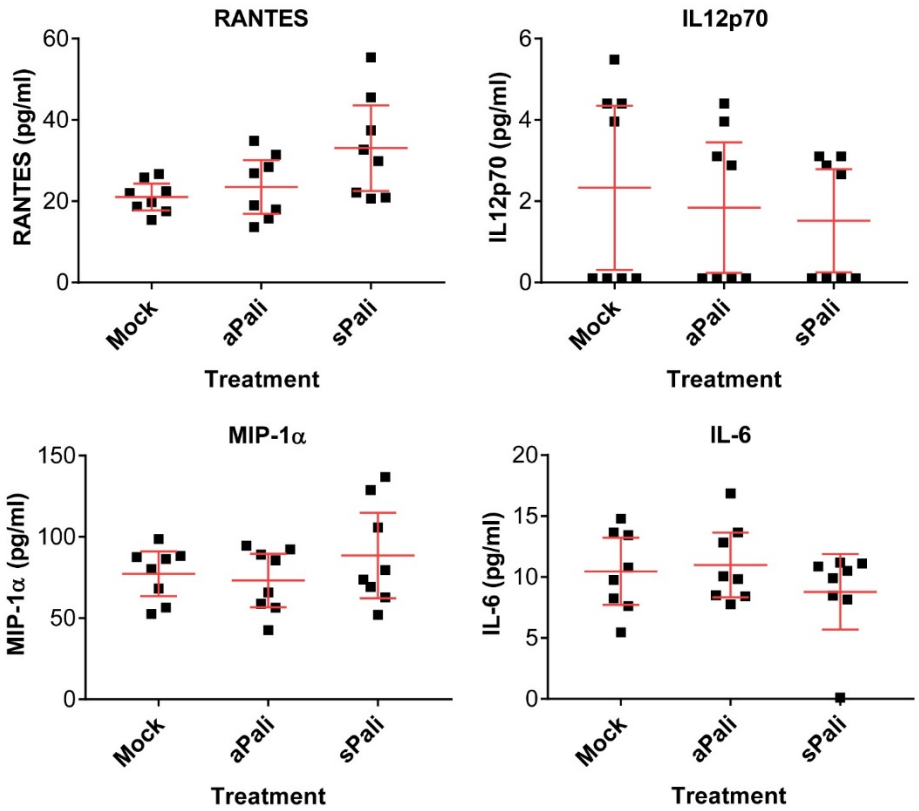

Figure 3.12. Cytokine protein levels in transfected and infected mice. Lung homogenates were analyzed by bead-based immunoassay for cytokine protein levels of RANTES, IL12 p70, MIP-1α, and IL-6. Error bars represent 95% confidence intervals. Undetermined values were set to 0.1 pg/mL. No group was found to be significantly different from another (Kruskal Wallis).

Adapting the GPI anchor to single-chain antibodies

To demonstrate that the GPI anchor is adaptable to other classes of neutralizing antibodies, we designed and produced an mRNA encoding for a newly discovered single-domain camelid antibody (VHH), capable of neutralizing RSV at much lower antibody titers, linked to the DAF GPI membrane anchor sequence, termed aVHH[119]. Single chain antibodies offer several advantages over whole IgG for mRNA delivery, including: (1) they are much smaller than whole IgG, so that more molecules are delivered per gram of mRNA (2) shorter mRNAs are translated more efficiently due to increased ribosome density, and (3) single chain antibodies are expressed by a single mRNA and thus do not require heavy and light chain association to actively bind antigen[121]. Like aPali, the expressed aVHH was primarily localized to the plasma membrane *in vitro*, and protected cells from RSV infection (Figure 3.13A), as demonstrated by the quantification of the RSV N volume in either untransfected or transfected cells (Figure 3.13B). Importantly, the RSV N signal observed in cells transfected with aVHH was derived only from the initial virus inoculum; no detectable replication occurred in the transfected cells. Delivery of aVHH mRNA drastically reduced RSV titer, with 3 of the 6 replicates producing no detectable plaques (Figure 3.13C). Additionally, aVHH mRNA transfection significantly reduced RSV F copy number in infected cells, by 81.8%, compared to untransfected controls (Figure 3.13D). These data indicate that delivery of aVHH mRNA potently inhibited RSV infections in transfected cells.

Finally, to demonstrate that aVHH mRNA is also effective as a prophylactic *in vivo,* we delivered 100 μg of aVHH or aPali mRNA by intratracheal aerosol to mice lungs. One day later, we infected the animals with RSV L19. At 4 dpi, animals were sacrificed and their lungs were excised and prepared for microscopy, qRT-PCR, and plaque assay. First, we found that aVHH was readily detectable by immunofluorescence in transfected lungs, increasing in brightness from 1 day to 5 days post transfection (Figure 3.13E). Additionally,

aVHH mRNA delivery reduced RSV staining compared to untransfected controls at 4 dpi. Both RSV titer and RSV F copy number from animals treated with aVHH mRNA were not significantly different from mock infected mice (Figure 3.13F-G). Overall, these data demonstrate that (1) the GPI anchor sequence can be used interchangeably between whole IgG and single chain antibodies, and (2) mRNA-expressed aVHH is highly effective at preventing RSV infection both *in vitro* and *in vivo*.

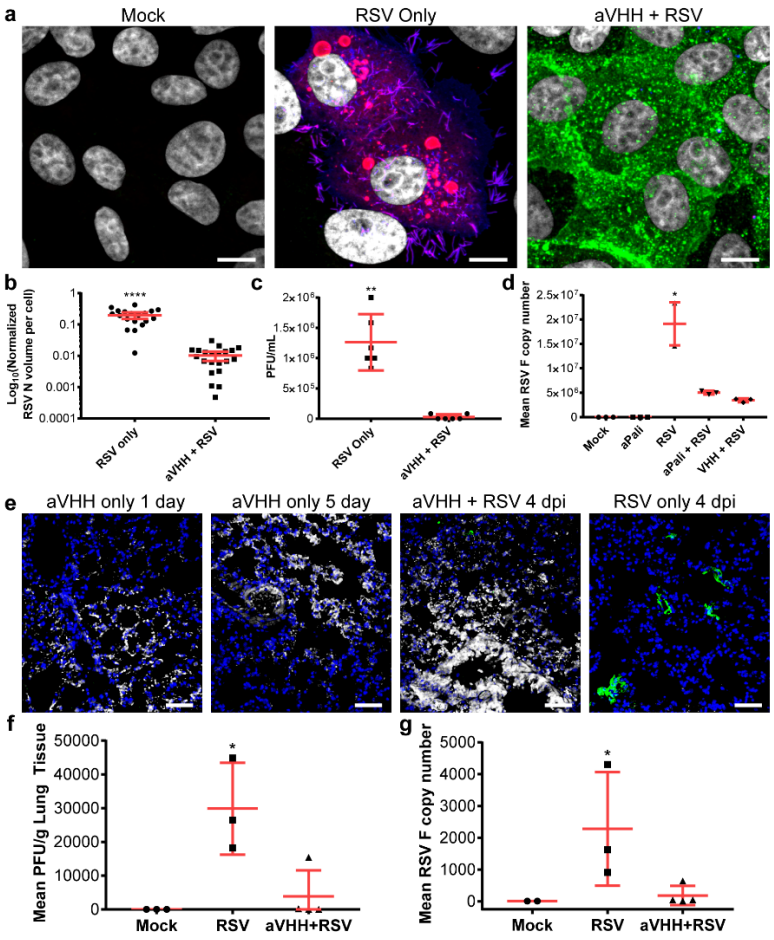

Figure 3.13. Adapting the GPI anchor to single-chain antibodies. (A) Cells were transfected with vehicle control or 1 µg aVHH mRNA. After overnight incubation, cells were infected for 24 h before being fixed and stained for RSV N (red), panRSV (blue), and aVHH (green). Scale bar represents 10 µm. **(B)** Quantification of mean volume of RSV N signal per cell from microscopy images in part **(A)**. Error bars represent 95% confidence intervals. Asterisks indicate p<0.0001 (Mann-Whitney U test). **(C)** Cells were transfected with vehicle control or 1 µg of aVHH mRNA and infected with RSV at MOI of 0.1 before being analyzed by plaque assay. Error bars represent standard deviation. Asterisks indicate p<0.01 (Mann-Whitney U test). **(D)** Cells were transfected with vehicle control or 1 µg of either aPali or aVHH mRNA. Cells were infected with RSV for 24 h before RNA was isolated. Mean RSV F copy number was determined by qRT-PCR and normalized to the mock control group. Asterisk indicates p<0.05 (Kruskal-Wallis test, Dunn's multiple comparisons test compared to mock). **(E)** Mice lungs were transfected with saline or 100 µg of naked aVHH mRNA. Uninfected mice were sacrificed on days 1 and 5 post transfection. 1 day after transfection, mice were infected intranasally with RSV L19. Lungs were cryosectioned and stained for aVHH (white) and panRSV (green). Scale bar represents 50 µm. **(F)** Infected mice lung homogenate supernatants from part **(E)** were analyzed by plaque assay. Error bars represent standard deviation. Asterisk indicates p<0.05 (Kruskal-Wallis test, Dunn's multiple comparisons test compared to mock). **(G)** Infected mice lung homogenates from part **(E)** were analyzed by qRT-PCR for mean RSV F copy number. Error bars represent standard deviation. Asterisk indicates p<0.05 (Kruskal-Wallis test, Dunn's multiple comparisons test compared to mock).

Conclusion

To our knowledge, this study is the first instance of mRNA-based expression of neutralizing antibodies in the lung to prevent viral infections *in vivo*. We demonstrated that GPI-anchored mRNA-expressed antibodies are retained on the plasma membrane of transfected cells, and we report that expressed neutralizing antibodies with and without a plasma membrane anchor can prevent infections *in vitro* and *in vivo*, in an RSV model system. We determined that aPali inhibited RSV by preventing fusion of viral particles with the membrane of transfected cells. In addition, we found that mRNA-expressed neutralizing antibodies did not alter baseline cytokine levels, an important safety concern as undesirable inflammation could limit the translational application of this approach. We also showed that the GPI anchor is adaptable to other types of neutralizing proteins, such as highly-potent neutralizing VHH antibodies, where lung retention was greatly enhanced compared with historical half-life data for VHH antibodies. Theoretically, since the delivery characteristics are based on the mRNA properties, many expressed therapeutic proteins could be anchored in such a manner.

Interestingly, we found that expressing antibodies with the GPI anchor resulted in far less accumulation of the antibody in the ER and secretory membrane system compared to the secreted antibody. As we only evaluated the DAF GPI linker, we can only speculate if the improved trafficking is linker specific, but it is clear that the linker effected the localization. It is possible that the linker is improving antibody assembly, as the heavy chains may be less mobile in the lumen of the ER, promoting heavy and light chain interactions, and may improve trafficking to the plasma membrane[117]. Future work will focus on linker effects on the efficiency of antibody assembly when expressed from mRNA. Linkers with higher cleavage rates could be incorporated to more reliably liberate the antibody from the cell in cases where secretion is critical.

In addition, our mRNA imaging data suggested that approximately half of the naked mRNA, when delivered by aerosol to the lung, was free of the endosomal compartment, in contrast to typical nanoparticle delivery[122,123], where only a small fraction of RNA is delivered to the cytosol. This was a surprising result, and clearly indicates that further research should focus on how droplet size, velocity, and buffers are facilitating cytosolic delivery. We did find though, that Viromer RED delivery of aPali mRNA was equally as effective at preventing RSV infection as naked mRNA delivery, and that *in vivo*-jetPEI exacerbated cytokine responses and did not significantly reduce viral titers, indicating the importance of the delivery approach on outcomes and safety.

While previous studies have used GPI-anchored antibodies for high-throughput screening purposes and HIV inhibition *in vitro*, we report here the first use of antibodies anchored to the surface of cells as a prophylactic approach for lung infections[124,125]. Importantly, expressing anchored neutralizing antibodies on the surface of lung cells provides several benefits over systemic delivery by: (1) preventing the neutralizing antibody from diffusing away from the tissues infected by viruses, (2) raising the local concentration of antibody in the target organ, and (3) are likely increasing the time that neutralizing antibodies are present on the mucosal surface. Together, these benefits point to a prophylactic approach that has the potential to be more efficacious than systemic neutralizing antibody delivery, while avoiding systemic delivery. Taking into account that children receive 15 mg/kg of palivizumab during treatment, this could lead to significant cost reduction and mitigate the risk of anti-human antibody responses.

These properties were even more important in the case of single chain antibodies. Single chain antibodies are smaller than whole immunoglobulins, have larger diffusion rate constants, and are cleared much more rapidly, with serum half-lives ranging from 30 min to 2 h[126–128]. Anchoring these small, high-affinity, neutralizing antibodies to the plasma membrane overcame these issues while allowing for more mRNA copies to be delivered

per equivalent mass. We found that aVHH mRNA delivery was highly effective at mitigating RSV infection both *in vitro* and *in vivo*. Critically, aVHH mRNA delivery and infection with RSV resulted in statistically similar data as mock infected animals by both plaque assay and qRT-PCR. We also demonstrated retention of the aVHH on lung cells 5 days post transfection. Additionally, in cases where the Fc region of the antibody enhances neutralization of the pathogen, such as HIV, anthrax, and influenza, a sequence encoding the Fc could be inserted between the single-chain antibody coding region and the GPI anchor sequence[129–132]. Because they do not rely on heavy and light chain association, sequences encoding single chain antibodies also offer the ability to multiplex several anchored neutralizing antibodies in a single cocktail, either for targeting multiple pathogens or additional virus strains.

Here we used RSV as a model system to test the prophylactic benefits of synthetic mRNA-expressed neutralizing antibodies. However, it is important to stress that mRNA encoding broadly neutralizing antibodies that target other viruses can be used to prevent infection, such as influenza or human metapneumovirus[133]. Additionally, the membrane anchor can be easily adapted to other neutralizing antibodies or proteins in cases where systemic antibody therapy is undesirable. Moreover, we emphasize the use of the anchor on single chain antibody constructs, which will allow for multivalent prophylaxis against additional pathogens and viral strains. Overall, pulmonary expression of neutralizing antibodies is a new prophylaxis tool that can protect the lung from infection and is adaptable to other viruses and antibodies.

Methods

Cell lines and virus culture

Vero cells (African green monkey kidney cells, American Type Culture Collection CCL-81) or HEp-2 (human epithelial cells, ATCC CCL-23) were cultured in DMEM (Lonza) supplemented with 10% fetal bovine serum (FBS) (Hyclone) and 100 U mL^{-1} penicillin and

100 mg mL^{-1} streptomycin (Life Technologies). Cells were plated on No. 1.5 coverslips (Electron Microscopy Sciences) one day prior to infection. Both Vero and HEp-2 cell lines were authenticated by ATCC and were checked for Mycoplasma contamination in our laboratory. HEp-2 cells are commonly used to propagate RSV in culture.

Human RSV A2 (ATCC VR-1544) and human RSV L19 (a gift from Martin L. Moore's lab, Emory University) was propagated in HEp-2 cells when the cells were >80% confluent. The media was removed and cells were washed with DPBS (without Ca^{2+} and Mg^{2+}, Lonza), and virus was added at a multiplicity of infection (MOI) of 0.1 for 1 h before adding complete medium to the inoculum. Cell-associated virus was harvested by scraping the cells when about 90% of cytopathic effects was visualized (about 96 hpi). Virus was then vortexed briefly, aliquoted, and stored at -80 ºC. For L19 virus, the cell suspensions were sonicated at 30% amplitude, with 1 second on/off pulses and centrifuged at 800x g at 4 °C. Supernatants were pooled and 1mL aliquots were snap frozen in liquid nitrogen and stored at -80 ºC. Virus titers were measured via plaque assay.

Antibodies

For immunostaining, primary antibodies used were mouse anti-RSV N (Abcam, Cat. No. ab22501), mouse anti-RSV G (Abcam, Cat. No. ab94966), rabbit anti-camelid VHH (GenScript, Cat. No. A01860-200), goat anti-panRSV polyclonal (Millipore, Cat. No. AB1128), rat anti-CD63 (BD, Cat. No. 564221), rabbit anti-Rab5 (Affinity BioReagents, Cat. No. PA3-915), and rabbit anti-Rab7 (Abcam, Cat. No. 137029). All primary antibodies for immunostaining experiments were used at 1 µg/mL. Secondary antibodies used were donkey anti-human Alexa Fluor 647 (Jackson ImmunoResearch), donkey anti-goat Alexa Fluor 546, donkey anti-rabbit Alexa Fluor 488, and donkey anti-mouse Alexa Fluor 488 (all from Life Technologies). All secondary antibodies for immunostaining experiments were used at 4 µg/mL. For dSTORM experiments, secondary antibodies used were

donkey anti-mouse Alexa Fluor 647 (Life Technologies) and goat anti-human CF568 (Biotium), and both were used at 1 µg/mL.

Construct preparation for in vitro transcription

Plasmids for IVT were designed using the full length nucleotide sequences of palivizumab heavy and light chain. The coding region was preceded by 5' UTR with Kozak sequence and followed by a 3' untranslated region (UTR) derived from the mouse alpha globin sequence. Sequences were human codon optimized and inserted in a pMA-7 vector (Thermo Fisher Scientific, GeneArt) to be used as a template for mRNA synthesis. For the anchored version of palivizumab, a GPI linker based on the human decay accelerating factor (DAF) was appended to the Fc region of the heavy chain and synthesized in the same manner as the secretory version[134].

V5 peptide tag addition (PCR)

V5 is a 14 amino acid epitope tag that was inserted into the 3' terminus of the light chain construct through two fragment Gibson assembly. The linear backbone was PCR amplified from the insertion site in the forward and reverse directions (primers 1 and 2, Table 3.1). The insert was 104 bp in size – 42 bases for the V5 tag and 31 x 2 bases for the overlapping segments that correspond to the aPali light chain backbone. This insert was synthesized via PCR (primers 3 and 4, Table 3.1). All PCR products were 0.8% agarose gel purified.

The backbone was assembled with 3x molar excess of insert in 5 µL total volume of NEBuilder® HiFi DNA Assembly Master Mix, according to NEB's protocol. After incubation for 1 hour at 50C, 1 µL of reaction mixture was used to transform NEB 5-alpha competent *E. Coli*. Ampicillin plates were used to select 10 colonies and outgrowth performed at 30C for 24 hours. Subsequent plasmids from each colony were Sanger sequenced to ensure incorporation of the V5 tag at the 3' terminus of the light chain.

Immunofluorescence staining confirmed that V5 tag insertion did not negatively impact heavy and light chain association or ability to knock down RSV infection.

Gibson assembly of aVHH construct

The anchored VHH sequence, F-VHH-4 from Rossey et al., flanked by UTRs, was ordered as a DNA geneblock from IDT[119]. The geneblock was PCR amplified with primers that contained overlapping regions for the PMA-7 vector (primers 5 and 6, Table 3.1). This aVHH PCR product was cloned into the PCR amplified pMA7 vector (primers 7 and 8, Table 3.1) through Gibson assembly using NEB Builder with 3x molar excess of aVHH insert, as described above. All reaction transcripts were 0.8% agraose gel purified prior to assembly reaction. Subsequent plasmids from each colony were Sanger sequenced to ensure desired sequence fidelity.

Table 3.1. Primers used for construct synthesis and PCR. All sequences are presented in 5' to 3' direction. *These sequences are from Mentel *et. al.*[135].

Primer 1	Forward Primer for pMA7:VHH LC at 3' end insertion site	TGATAAGCTGCCTTCTGCGGGGCTTGCCTTC
Primer 2	Reverse Primer for pMA7:VHH LC at 3' end insertion site	GCACTCGCCCCGGTTGAAGCTCTTGGTCACG
Primer 3	Forward Primer to create insert with V5 tag	CGTGACCAAGAGCTTCAACCGGGGCGAGTGCGGCAAG CCCATCCCCAACCCCCTGCTGGGCCTGGACAGCACCTG
Primer 4	Reverse Primer to create insert with V5 tag	GAAGGCAAGCCCCGCAGAAGGCAGCTTATCAGGTGCTG TCCAGGCCCAGCAGGGGGTTGGGGATGGGCTTGCCGC
Primer 5	Forward Primer to place pMA7 overlaps on 5' end of VHH geneblock	GCGACGATTGGCGGAAGGCCGTCAAGGCCGCATTTTTA AG
Primer 6	Reverse Primer to place pMA7 overlaps on 5' end of VHH geneblock	CGGGCAGTGAGCGGAAGGCCCATGAGGCCCAGTTTTTG
Primer 7	Forward Primer for to amplify linear pMA7 PCR product	GGCCTTCCGCTCACTGCC
Primer 8	Reverse Primer for to amplify linear pMA7 PCR product	GGCCTTCCGCCAATCGTC
Primer 9	RSV F gene (standard) Forward	CTTTCTTCCCACAAGCTGAAAC
Primer 10	RSV F gene (standard) Reverse	GTGGTGGATTTACCAGCATTTAC
Primer 11	RSV F-qPCR Forward*	AACAGATGTAAGCAGCTCCGTTATC
Primer 12	RSV F-qPCR reverse*	CGATTTTTATTGGATGCTGTACATTT
Probe	RSV F probe*	TGCCATAGCATGACACAATGGCTCCT

Synthetic mRNA in vitro transcription

Plasmids were linearized with Not-I HF (New England Biolabs) overnight and PCR purified using PCR clean-up kit (Qiagen), prior to in vitro transcription (IVT) using a T7 mScript kit (Cellscript) following the manufacturer's instructions. Equimolar ratios of ATP, GTP, and CTP were used alongside N1-methylpseudouridine-5'-triphosphate (TriLink). RNAs were capped using 2'-O-Methytransferase followed by enzymatic addition of a poly-A tail, both according to the mScript kit instructions. The capped and tailed mRNAs were then purified using an RNeasy kit (Qiagen) and treated with Antarctic Phosphatase (New England Biolabs) for 1 hour (New England Biolaboratories), and purified again. RNA concentration of the purified mRNA was measured the RNA was stored at -80 °C until further use.

Transfections in vitro

Vero cells were transfected using either Viromer Red (Lipocalyx) or Neon electroporation system (Invitrogen), according to the manufacturer's instructions, into a 24 well plate (for imaging and plaque assays) and were transfected with 1 µg of mRNA per 200,000 cells. For mRNA encoding whole IgG, heavy chain and light chain mRNAs were combined in a 4:1 mass ratio for equimolar conditions. Twenty hours post-transfection, cells were fixed and immunostained with or without permeabilization.

Immunostaining

Vero cells were fixed with 4% paraformaldehyde (PFA) (Electron Microscopy Sciences) for 10 min at room temperature before permeabilization with 0.2% Triton X-100 (Sigma) for 5 min at room temperature. Then, cells were blocked by incubation with 5% bovine serum albumin (Calbiochem) for 30 min at 37ºC before being incubated with primary antibody for 30 min at 37 ºC. Cells were then washed with PBS and incubated with secondary antibody for 30 min at 37 ºC. Multiple antibody labeling was performed simultaneously after checking cross-reactivity. Nuclei were then stained with 4',6-

diamidino-2-phenylindole (DAPI) (Life Technologies), and coverslips were mounted onto glass slides with Prolong Gold (Life Technologies).

Plaque assay

For mRNA knockdown of viral titer *in vitro*, Vero cells were transfected with or without aPali or aVHH mRNA, using the Neon system, into a 24 well plate and incubated until fully confluent. Either 50 µL of serially diluted lung supernatant (for *in vivo* studies) or 50 plaque forming units (PFU) or multiplicity of infection (MOI) of 0.01, 0.1 or 1 (for direct measurements or supernatant measurements, respectively) of RSV A2 stock was added to the cells. Cells were incubated at 37 ºC for 1 h with shaking every 15 min. At 1 hpi, 1 mL of overlay media, consisting of either 1.2% Avicel (FMC Biopolymer) or 1.2% methylcellulose (Sigma-Aldrich) in 1X DMEM with 2% FBS and 100 U mL^{-1} penicillin and 100 mg mL^{-1} streptomycin (Life Technologies), was added. At either 6 dpi (RSV for A2) or 8 dpi (for RSV L19), cells were washed and fixed with 4% paraformaldehyde, blocked with 5% BSA, and stained with a goat anti-panRSV polyclonal and HRP-conjugated donkey anti-goat secondary antibody. A precipitating peroxidase substrate (TrueBlue, KPL) was then added and cells were incubated at room temperature for 10 min before a final wash with water. Plaque count was converted using the dilution factor to generate viral titer in PFU/mL and, in the case of *in vivo* assays, lung titers were normalized by lung weights.

Animal studies

Six- to 8-week-old female BALB/c mice (Charles River Laboratories) were maintained under pathogen-free conditions in individually ventilated and watered cages kept at negative pressure. Food was provided to mice *ad libitum*. Animals were acclimatized for at least 6 d before the beginning of experiments. Animals were sacrificed by CO_2 asphyxiation. Infected animals were handled and kept under BSL-2 conditions until euthanized. All animals were cared for according to the Georgia Institute of Technology Physiological Research Laboratory policies and under ethical guidance from

the university's Institutional Animal Care and Use Committee (IACUC) following National institutes of Health (NIH) guidelines. Number of animals used in each experiment is detailed in Table 3.2.

Table 3.2. Number of animals used per experiment

Experiments	Groups	No. of animals per group	Total animals per experiment
aPali Expression using microscopy	Control, aPali and sPali	2 each	6
Vehicle test	Control, RSV, ViromerRed, *invivo*Jet-PEI, Naked mRNA	3 each	15
mRNA titration	Control, 20 µg, and 100 µg	3 control, 4 each amount	11
Palivizumab 680	Control and Palivizumab	3 each	6
mRNA distribution in lung	Control and aPali	2 each	4
aPali expression using Flow Cytometry	Control and aPali	1 control, 3 aPali	4
RSV Challenge	Control, RSV only, aPali, aPali+RSV, sPali, sPali+RSV,	10 (8 for RSV titers and 2 for microscopy)	60
aVHH expression	Control, aVHH, and aVHH+RSV	2 each	6
aVHH Challenge	Control, RSV, aPali, aPali+RSV, aVHH, aVHH+RSV	3 each	18
		Total	**130**

Palivizumab intramuscular injection

Mice were anesthetized under constant isofluorane (Henry Schein Medical) with oxygen and kept on a heating pad. The *anterior tibialis* muscle was then shaved and injected with 15 mg/kg of palivizumab in 25 µL using a 29 gauge needle. Near-IR imaging was performed using a Fluobeam (Fluoptics) on anesthetized mice. Mice were euthanized 24 h post injection and organs were imaged for palivizumab biodistribution in organs pre- and post- harvesting using the Fluobeam.

Intratracheal aerosol mRNA transfections

Mice were anesthetized using 87 mg/kg ketamine and 16 mg/kg xylazine. The trachea was visualized by inverting the mouse on a 45° tilting intubation stand (Hallowell EMC) using the upper teeth and illuminating the trachea with a flex light. A 1.22 mm endotracheal tube (ET, Hallowell EMC) was then inserted to intubate the animal. A MicroSprayer Model IA-1C connected to a High Pressure Syringe Model FMJ-250 (both from PennCentury) was then inserted such that the tip of the sprayer nozzle was 1 mm past the tip of the ET tube. The MicroSprayer was then actuated using a custom Pump 11 Elite Nanomite handheld syringe pump (Harvard Apparatus) that allowed for repeatable pressure and volume delivery of 50 µL. To find the best delivery vehicle, we compared Viromer RED and in vivo-jetPEI against naked mRNA at 40 µg in nuclease free water. For naked mRNA transfections, the appropriate amount of mRNA was mixed with water to the desired concentration. For Viromer RED transfections, 0.2 µL of Viromer RED (Lipocalyx) per 1 µg of mRNA was mixed with Buffer Red. The mRNA, also diluted in Buffer Red, was then added to the Viromer solution, per the manufacturer's instructions. For *in vivo*-jetPEI transfections, 40 µg of mRNA was delivered with 6.4 µL of vehicle diluted in 5% glucose in water. In order to mitigate any possible double stranded RNA-dependent protein kinase (PKR) response, Imidazolo-oxindole PKR inhibitor C16 (Sigma-Aldrich) was added to all

mRNA preparations to a final concentration of 375 μM. To find an optimum mRNA amount for delivery, we tested aPali at 20 μg and 100 μg without any delivery vehicle.

MTRIP labeling of mRNA

MTRIPs were constructed as described previously[93,97,120]. Briefly, we designed four 2' O-methyl RNA-DNA chimeric oligonucleotides, each containing a 17-18 nucleotide binding region and 5-7 poly(T) linker. Oligos were complementary to 4 adjacent sequences across the mRNA 3' UTR regions and contained 3-4 amino-modified thymidines each, as well as a 5' biotin modification (Biosearch Technologies). Labelled oligos were synthesized by conjugating either Cy3B NHS ester (GE Healthcare) or DyLight 650 (Thermo Fisher) to the amine groups on the oligonucleotides following the manufacturer's protocol. Complete MTRIPs were assembled by incubating the labeled oligos with Neutravidin (Pierce) for 1 h at RT followed by filtration using 30 kDa MWCO centrifugal filters (Millipore). mRNA was buffer exchanged into 1X PBS, heated to 70 ºC for 10 min, and immediately placed on ice. Denatured mRNA was then combined with MTRIPs in a 1:1 ratio for each MTRIP and incubated at 37 ºC overnight. Labeled mRNA was then buffer exchanged into water and concentrated using a 30 kDa filter before being injected into the animals.

RSV infections in mice and tissue processing

One day after transfection, mice were anesthetized using cotton soaked with isofluorane in a small chamber. After breathing rate had slowed sufficiently, mice were inoculated with $5x10^5$ PFU of RSV L19 in 50 μL, with 25 μL in each nostril. Mice were weighed before infection and then once daily to monitor weight loss. Mice were sacrificed by CO_2 asphyxiation at 4 dpi. Lungs were harvested in cold DMEM without any supplements and were either stored on ice for imaging or snap-frozen in liquid nitrogen for protein and RNA extractions. Snap frozen tissues were thawed and homogenized using a Gentle MACS Tissue Dissociator (Miltenyi) and centrifuged to collect supernatants

for plaque assay and cytokine analysis. Tissue pellets from this step were used for RNA extraction.

For plaque assay, neat and serially diluted lung homogenates were added to confluent Vero cells and processed as described above. Dilutions with individual plaques were counted and averaged across 4 replicate wells to generate viral titer in PFU/mL. Viral titer was then normalized by lung weight.

Lung tissues collected in DMEM were washed in PBS and fixed in 4% paraformaldehyde overnight. Tissues were then washed three times in PBS and were cryoprotected using 30% sucrose (Sigma) in 1X PBS until tissues sank to the bottom of the container. Tissues were then frozen in OCT compound (Tissue-Tek) and cryosectioned (10 μm sections). Tissue sections were then immunostained as described above.

Flow cytometry

Mice lungs were collected in DMEM and washed to remove any blood. The tissues were then dissociated using the Miltenyi Lung dissociation kit, following manufacturer's instructions with slight modifications[136,137]. Briefly, after coarse digestion of lungs, 0.1 mg/mL soybean trypsin inhibitor (Sigma) 60 U/mL DNAse I and 1mg/mL type XI collagenase was added and tissues were digested at 37°C for 30 min. Then, lungs were finely homogenized in Miltenyi Gentle MACs, followed by addition of 0.1 M EDTA in FBS to inactivate the enzymes. Cell suspension was then passed through 70 μm filter, washed with PBS by centrifugation at 800 xg for 10 min. RBCs were lysed using ACK lysis buffer (Alfa Aesar) and washed with DPBS. Cells were then counted and 1-2 million cells were stained with live/dead marker (Life Technologies) before being incubated with rabbit anti-V5 antibody followed by AlexaFluor 488 conjugated donkey anti-rabbit secondary antibody (Invitrogen). Cells were then fixed with BD Cytofix/Cytoperm (BD Biosciences) and acquired on a BD LSRFortessa flow cytometer. Compensation was performed using

beads (BD Biosciences) labeled with fluorophore conjugated antibodies.Data was analyzed using Flow Jo software (Treestar).

qRT-PCR

Total RNA was extracted from cells or tissues using an RNeasy kit (Qiagen) and cDNA was synthesized using 250 ng of total RNA and a High Capacity cDNA synthesis kit (Applied Biosystems) with random hexamers. Extent of RSV infection was assessed using an absolute quantification method based on RSV F gene copy numbers as described previously[135]. Primers used are in Table 3.1. For cytokine analysis, Taqman gene expression assays were used for IL-6, IFN-β, IFN-γ, and CCL5 (Thermo Fisher).

Bead-based immunoassay

Lung homogenates were assessed for cytokine response using a custom Millipore Milliplex assay following the manufacturer's instructions. Briefly, samples were diluted 1 fold in assay buffer and assayed using a BioPlex 2.0. Observed and interpolated cytokine concentrations were used and undetected cytokines were set as 0.1 pg/mL.

Microscopy

All images were acquired with a Hamamatsu Flash 4.0 v2 sCMOS camera on a PerkinElmer UltraView spinning disk confocal microscope mounted to a Zeiss Axiovert 200M body with either a 63x NA 1.4 plan-apochromat objective for individual cells or a 20X NA 0.8 plan-apochromat objective for tissue sections. All 63x images were acquired with Volocity (PerkinElmer) with Z-stacks taken in 0.2 μm increments. Stitched tissue images were acquired automatically using the motorized ASI PZ-2150 stage in Volocity using 25% overlap with automatic alignment and without background correction. Linear contrast enhancements were applied to images for clarity. Unless indicated, all images in a given experiment were enhanced the same. All image quantification and analysis was completed on unenhanced data.

dSTORM

Images were acquired using a Bruker Vutara 352 with a 63x NA 1.2 plan-apochromat water immersion objective lens kept at room temperature. Samples were immunostained as above, but without nuclear counterstain since the 405 laser is used for dSTORM excitation. Samples were imaged in a buffer to enhance fluorophore blinking which contains: 50 mM Tris-HCl (pH 8.0), 10 mM NaCl, 10% glucose, 20 mM cysteamine, 1% 2-Mercaptoethanol, 169 AU/mL glucose-oxidase, and 1,404 AU/mL catalase. Imaging buffer was prepared fresh daily and replaced after approximately 2 h. All images were acquired and analyzed using the Vutara SRX software. All images were processed using the denoise option set to 0.2. For particle height quantification, a 1 μm square around each individual particle was analyzed. To ensure quantification of RSV virions, particles were only included if the XY FWHM was greater than 50 nm and the Z FWHM was greater than 100 nm. The mean of the aPali signal and mean of the RSV N signal was subtracted to determine mean particle distance above the aPali signal.

Statistical analysis

Results were plotted and statistical analyses were performed using Prism 7 (GraphPad). Hypothesis tests were chosen and performed as appropriate, indicated in the figure captions.

CHAPTER 4

PERSPECTIVES AND FUTURE DIRECTIONS

The work presented here discovered new avenues of RSV biology and prophylaxis, but also inspired many new questions. This chapter will review the accomplishments of this work and some of the future research enabled by the findings. These perspectives will be divided into several broad categories: enabling high resolution RSV G imaging, RSV G interactome analysis, and mRNA delivered anchored neutralizing antibody prophylaxis and treatment.

Enabling high resolution RSV G imaging

First, we discovered that lectin conjugates can specifically bind RSV G on both infected cells and virions, and we found that this binding does not inhibit either infectivity or replication of the virus. We then used fluorescent lectin conjugates to obtain the first live images of wild-type RSV filament formation in cells, discovering that this process is microtubule, and specifically dynein, dependent. We found that many of the viral proteins involved with RSV assembly of mature virions colocalize with vesicles involved in filament formation. We observed that, during endosomal recycling, RSV G is first bound to clathrin during endocytosis, but is associated with caveolar membranes in mature virions. Finally, we recorded, for the first time, that RSV genomic RNA is loaded into extended RSV filaments, and that this process is also governed by microtubules. Together, these results indicate that RSV filament formation is not exclusive to the plasma membrane.

While we demonstrate that RSV filaments can be formed intracellularly, we also show that these same filaments protrude out of the plasma membrane during late-stage infections. Our current results do not provide a mechanistic answer for this process, but the first step in providing an explanation for filament translocation to the plasma membrane is understanding the orientation of RSV G on intracellular filaments. We could not directly

determine this partially due to the limited resolution of diffraction-limited confocal microscopy. Therefore, we began efforts to enable high resolution imaging of RSV G. First, we began the process of using gold nanoparticle lectin conjugates to employ cryoEM. The single-nanometer resolution of cryoEM, should provide enough resolution to observe lectin-Au labeled RSV G molecules. Obvious extensions of this method include using dual-labeled lectins, with fluorophores and gold nanoparticles on the same lectin molecule, to enable Cryo-CLEM (correlated light and electron microscopy). Cryo-CLEM allows for samples to be investigated first using fluorescence, to obtain the general spatial and temporal location of interest, followed by electron microscopy, to generate the high resolution structural data[29,138].

By enabling high-resolution cryoEM imaging of RSV G, we can observe other points along the RSV life cycle. For instance, the precise entry mechanism of RSV is still debated. Some reports indicate that direct fusion of virions with the plasma membrane is responsible[139,140]. Yet, other studies indicate that clathrin-mediated endocytosis is involved with viral uptake[81,82,141]. Finally, a recent study proposed that a micropinocytosis mechanism is implicated[142]. By labeling virions with lectin-Au conjugates, cryoEM can be utilized to observe the entry mechanism of RSV in cells with wild-type virus and minimal, if any, chemical fixative and permeabilization artifacts.

Finally, in an effort to minimize risk in the event that cryoEM is unfeasible, we will assess the use of dSTORM to localize RSV G on cells. While the lateral resolution of dSTORM is only 20-30 nm compared to ~1 nm in the case of cryoEM, the increased resolution over diffraction-limited microscopy might be sufficient to visualize the populations of RSV G beneath the plasma membrane. Unlike other imaging techniques such as STORM, which relies on photoswitchable dyes, and FPALM, which relies on photoswitchable fluorescent proteins, dSTORM can be used with conventional fluorophores[34,143,144]. The switching characteristics of several conventional dyes, such as

Alexa Fluor 647, has already been characterized[145]. Additionally, the Vutara dSTORM system used in this work is equipped with a biplane module, which allows for enhanced axial resolution (~50 nm) and the ability to localize individual fluorophores in multiple imaging planes[146]. In order to first assess the ability of the dSTORM system to localize RSV G, we will perform initial experiments using RSV infected cells and RSV G transfected cells in order to verify that SBA would be suitable for further experiments.

To these ends, we attempted: 1) adapting SBA to cryoEM by generating gold SBA conjugates and optimizing cell infection and staining conditions, and 2) using fluorescent SBA conjugates to label RSV G on infected cells and on cells transfected with RSV G mRNA (cells thin enough to enable cryoEM imaging).

First, while RSV G localization has been characterized in infected cells using transmission EM (TEM), there have not been any reports of RSV G imaging using cryoEM. Though TEM imaging of RSV first indicated that virion assembly can occur prior to the plasma membrane and that RSV G is present along the membranes of intracellular vesicles, the precise mechanism governing the translocation of progeny from the intracellular space to the plasma membrane has not been delineated[21]. This is likely due to the chemical fixatives and permeabilization techniques required for adequate gold labeling in TEM[147]. Because these chemical-based techniques can result in a loss of ultrastructure, cryogenic freezing of cells is utilized which can maintain structural integrity, resulting in the most accurate representation of cells[148–150]. However, gold labels in cryoEM must be applied to living cells, so intracellular staining can be difficult[151]. Because RSV G recirculates, and SBA can be applied to the extracellular fraction and allowed to internalize, this method could be used alongside a gold-conjugated SBA (SBA-Au) in order to visualize the intracellular localization of RSV G using cryoEM. To begin testing this theory, we first characterized the conjugation of gold nanoparticles to SBA, ensuring that the process did not inhibit the binding of SBA-Au to RSV G. Additionally, in order to confine

sample thickness to the 500-700 nm limit of cryoEM, cell plating strategies, infections, and lectin labeling was assessed prior to attempting cryoEM.

Characterizing the conjugation of gold nanoparticles to SBA

First, we purchased commercially available SBA-Au containing either a 5 or 10 nm gold nanoparticle. When analyzed by high performance liquid chromatography (HPLC), we found that while some SBA-Au samples were quite pure, indicated by a single sharp peak in the chromatogram, others were not, indicated by a broad plateau (Figure 4.1). Because of the variation in SBA-Au purity, we opted to only use either commercially available SBA-Au that had been verified by our HPLC or SBA-Au conjugates that we produced and purified ourselves.

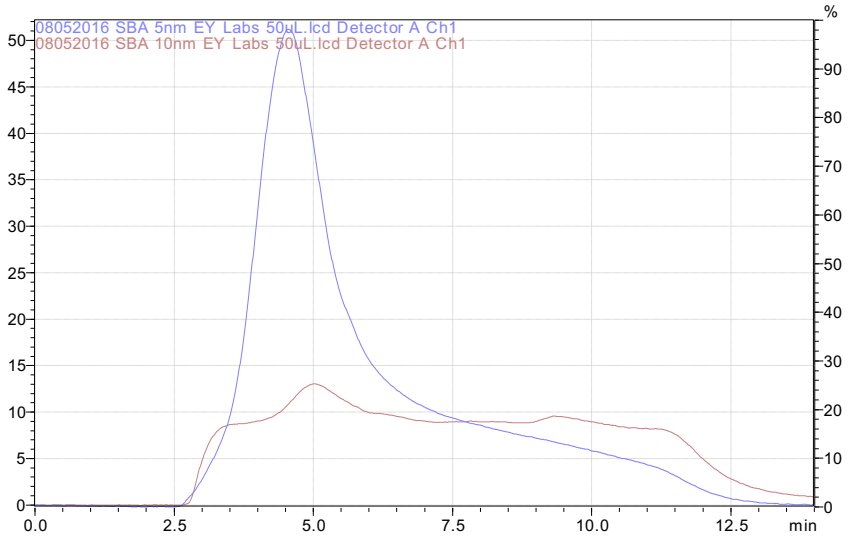

Figure 4.1. Commercially available Au-SBA conjugates vary in purity. 5 (blue) and 10 nm (red) Au-SBA conjugates were analyzed by size-exclusion HPLC. Note that a sharp peak indicates a purer sample, while a plateau shape indicates less purity.

Next, we verified that conjugation of gold nanoparticles to SBA does not inhibit the binding of SBA to RSV G. First, we labeled individual RSV virions with SBA-Au and isolated them onto glass coverslips. The RSV particles were then fixed and

immunostained for RSV F. Localization of gold nanoparticles was then visualized using darkfield microscopy while the immunostained viral proteins were imaged using the widefield epifluorescence light path on the same instrument. We observed that SBA-Au bound to the isolated RSV virions, allowing clear visualization of the viral filaments, though some lectin-gold conjugate bound the glass coverslip nonspecifically (Figure 4.2A). Finally, we ensured that SBA-Au binds RSV G on infected cells. Vero cells were infected for 24 h with RSV A2. Cells were labeled live with SBA-Au before being fixed and immunostained for RSV F and RSV G. Again, cells were imaged using darkfield and widefield epifluorescent microscopy. While some background SBA-Au staining is present on the cells, RSV filaments are visibly demarcated in the darkfield channel, indicating that SBA-Au binds RSV G and that gold does not inhibit this binding (Figure 4.2B).

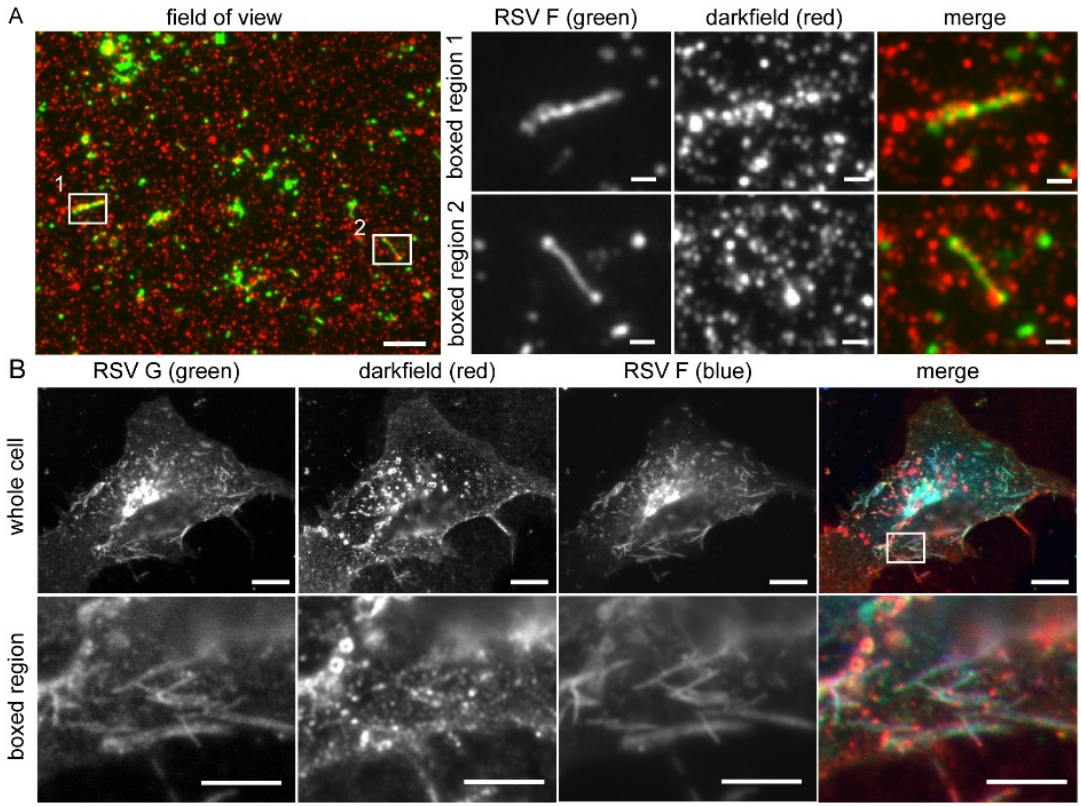

Figure 4.2. SBA-Au labels RSV G. (A) Gold-SBA (red) was incubated with RSV A2 stocks for 30 min before filaments were isolated onto glass coverslips. Isolated virions were fixed and stained for RSV F (green). Cropped regions are indicated by the white boxes. **(B)** Vero cells were infected with RSV A2 for 24 h before RSV G was labeled live with gold-SBA (red). Cells were then fixed and immunostained for RSV F (blue) and RSV G (green). Cropped region is indicated by the white box.

The effect of cell plating density and infection technique on RSV morphology

Since cryoEM requires very thin specimens, the technique requires plating cells in a very sparse manner[29]. First, we assessed the effect of cell plating density on RSV structures. Vero cells were plated at either low or high confluence, infected with RSV A2 for 24 h, and labeled live with SBA-488 immediately prior to fixation. Cells were then immunostained for RSV F and RSV N. Cells infected at high confluence exhibited many long viral filaments composed of RSV G, RSV F, and RSV N. However, cells infected at low confluence had much fewer filaments per cell, and the filaments often did not contain one or more of the stained viral proteins (Figure 4.3). As a first attempt at resolving this issue, we infected confluent cells for 24 h before trypsinizing the cells to lift them off the surface and plating the infected cells at either low or high confluence onto new coverslips. After several hours, cells were labeled with SBA before being immediately fixed and immunostained for RSV F and RSV N. When infected and plated in this manner, long RSV filaments were visible that contained all of the stained RSV proteins, as expected (Figure 4.3). These infection and plating conditions should be further assessed and used in future cryoEM experiments.

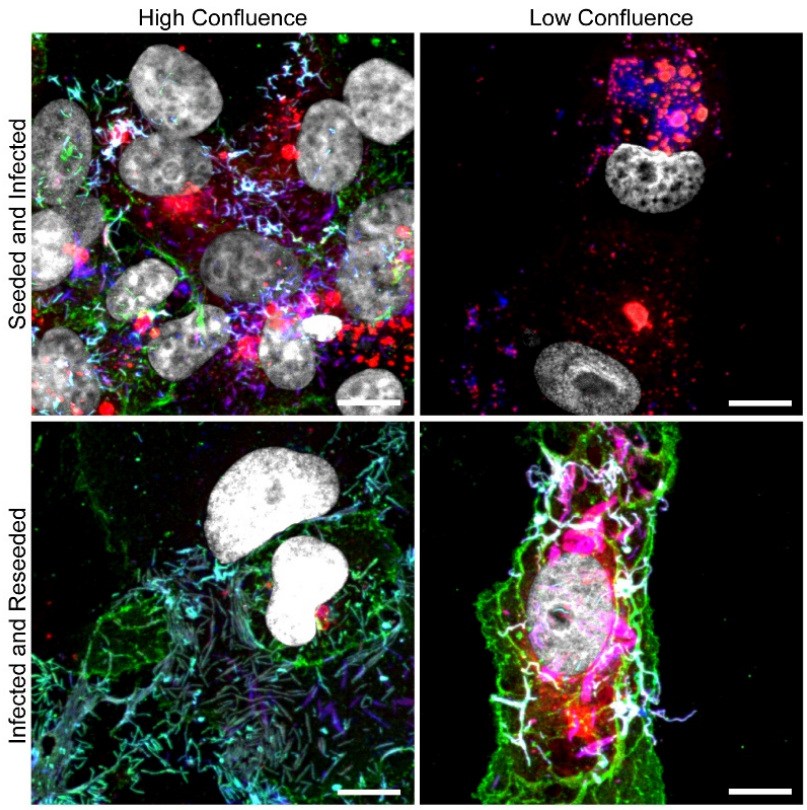

Figure 4.3. Reseeding RSV infected cells preserves prototypical RSV structures. (TOP) Vero cells were plated at high and low density and infected for 24 hours with RSV A2 at MOI 1. At 24 hours, cells were either labeled with SBA-488 (green), and fixed and stained for RSV F (blue) and N (red). **(BOTTOM)** Vero cells were plated at high density and infected for 24 hours with RSV A2 at MOI 1. Cells were trypsinized and reseeded at high and low density. After 2 hours, cells were labeled with SBA-488 (green) before being fixed and stained for RSV F (blue) and N (red).

RSV G glycosylation moieties vary by cell type

As mentioned several times already, cryoEM necessitates very thin specimens. In order to accommodate this requirement, certain cell lines are often chosen for having a low average thickness[152]. For RSV, several cell lines have already been evaluated for cryoEM based on permissivity of the virus and thickness[29]. Additionally, glycosylations present on RSV G have been shown to be highly cell type dependent[153]. We assessed the binding of various fluorescent lectin conjugates to RSV G on infected A549 and Beas-2B cells, two cell lines often chosen for RSV work and compatible with cryoEM. Cells were infected with RSV, incubated for 24 h, and stained live with either SBA, helix pomatia agglutinin (HPA), wheat germ agglutinin (WGA), or concanavalin a (ConA), all conjugated to Alexa Fluor 488. Cells were then fixed immediately and imaged. Unlike the Vero and HEp-2 cell tested in Chapter 2, SBA, WGA, and ConA all had high background staining on mock-infected A549 cells, while HPA-488 specifically bound infected cells with minimal background on mock-infected controls (Figure 4.4). When lectin binding to RSV G was analyzed on infected Beas2B cells, all of the tested lectins exhibited high background staining on mock infected cells (data not shown). These data indicate that: 1) glycosylation of viral proteins is highly variable by cell type and 2) HPA conjugates should be used on A549 cells when analyzing RSV G localization using lectin labeling strategies.

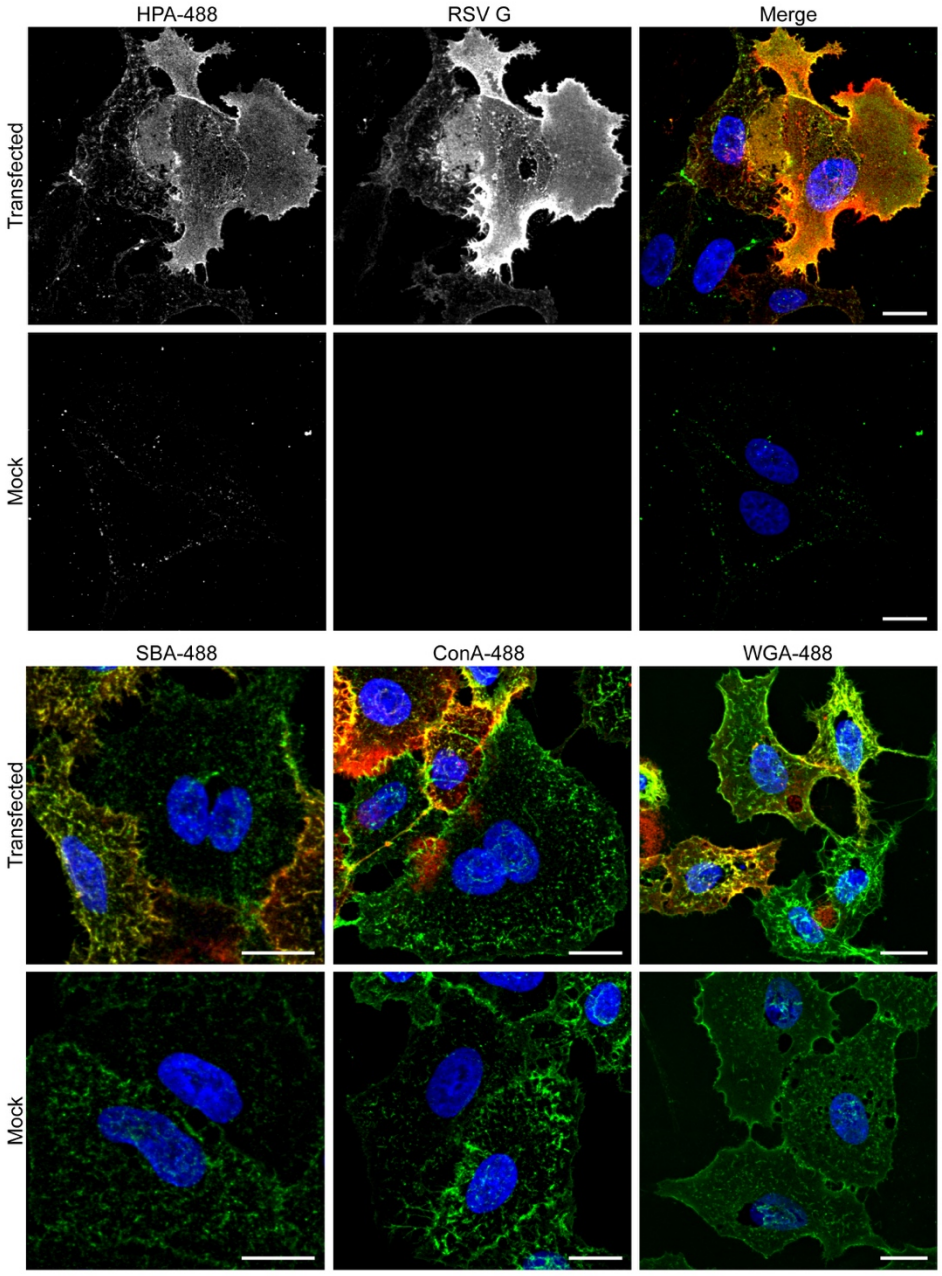

Figure 4.4. HPA-488 specifically bind RSV G on infected A549 cells. A549 cells were infected with RSV A2 for 24 h before being labeled live with the indicated 488-conjugated lectin (green) and fixed. Cells were then immunostained for RSV G (red).

Our methods for adapting lectin labeling to cryoEM techniques should enable single nanometer resolution imaging of RSV G structures in infected cells. The results of these experiments have generated a list of criteria that must be met for cryoEM imaging. First, the lectin-gold conjugate must be pure (as analyzed by HPLC) in order to minimize background due to nonspecific binding. Second, the cell types used in cryoEM imaging of RSV infected cells should be individually tested for lectin binding using a panel of fluorescently conjugated lectins. This will allow selection of a compatible cell type and lectin marker for RSV G labeling. Third, before proceeding to infection staining, cells should be transfected with RSV G and imaged with the selected lectin under cryoEM. This will ensure that the staining is specific with minimal background on untransfected cell lines. Last, the chosen lectin can then be used to image RSV G on infected cells, with discretion used on infection technique to minimize alteration of the progeny virion morphology. Future work could include ensuring the lectin-gold conjugates do not inhibit RSV infectivity or replication as well as ensuring the lectin-gold conjugates are endocytosed in a similar manner to the fluorescent counterparts[154]. Finally, once all lectin-gold conjugate binding verification is complete, cryoEM on both transfected and infected cells could be performed.

By using SBA-488 on live RSV G transfected or RSV infected cells, we will be able to examine the localization of the glycoproteins during infections and in a reduced system. This work opens a new avenue to study the interactions and localizations of RSV G, both in the cytoplasm and at the membrane, with other RSV proteins such as RSV F, RSV N, and RSV M. Additionally, the reduced mRNA-based system could be studied in further detail, with various combinations of viral proteins expressed, in order to examine their individual effect on RSV G localization and trafficking to the plasma membrane. The role of clathrin and caveolar membranes is still actively being studied with regard to RSV replication and assembly[26,154]. Therefore, in both the reduced systems and viral infections, the interactions and localizations of clathrin and caveolin with RSV G can be studied using

dSTORM alongside interaction assays such as proximity ligation assay (PLA), that we have previously utilized[98,120,155–157].

RSV G interactome analysis

Our ability to label RSV G on infected cells and RSV particles also provides the capability to analyze the dynamics of RSV G during all stages of an infection. Additionally, by employing a combination of colocalization analysis, dSTORM, and PLA (proximity ligation assay) interaction assays, we can track the location of RSV G as well as host cell and viral components that interact with RSV G throughout an infection. First, the precise host cell proteins involved in the entry of RSV have been widely debated. By labeling RSV with lectin conjugates, we can investigate the interactions of RSV G with various host cell proteins using the methods discussed above. Confirmatory experiments with drugs to knock down specific pathways could be used to exactly delineate the RSV entry process.

The precise dynamics of RSV G during the replication stages of RSV have never been studied outside of our work here. We showed the RSV G recirculates from the plasma membrane, but the specific proteins and mechanisms involved with incorporating RSV G into mature filaments are not known. Currently, we hypothesize that the switch we observed in colocalization of RSV G from clathrin to caveolae plays a role in this maturation, especially as mature RSV particles contain caveolae[26,154]. Using lectins to label RSV G and investigate these mechanisms using dSTORM and PLA, along with pharmacological knockdown of specific cellular pathways, could answer crucial questions regarding the dynamics of RSV G during the RSV life cycle. By employing dSTORM and PLA to visualize the spatial distribution and interactions of other RSV proteins (such as RSV M, RSV N, RSV F, and RSV M2-1) with each other and with various host cell components, the complete interactome of RSV G and other viral proteins can be mapped across the course of an infection. Moreover, our work on expressing RSV G and RSV F from mRNA can be further expanded upon to help answer these questions in a more

discrete manner. Additional mRNAs encoding for RSV M, RSV N, RSV L, and RSV M2-1 could be easily synthesized. Transfecting cells with one or more of the mRNAs could then answer very important questions regarding the individual actions of each protein. Specifically, expressing RSV G alone or with a combination of other viral structural proteins, such as RSV F or RSV M, and tracking the location of RSV G throughout its production, could help determine if RSV G recycling is independent or if it requires other viral components. Moreover, the interactions of these individual viral proteins can be quantified using PLA independently from a complete viral infection. Using a combination of whole virus and the mRNA reduced system, the interactome of RSV G can be isolated and studied in detail, potentially leading to new therapeutic targets.

mRNA delivered anchored neutralizing antibody prophylaxis and treatment

Finally, we engineered mRNA expressed membrane anchored antibodies that prevent RSV infections in mice lungs. The broad achievement is underscored by several other accomplishments which will be further discussed below: 1) encoding a GPI membrane anchor into antibodies appears to enhance the trafficking of antibodies to the cell surface, 2) mRNA diluted in water can be effectively delivered to epithelial cells at mucosal surfaces, 3) anchoring neutralizing antibodies to the plasma membrane of transfected cells can protect the cell from infection, 4) anchoring antibodies results in increased clearance time, 5) the anchor can be easily encoded to other constructs, and 6) anchoring single-domain VHH camelid antibodies can overcome the single major hurdle of an exceptionally short half-life.

First, we found that mRNA-expressed aPali proceeded to the surface of transfected cells in as little as two hours with intracellular antibody staining becoming undetectable 12 hours post transfection. However, sPali was visible throughout the secretory membrane system across all tested time points, up to the 24 hours post transfection. Since the structure of the GPI anchor acts as a cellular active transport signal

to the plasma membrane, broadly reviewed in Muñiz *et. al.*, this could be further exploited to increase transport of the therapeutic protein to the plasma membrane[158]. Once trafficked to the membrane, the protein could either be retained or cleaved for secretion as necessary depending on the mechanism of action of the therapy, depending the choice of GPI anchor[159].

Second, we found that mRNA diluted in water effectively transfected alveolar cells throughout the lungs of mice. This is a critical observation in the context of storage and "off-the-shelf" availability of future commercially available mRNA therapies. The hypothetical drug could be stored lyophilized in sealed anoxic vials with minimal long-term degradation, even in climates with elevated temperatures[69]. Also, the ability of mRNA to transfect cells *in vivo* via aerosol without a delivery vehicle cannot be understated. Critically, lack on a vehicle should be a boon for safety – while lipid nanoparticles can cause inflammation and long-term liver toxicity, water mixed with mRNA has no such issue[160]. In the case of pulmonary aerosol delivery, this is even more important, as inflammation in the airways of the lung can be life threatening. Additionally, other important mucosal surfaces, such as the female reproductive tract, rectum, and oral cavity, could be tested for efficient transfection of aerosolized mRNA without a delivery vehicle. The delivery of mRNA via aerosol also opens new questions on the mechanisms of droplet-mediated RNA entry. Several aerosol characteristics could be evaluated in order to further optimize gene transfer in the lung epithelium including: droplet size, droplet velocity, and the angle of conical spraying.

Third, we discovered that anchoring neutralizing antibodies to the surface of the cell abrogates viral infection by preventing entry of virions. Broadly neutralizing antibodies are a promising technology in future prophylaxis, but palivizumab represents the only available preventative therapy. While cost is a major factor, repeated injections and a high neutralizing concentration required at the target mucosal surface are substantial

obstacles[161,162]. Linking neutralizing antibodies to the plasma membrane of the target epithelium of a particular virus can provide increased concentration of the antibody at the viral target surface. Clearly, while we demonstrate the effectiveness of anchoring palivizumab, other anchored broadly neutralizing antibodies could be encoded in mRNA and delivered, representing a promising new tool in the future of viral prophylaxis.

Fourth, we found that anchoring antibodies to the plasma membrane limits the diffusion of the antibody away from the surface. This effect results in directly increasing the clearance time of the antibody away from the target membrane of the pathogen. Half-lives of broadly neutralizing antibodies are actively being studied, as longer half-lives directly result in more sustained protection[163]. Anchoring the antibody to the membrane of interest can increase this half-life, as turnover of the GPI anchored protein is limited by cleavage rate (which can be limited as discussed above) and turnover of the membrane, which can be slower than transmembrane domain anchored proteins[159,164]. Dosing size and spacing are two aspects of delivery that must be evaluated with regard to mRNA expression of anchored antibodies. Though neutralizing antibodies can be quite potent, it is unknown exactly how many copies are necessary at the target membrane of a pathogen in order to prevent infection.

Fifth, we were able to easily encode the GPI anchor onto an RSV-neutralizing single domain camelid VHH antibody. The ability to easily adapt the anchor sequence to other constructs opens a multitude of new avenues. Not only can the anchor be used for VHH antibodies, but also neutralizing single-chain variable fragment (scFv) antibodies, which are easily constructed from whole antibodies, allowing for trivial generation of prophylactics from newly discovered broadly neutralizing antibodies. The anchor could also be placed on enzymes or other non-antibody based therapeutics to treat nonviral diseases.

Finally, we demonstrated that expressing the anchored anti-RSV VHH was highly potent at neutralizing RSV infection in mice lungs. VHH antibodies represent a promising new tool in passive immunotherapy because they possess high solubility, are one-tenth the size of whole immunoglobulins, and have extremely high binding kinetics, reviewed in depth by Arbabi-Ghahroudi[165]. However, the small size of VHHs results in incredibly short half-lives, on the order of 30 minutes to a couple of hours[126,127]. Anchoring VHH antibodies to the surface of cells can drastically improve this clearance rate, remedying one of the largest problems with single-domain antibody therapeutics. The use of mRNA expressed anchored VHH-based antibodies also results in two tangential benefits in that 1) only a single mRNA has to be delivered to a cell in order to have a biologically active neutralizing antibody (which also increases the number of mRNA copies per unit mass) and 2) smaller mRNAs are more efficiently translated due to increased ribosome density, increasing both the number of mRNA copies and the amount therapeutic anchored VHH available[121]. Overall, mRNA expressed anchored neutralizing VHHs represent a novel and effective prophylaxis technique.

Concluding remarks

Overall, the work presented here has produced innovative tools to image and prevent RSV infections, providing new targets for future antiviral investigations and an adaptable new method to inhibit RSV infection in the lung. This work, while answering several questions regarding the nature of RSV and mRNA therapeutics, has prompted a number of new questions and new opportunities for future research.

REFERENCES

1. Shi, T. *et al.* Global, regional, and national disease burden estimates of acute lower respiratory infections due to respiratory syncytial virus in young children in 2015: a systematic review and modelling study. *The Lancet* **390,** 946–958 (2017).

2. Krilov, L. R. Respiratory syncytial virus disease: update on treatment and prevention. *Expert Rev. Anti Infect. Ther.* **9,** 27–32 (2011).

3. Farber, H. J. *et al.* Observed Effectiveness of Palivizumab for 29–36-Week Gestation Infants. *Pediatrics* e20160627 (2016). doi:10.1542/peds.2016-0627

4. Johnson, S. *et al.* Development of a humanized monoclonal antibody (MEDI-493) with potent in vitro and in vivo activity against respiratory syncytial virus. *J. Infect. Dis.* **176,** 1215–1224 (1997).

5. Dall'Acqua, W. F., Kiener, P. A. & Wu, H. Properties of Human IgG1s Engineered for Enhanced Binding to the Neonatal Fc Receptor (FcRn). *J. Biol. Chem.* **281,** 23514–23524 (2006).

6. Marcelin, J. R., Wilson, J. W., Razonable, R. R. & Mayo Clinic Hematology/Oncology and Transplant Infectious Diseases Services. Oral ribavirin therapy for respiratory syncytial virus infections in moderately to severely immunocompromised patients. *Transpl. Infect. Dis. Off. J. Transplant. Soc.* **16,** 242–250 (2014).

7. Collins, P. L., Fearns, R. & Graham, B. S. Respiratory Syncytial Virus: Virology, Reverse Genetics, and Pathogenesis of Disease. *Curr. Top. Microbiol. Immunol.* **372,** 3–38 (2013).

8. Brock, S. C., Goldenring, J. R. & Crowe, J. E. Apical recycling systems regulate directional budding of respiratory syncytial virus from polarized epithelial cells. *Proc. Natl. Acad. Sci. U. S. A.* **100,** 15143–15148 (2003).

9. Batonick, M., Wertz, G. W., Batonick, M. & Wertz, G. W. Requirements for Human Respiratory Syncytial Virus Glycoproteins in Assembly and Egress from Infected Cells, Requirements for Human Respiratory Syncytial Virus Glycoproteins in Assembly and Egress from Infected Cells. *Adv. Virol. Adv. Virol.* **2011, 2011,** e343408 (2011).

10. Utley, T. J. *et al.* Respiratory syncytial virus uses a Vps4-independent budding mechanism controlled by Rab11-FIP2. *Proc. Natl. Acad. Sci. U. S. A.* **105,** 10209–10214 (2008).

11. Alonas, E. *et al.* Combining Single RNA Sensitive Probes with Subdiffraction-Limited and Live-Cell Imaging Enables the Characterization of Virus Dynamics in Cells. *ACS Nano* **8,** 302–315 (2014).

12. Shaikh, F. Y. *et al.* Respiratory Syncytial Virus Assembles into Structured Filamentous Virion Particles Independently of Host Cytoskeleton and Related Proteins. *PLoS ONE* **7,** e40826 (2012).

13. Gower, T. L. *et al.* RhoA Signaling Is Required for Respiratory Syncytial Virus-Induced Syncytium Formation and Filamentous Virion Morphology. *J. Virol.* **79,** 5326–5336 (2005).

14. Oomens, A. G. P., Bevis, K. P. & Wertz, G. W. The Cytoplasmic Tail of the Human Respiratory Syncytial Virus F Protein Plays Critical Roles in Cellular Localization of the F Protein and Infectious Progeny Production. *J. Virol.* **80,** 10465–10477 (2006).

15. Roberts, S. R., Compans, R. W. & Wertz, G. W. Respiratory syncytial virus matures at the apical surfaces of polarized epithelial cells. *J. Virol.* **69,** 2667–2673 (1995).

16. Förster, A., Maertens, G. N., Farrell, P. J. & Bajorek, M. Dimerization of Matrix Protein Is Required for Budding of Respiratory Syncytial Virus. *J. Virol.* **89,** 4624–4635 (2015).

17. Shaikh, F. Y. *et al.* A Critical Phenylalanine Residue in the Respiratory Syncytial Virus Fusion Protein Cytoplasmic Tail Mediates Assembly of Internal Viral Proteins into Viral Filaments and Particles. *mBio* **3,** e00270-11 (2012).

18. Mitra, R., Baviskar, P., Duncan-Decocq, R. R., Patel, D. & Oomens, A. G. P. The Human Respiratory Syncytial Virus Matrix Protein Is Required for Maturation of Viral Filaments. *J. Virol.* **86,** 4432–4443 (2012).

19. McPhee, H. K. *et al.* Influence of Lipids on the Interfacial Disposition of Respiratory Syncytical Virus Matrix Protein. *Langmuir* **27,** 304–311 (2011).

20. Norrby, E., Marusyk, H. & Örvell, C. Morphogenesis of Respiratory Syncytial Virus in a Green Monkey Kidney Cell Line (Vero). *J. Virol.* **6,** 237–242 (1970).

21. Arslańagic, E. *et al.* Maturation of respiratory syncytial virus within HEp-2 cell cytoplasm. *Acta Virol.* **40,** 209–214 (1996).

22. Radhakrishnan, A. *et al.* Protein Analysis of Purified Respiratory Syncytial Virus Particles Reveals an Important Role for Heat Shock Protein 90 in Virus Particle Assembly. *Mol. Cell. Proteomics MCP* **9,** 1829–1848 (2010).

23. Kallewaard, N. L., Bowen, A. L. & Crowe Jr., J. E. Cooperativity of actin and microtubule elements during replication of respiratory syncytial virus. *Virology* **331,** 73–81 (2005).

24. Jeffree, C. E. *et al.* Ultrastructural analysis of the interaction between F-actin and respiratory syncytial virus during virus assembly. *Virology* **369,** 309–323 (2007).

25. Santangelo, P. J. & Bao, G. Dynamics of filamentous viral RNPs prior to egress. *Nucleic Acids Res.* **35,** 3602–3611 (2007).

26. Ludwig, A. *et al.* Caveolae provide a specialized membrane environment for respiratory syncytial virus assembly. *J. Cell Sci.* **130,** 1037–1050 (2017).

27. Bajorek, M. *et al.* The Thr205 Phosphorylation Site within Respiratory Syncytial Virus Matrix (M) Protein Modulates M Oligomerization and Virus Production. *J. Virol.* **88,** 6380–6393 (2014).

28. McCurdy, L. H. & Graham, B. S. Role of Plasma Membrane Lipid Microdomains in Respiratory Syncytial Virus Filament Formation. *J. Virol.* **77,** 1747–1756 (2003).

29. Hampton, C. M. *et al.* Correlated fluorescence microscopy and cryo-electron tomography of virus-infected or transfected mammalian cells. *Nat. Protoc.* **12,** 150–167 (2017).

30. Croset, A. *et al.* Differences in the glycosylation of recombinant proteins expressed in HEK and CHO cells. *J. Biotechnol.* **161,** 336–348 (2012).

31. Schermelleh, L., Heintzmann, R. & Leonhardt, H. A guide to super-resolution fluorescence microscopy. *J. Cell Biol.* **190,** 165–175 (2010).

32. Schnell, U., Dijk, F., Sjollema, K. A. & Giepmans, B. N. G. Immunolabeling artifacts and the need for live-cell imaging. *Nat. Methods* **9,** 152 (2012).

33. Merk, A. *et al.* Breaking Cryo-EM Resolution Barriers to Facilitate Drug Discovery. *Cell* **165,** 1698–1707 (2016).

34. Linde, S. van de *et al.* Direct stochastic optical reconstruction microscopy with standard fluorescent probes. *Nat. Protoc.* **6,** 991 (2011).

35. Hemmi, H. *et al.* A Toll-like receptor recognizes bacterial DNA. *Nature* **408,** 740–745 (2000).

36. Ahmad-Nejad, P. *et al.* Bacterial CpG-DNA and lipopolysaccharides activate Toll-like receptors at distinct cellular compartments. *Eur. J. Immunol.* **32,** 1958–1968 (2002).

37. Yasuda, K. *et al.* Requirement for DNA CpG Content in TLR9-Dependent Dendritic Cell Activation Induced by DNA-Containing Immune Complexes. *J. Immunol.* **183,** 3109–3117 (2009).

38. Latz, E. *et al.* Ligand-induced conformational changes allosterically activate Toll-like receptor 9. *Nat. Immunol.* **8,** 772–779 (2007).

39. Ledwith, B. J. *et al.* Plasmid DNA vaccines: investigation of integration into host cellular DNA following intramuscular injection in mice. *Intervirology* **43,** 258–272 (2000).

40. Manam, S. *et al.* Plasmid DNA vaccines: tissue distribution and effects of DNA sequence, adjuvants and delivery method on integration into host DNA. *Intervirology* **43,** 273–281 (2000).

41. Jäschke, A. & Helm, M. RNA sex. *Chem. Biol.* **10,** 1148–1150 (2003).

42. Chetverin, A. B. Replicable and recombinogenic RNAs. *FEBS Lett.* **567,** 35–41 (2004).

43. Ishii, K., R Weiss, W., Ichino, M., Verthelyi, D. & M Klinman, D. *Activity and safety of DNA plasmids encoding IL-4 and IFN gamma*. **6,** (1999).

44. MacColl, G., Bunn, C., Goldspink, G., Bouloux, P. & Górecki, D. C. Intramuscular plasmid DNA injection can accelerate autoimmune responses. *Gene Ther.* **8,** 1354–1356 (2001).

45. Sellins, K., Fradkin, L., Liggitt, D. & Dow, S. Type I interferons potently suppress gene expression following gene delivery using liposome(-)DNA complexes. *Mol. Ther. J. Am. Soc. Gene Ther.* **12,** 451–459 (2005).

46. Zhang, J.-S., Liu, F. & Huang, L. Implications of pharmacokinetic behavior of lipoplex for its inflammatory toxicity. *Adv. Drug Deliv. Rev.* **57,** 689–698 (2005).

47. Gautam, A., Densmore, C. L. & Waldrep, J. C. Pulmonary cytokine responses associated with PEI-DNA aerosol gene therapy. *Gene Ther.* **8,** 254–257 (2001).

48. Sakurai, F. *et al.* The role of tissue macrophages in the induction of proinflammatory cytokine production following intravenous injection of lipoplexes. *Gene Ther.* **9,** 1120–1126 (2002).

49. Conry, R. M. *et al.* Characterization of a messenger RNA polynucleotide vaccine vector. *Cancer Res.* **55,** 1397–1400 (1995).

50. Hoerr, I., Obst, R., Rammensee, H. G. & Jung, G. In vivo application of RNA leads to induction of specific cytotoxic T lymphocytes and antibodies. *Eur. J. Immunol.* **30,** 1–7 (2000).

51. Probst, J. *et al.* Spontaneous cellular uptake of exogenous messenger RNA in vivo is nucleic acid-specific, saturable and ion dependent. *Gene Ther.* **14,** 1175–1180 (2007).

52. Merten, O.-W., Gény-Fiamma, C. & Douar, A. M. Current issues in adeno-associated viral vector production. *Gene Ther.* **12,** S51–S61 (2005).

53. Schnepp, B. C., Jensen, R. L., Chen, C.-L., Johnson, P. R. & Clark, K. R. Characterization of Adeno-Associated Virus Genomes Isolated from Human Tissues. *J. Virol.* **79,** 14793–14803 (2005).

54. Zaiss, A.-K. *et al.* Differential activation of innate immune responses by adenovirus and adeno-associated virus vectors. *J. Virol.* **76,** 4580–4590 (2002).

55. McCaffrey, A. P. *et al.* The Host Response to Adenovirus, Helper-dependent Adenovirus, and Adeno-associated Virus in Mouse Liver. *Mol. Ther.* **16,** 931–941 (2008).

56. Lin, J. *et al.* A New Genetic Vaccine Platform Based on an Adeno-Associated Virus Isolated from a Rhesus Macaque. *J. Virol.* **83,** 12738–12750 (2009).

57. Cottard, V. *et al.* Immune Response Against Gene Therapy Vectors: Influence of Synovial Fluid on Adeno-Associated Virus Mediated Gene Transfer to Chondrocytes. *J. Clin. Immunol.* **24,** 162–169 (2004).

58. Peden, C. S., Burger, C., Muzyczka, N. & Mandel, R. J. Circulating Anti-Wild-Type Adeno-Associated Virus Type 2 (AAV2) Antibodies Inhibit Recombinant AAV2

(rAAV2)-Mediated, but Not rAAV5-Mediated, Gene Transfer in the Brain. *J. Virol.* **78,** 6344–6359 (2004).

59. Calcedo, R., Vandenberghe, L. H., Gao, G., Lin, J. & Wilson, J. M. Worldwide Epidemiology of Neutralizing Antibodies to Adeno-Associated Viruses. *J. Infect. Dis.* **199,** 381–390 (2009).

60. Scallan, C. D. *et al.* Human immunoglobulin inhibits liver transduction by AAV vectors at low AAV2 neutralizing titers in SCID mice. *Blood* **107,** 1810–1817 (2006).

61. Alexopoulou, L., Holt, A. C., Medzhitov, R. & Flavell, R. A. Recognition of double-stranded RNA and activation of NF-κB by Toll-like receptor 3. *Nature* **413,** 732–738 (2001).

62. Diebold, S. S., Kaisho, T., Hemmi, H., Akira, S. & Sousa, C. R. e. Innate Antiviral Responses by Means of TLR7-Mediated Recognition of Single-Stranded RNA. *Science* **303,** 1529–1531 (2004).

63. Heil, F. *et al.* Species-Specific Recognition of Single-Stranded RNA via Toll-like Receptor 7 and 8. *Science* **303,** 1526–1529 (2004).

64. Hornung, V. *et al.* 5'-Triphosphate RNA Is the Ligand for RIG-I. *Science* **314,** 994–997 (2006).

65. Anderson, B. R. *et al.* Incorporation of pseudouridine into mRNA enhances translation by diminishing PKR activation. *Nucleic Acids Res.* **38,** 5884–5892 (2010).

66. Karikó, K., Buckstein, M., Ni, H. & Weissman, D. Suppression of RNA Recognition by Toll-like Receptors: The Impact of Nucleoside Modification and the Evolutionary Origin of RNA. *Immunity* **23,** 165–175 (2005).

67. Karikó, K. *et al.* Incorporation of Pseudouridine Into mRNA Yields Superior Nonimmunogenic Vector With Increased Translational Capacity and Biological Stability. *Mol. Ther. J. Am. Soc. Gene Ther.* **16,** 1833–1840 (2008).

68. Ponsaerts, P., Van Tendeloo, V. F. I. & Berneman, Z. N. Cancer immunotherapy using RNA-loaded dendritic cells. *Clin. Exp. Immunol.* **134,** 378–384 (2003).

69. Bonnet, J. *et al.* Chain and conformation stability of solid-state DNA: implications for room temperature storage. *Nucleic Acids Res.* **38,** 1531–1546 (2010).

70. Kormann, M. S. D. *et al.* Expression of therapeutic proteins after delivery of chemically modified mRNA in mice. *Nat. Biotechnol.* **29,** 154–157 (2011).

71. Mahiny, A. J. *et al.* In vivo genome editing using nuclease-encoding mRNA corrects SP-B deficiency. *Nat. Biotechnol.* **33,** 584–586 (2015).

72. Mays, L. E. *et al.* Modified *Foxp3* mRNA protects against asthma through an IL-10–dependent mechanism. *J. Clin. Invest.* **123,** 1216–1228 (2013).

73. Nair, H. *et al.* Global burden of acute lower respiratory infections due to respiratory syncytial virus in young children: a systematic review and meta-analysis. *Lancet* **375,** 1545–1555 (2010).

74. Levine, S. Polypeptides of respiratory syncytial virus. *J. Virol.* **21,** 427–431 (1977).

75. Levine, S., Klaiber-Franco, R. & Paradiso, P. R. Demonstration that glycoprotein G is the attachment protein of respiratory syncytial virus. *J. Gen. Virol.* **68 (Pt 9),** 2521–2524 (1987).

76. McLellan, J. S., Ray, W. C. & Peeples, M. E. Structure and Function of RSV Surface Glycoproteins. *Curr. Top. Microbiol. Immunol.* **372,** 83–104 (2013).

77. Karron, R. A. *et al.* Respiratory syncytial virus (RSV) SH and G proteins are not essential for viral replication in vitro: Clinical evaluation and molecular characterization of a cold-passaged, attenuated RSV subgroup B mutant. *Proc. Natl. Acad. Sci. U. S. A.* **94,** 13961–13966 (1997).

78. Techaarpornkul, S., Barretto, N. & Peeples, M. E. Functional Analysis of Recombinant Respiratory Syncytial Virus Deletion Mutants Lacking the Small Hydrophobic and/or Attachment Glycoprotein Gene. *J. Virol.* **75,** 6825–6834 (2001).

79. Henderson, G., Murray, J. & Yeo, R. P. Sorting of the Respiratory Syncytial Virus Matrix Protein into Detergent-Resistant Structures Is Dependent on Cell-Surface Expression of the Glycoproteins. *Virology* **300,** 244–254 (2002).

80. Ghildyal, R. *et al.* Interaction between the respiratory syncytial virus G glycoprotein cytoplasmic domain and the matrix protein. *J. Gen. Virol.* **86,** 1879–1884 (2005).

81. Gutiérrez-Ortega, A., Sánchez-Hernández, C. & Gómez-García, B. Respiratory syncytial virus glycoproteins uptake occurs through clathrin-mediated endocytosis in a human epithelial cell line. *Virol. J.* **5,** 127 (2008).

82. Kolokoltsov, A. A. *et al.* Small Interfering RNA Profiling Reveals Key Role of Clathrin-Mediated Endocytosis and Early Endosome Formation for Infection by Respiratory Syncytial Virus. *J. Virol.* **81,** 7786–7800 (2007).

83. Brown, G., Rixon, H. W. M. & Sugrue, R. J. Caveolin-1 is incorporated into mature respiratory syncytial virus particles during virus assembly on the surface of virus-infected cells. *J. Gen. Virol.* **83,** 611–621 (2002).

84. Corry, J., Johnson, S. M., Cornwell, J. & Peeples, M. E. Preventing Cleavage of the Respiratory Syncytial Virus Attachment Protein in Vero Cells Rescues the Infectivity of Progeny Virus for Primary Human Airway Cultures. *J. Virol.* **90,** 1311–1320 (2016).

85. Jeffree, C. E., Rixon, H. W. M. L., Brown, G., Aitken, J. & Sugrue, R. J. Distribution of the attachment (G) glycoprotein and GM1 within the envelope of mature respiratory syncytial virus filaments revealed using field emission scanning electron microscopy. *Virology* **306,** 254–267 (2003).

86. Collins, P. L. & Mottet, G. Oligomerization and post-translational processing of glycoprotein G of human respiratory syncytial virus: altered O-glycosylation in the presence of brefeldin A. *J. Gen. Virol.* **73,** 849–863 (1992).

87. Low, K.-W., Tan, T., Ng, K., Tan, B.-H. & Sugrue, R. J. The RSV F and G glycoproteins interact to form a complex on the surface of infected cells. *Biochem. Biophys. Res. Commun.* **366,** 308–313 (2008).

88. Warren, L. *et al.* Highly efficient reprogramming to pluripotency and directed differentiation of human cells using synthetic modified mRNA. *Cell Stem Cell* **7,** 618–630 (2010).

89. Huang, K., Incognito, L., Cheng, X., Ulbrandt, N. D. & Wu, H. Respiratory Syncytial Virus-Neutralizing Monoclonal Antibodies Motavizumab and Palivizumab Inhibit Fusion. *J. Virol.* **84,** 8132–8140 (2010).

90. Chen, M. *et al.* A flow cytometry based assay to assess RSV specific neutralizing antibody is reproducible, efficient and accurate. *J. Immunol. Methods* **362,** 180–184 (2010).

91. Hallak, L. K., Collins, P. L., Knudson, W. & Peeples, M. E. Iduronic Acid-Containing Glycosaminoglycans on Target Cells Are Required for Efficient Respiratory Syncytial Virus Infection. *Virology* **271,** 264–275 (2000).

92. Ma, S. & Chisholm, R. L. Cytoplasmic dynein-associated structures move bidirectionally in vivo. *J. Cell Sci.* **115,** 1453–1460 (2002).

93. Lifland, A. W., Zurla, C., Yu, J. & Santangelo, P. J. Dynamics of Native β-actin mRNA Transport in the Cytoplasm. *Traffic* **12,** 1000–1011 (2011).

94. Cai, D., McEwen, D. P., Martens, J. R., Meyhofer, E. & Verhey, K. J. Single Molecule Imaging Reveals Differences in Microtubule Track Selection Between Kinesin Motors. *PLoS Biol* **7,** e1000216 (2009).

95. Cai, D., Verhey, K. J. & Meyhöfer, E. Tracking Single Kinesin Molecules in the Cytoplasm of Mammalian Cells. *Biophys. J.* **92,** 4137–4144 (2007).

96. Shaikh, F. Y. & Crowe, J. E. Molecular mechanisms driving respiratory syncytial virus assembly. *Future Microbiol.* **8,** 123–131 (2013).

97. Santangelo, P. J. *et al.* Single molecule–sensitive probes for imaging RNA in live cells. *Nat. Methods* **6,** 347–349 (2009).

98. Lifland, A. W. *et al.* Human Respiratory Syncytial Virus Nucleoprotein and Inclusion Bodies Antagonize the Innate Immune Response Mediated by MDA5 and MAVS. *J. Virol.* **86,** 8245–8258 (2012).

99. Popa, A. *et al.* Residues in the Hendra Virus Fusion Protein Transmembrane Domain Are Critical for Endocytic Recycling. *J. Virol.* **86,** 3014–3026 (2012).

100. Vogt, C., Eickmann, M., Diederich, S., Moll, M. & Maisner, A. Endocytosis of the Nipah Virus Glycoproteins. *J. Virol.* **79,** 3865–3872 (2005).

101. Leser, G. P., Ector, K. J. & Lamb, R. A. The paramyxovirus simian virus 5 hemagglutinin-neuraminidase glycoprotein, but not the fusion glycoprotein, is internalized via coated pits and enters the endocytic pathway. *Mol. Biol. Cell* **7,** 155–172 (1996).

102. Leser, G. P., Ector, K. J., Ng, D. T. W., Shaughnessy, M. A. & Lamb, R. A. The Signal for Clathrin-Mediated Endocytosis of the Paramyxovirus SV5 HN Protein Resides at the Transmembrane Domain–Ectodomain Boundary Region. *Virology* **262,** 79–92 (1999).

103. Ravid, D., Leser, G. P. & Lamb, R. A. A Role for Caveolin 1 in Assembly and Budding of the Paramyxovirus Parainfluenza Virus 5. *J. Virol.* **84,** 9749–9759 (2010).

104. Bruce, E. A., Digard, P. & Stuart, A. D. The Rab11 Pathway Is Required for Influenza A Virus Budding and Filament Formation. *J. Virol.* **84,** 5848–5859 (2010).

105. Bruce, E. A., Stuart, A., McCaffrey, M. W. & Digard, P. Role of the Rab11 pathway in negative-strand virus assembly. *Biochem. Soc. Trans.* **40,** 1409–1415 (2012).

106. Lin, S. X., Gundersen, G. G. & Maxfield, F. R. Export from Pericentriolar Endocytic Recycling Compartment to Cell Surface Depends on Stable, Detyrosinated (Glu) Microtubules and Kinesin. *Mol. Biol. Cell* **13,** 96–109 (2002).

107. Boukhvalova, M. S., Prince, G. A. & Blanco, J. C. G. Respiratory Syncytial Virus Infects and Abortively Replicates in the Lungs in Spite of Preexisting Immunity. *J. Virol.* **81,** 9443–9450 (2007).

108. Richner, J. M. *et al.* Modified mRNA Vaccines Protect against Zika Virus Infection. *Cell* **168,** 1114-1125.e10 (2017).

109. Pardi, N. *et al.* Administration of nucleoside-modified mRNA encoding broadly neutralizing antibody protects humanized mice from HIV-1 challenge. *Nat. Commun.* **8,** 14630 (2017).

110. Petsch, B. *et al.* Protective efficacy of *in vitro* synthesized, specific mRNA vaccines against influenza A virus infection. *Nat. Biotechnol.* **30,** nbt.2436 (2012).

111. Hekele, A. *et al.* Rapidly produced SAM® vaccine against H7N9 influenza is immunogenic in mice. *Emerg. Microbes Infect.* **2,** e52 (2013).

112. Brito, L. A. *et al.* A Cationic Nanoemulsion for the Delivery of Next-generation RNA Vaccines. *Mol. Ther.* **22,** 2118–2129 (2014).

113. Bogers, W. M. *et al.* Potent Immune Responses in Rhesus Macaques Induced by Nonviral Delivery of a Self-amplifying RNA Vaccine Expressing HIV Type 1 Envelope With a Cationic Nanoemulsion. *J. Infect. Dis.* **211,** 947–955 (2015).

114. Geall, A. J., Mandl, C. W. & Ulmer, J. B. RNA: The new revolution in nucleic acid vaccines. *Semin. Immunol.* **25,** 152–159 (2013).

115. Probst, J. *et al.* Messenger RNA Vaccines. *SpringerLink* 223–245 (2012). doi:10.1007/978-3-7091-0439-2_11

116. Schlake, T., Thess, A., Fotin-Mleczek, M. & Kallen, K.-J. Developing mRNA-vaccine technologies. *RNA Biol.* **9,** 1319 (2012).

117. Du, Y., Pattnaik, A. K., Song, C., Yoo, D. & Li, G. Glycosyl-phosphatidylinositol (GPI)-anchored membrane association of the porcine reproductive and respiratory syndrome virus GP4 glycoprotein and its co-localization with CD163 in lipid rafts. *Virology* **424,** 18–32 (2012).

118. Nickells, M. W., Alvarez, J. I., Lublin, D. M. & Atkinson, J. P. Characterization of DAF-2, a high molecular weight form of decay-accelerating factor (DAF; CD55), as a covalently cross-linked dimer of DAF-1. *J. Immunol. Baltim. Md 1950* **152,** 676–685 (1994).

119. Rossey, I. *et al.* Potent single-domain antibodies that arrest respiratory syncytial virus fusion protein in its prefusion state. *Nat. Commun.* **8,** ncomms14158 (2017).

120. Kirschman, J. L. *et al.* Characterizing exogenous mRNA delivery, trafficking, cytoplasmic release and RNA-protein correlations at the level of single cells. *Nucleic Acids Res.* (2017). doi:10.1093/nar/gkx290

121. Hendrickson, D. G. *et al.* Concordant Regulation of Translation and mRNA Abundance for Hundreds of Targets of a Human microRNA. *PLOS Biol.* **7,** e1000238 (2009).

122. Varkouhi, A. K., Scholte, M., Storm, G. & Haisma, H. J. Endosomal escape pathways for delivery of biologicals. *J. Control. Release Off. J. Control. Release Soc.* **151,** 220–228 (2011).

123. Juliano, R. L. & Carver, K. Cellular Uptake and Intracellular Trafficking of Oligonucleotides. *Adv. Drug Deliv. Rev.* **87,** 35–45 (2015).

124. Li, F. *et al.* Construction and development of a mammalian cell-based full-length antibody display library for targeting hepatocellular carcinoma. *Appl. Microbiol. Biotechnol.* **96,** 1233–1241 (2012).

125. Wen, M. *et al.* GPI-anchored single chain Fv - an effective way to capture transiently-exposed neutralization epitopes on HIV-1 envelope spike. *Retrovirology* **7,** 79 (2010).

126. Harmsen, M. M. & De Haard, H. J. Properties, production, and applications of camelid single-domain antibody fragments. *Appl. Microbiol. Biotechnol.* **77,** 13–22 (2007).

127. Coppieters, K. *et al.* Formatted anti–tumor necrosis factor α VHH proteins derived from camelids show superior potency and targeting to inflamed joints in a murine model of collagen-induced arthritis. *Arthritis Rheum.* **54,** 1856–1866 (2006).

128. Harmsen, M. M., Van Solt, C. B., Fijten, H. P. D. & Van Setten, M. C. Prolonged in vivo residence times of llama single-domain antibody fragments in pigs by binding to porcine immunoglobulins. *Vaccine* **23,** 4926–4934 (2005).

129. Hessell, A. J. *et al.* Fc receptor but not complement binding is important in antibody protection against HIV. *Nature* **449,** 101–104 (2007).

130. Bournazos, S. *et al.* Broadly neutralizing anti-HIV-1 antibodies require Fc effector functions for in vivo activity. *Cell* **158,** 1243–1253 (2014).

131. Bournazos, S., Chow, S.-K., Abboud, N., Casadevall, A. & Ravetch, J. V. Human IgG Fc domain engineering enhances antitoxin neutralizing antibody activity. *J. Clin. Invest.* **124,** 725–729 (2014).

132. DiLillo, D. J., Tan, G. S., Palese, P. & Ravetch, J. V. Broadly neutralizing hemagglutinin stalk-specific antibodies require FcγR interactions for protection against influenza virus in vivo. *Nat. Med.* **20,** 143–151 (2014).

133. Schuster, J. E. *et al.* A Broadly Neutralizing Human Monoclonal Antibody Exhibits In Vivo Efficacy Against Both Human Metapneumovirus and Respiratory Syncytial Virus. *J. Infect. Dis.* **211,** 216–225 (2015).

134. Medof, M. E. *et al.* Cloning and characterization of cDNAs encoding the complete sequence of decay-accelerating factor of human complement. *Proc. Natl. Acad. Sci.* **84,** 2007–2011 (1987).

135. Mentel, R., Wegner, U., Bruns, R. & Gürtler, L. Real-time PCR to improve the diagnosis of respiratory syncytial virus infection. *J. Med. Microbiol.* **52,** 893–896 (2003).

136. Hardy, C. L. *et al.* Inert 50-nm Polystyrene Nanoparticles That Modify Pulmonary Dendritic Cell Function and Inhibit Allergic Airway Inflammation. *J. Immunol.* **188,** 1431–1441 (2012).

137. Barletta, K. E. *et al.* Leukocyte compartments in the mouse lung: Distinguishing between marginated, interstitial, and alveolar cells in response to injury. *J. Immunol. Methods* **375,** 100–110 (2012).

138. Koning, R. I. *et al.* Correlative cryo-fluorescence light microscopy and cryo-electron tomography of Streptomyces. *Methods Cell Biol.* **124,** 217–239 (2014).

139. Kahn, J. S., Schnell, M. J., Buonocore, L. & Rose, J. K. Recombinant vesicular stomatitis virus expressing respiratory syncytial virus (RSV) glycoproteins: RSV fusion protein can mediate infection and cell fusion. *Virology* **254,** 81–91 (1999).

140. Srinivasakumar, N., Ogra, P. L. & Flanagan, T. D. Characteristics of fusion of respiratory syncytial virus with HEp-2 cells as measured by R18 fluorescence dequenching assay. *J. Virol.* **65,** 4063–4069 (1991).

141. San-Juan-Vergara, H. *et al.* Cholesterol-rich microdomains as docking platforms for respiratory syncytial virus in normal human bronchial epithelial cells. *J. Virol.* **86,** 1832–1843 (2012).

142. Krzyzaniak, M. A., Zumstein, M. T., Gerez, J. A., Picotti, P. & Helenius, A. Host cell entry of respiratory syncytial virus involves macropinocytosis followed by proteolytic activation of the F protein. *PLoS Pathog.* **9,** e1003309 (2013).

143. Rust, M. J., Bates, M. & Zhuang, X. Sub-diffraction-limit imaging by stochastic optical reconstruction microscopy (STORM). *Nat. Methods* **3,** 793 (2006).

144. Hess, S. T., Girirajan, T. P. K. & Mason, M. D. Ultra-High Resolution Imaging by Fluorescence Photoactivation Localization Microscopy. *Biophys. J.* **91,** 4258–4272 (2006).

145. Dempsey, G. T., Vaughan, J. C., Chen, K. H., Bates, M. & Zhuang, X. Evaluation of fluorophores for optimal performance in localization-based super-resolution imaging. *Nat. Methods* **8,** 1027–1036 (2011).

146. Juette, M. F. *et al.* Three-dimensional sub–100 nm resolution fluorescence microscopy of thick samples. *Nat. Methods* **5,** 527 (2008).

147. Jiménez, N. & Post, J. A. A Novel Approach for Intracellular 3D Immuno-Labeling for Electron Tomography. *Traffic* **13,** 926–933 (2012).

148. Lebbink, M. N. *et al.* Spiral Coating of the Endothelial Caveolar Membranes as Revealed by Electron Tomography and Template Matching. *Traffic* **11,** 138–150 (2010).

149. McDonald, K. Cryopreparation Methods for Electron Microscopy of Selected Model Systems. *Methods Cell Biol.* **79,** 23–56 (2007).

150. Murk, J. L. a. N. *et al.* Influence of aldehyde fixation on the morphology of endosomes and lysosomes: quantitative analysis and electron tomography. *J. Microsc.* **212,** 81–90 (2003).

151. Hoenger, A. High-resolution cryo-electron microscopy on macromolecular complexes and cell organelles. *Protoplasma* **251,** 417–427 (2014).

152. Strauss, J. D. *et al.* Three-Dimensional Structural Characterization of HIV-1 Tethered to Human Cells. *J. Virol.* **90,** 1507–1521 (2016).

153. García-Beato, R. *et al.* Host cell effect upon glycosylation and antigenicity of human respiratory syncytial virus G glycoprotein. *Virology* **221,** 301–309 (1996).

154. Vanover, D. *et al.* RSV glycoprotein and genomic RNA dynamics reveal filament assembly prior to the plasma membrane. *Nat. Commun.* **8,** 667 (2017).

155. Jung, J., Lifland, A. W., Zurla, C., Alonas, E. J. & Santangelo, P. J. Quantifying RNA-protein interactions in situ using modified-MTRIPs and proximity ligation. *Nucleic Acids Res.* **41,** e12 (2013).

156. Jung, J., Lifland, A. W., Alonas, E. J., Zurla, C. & Santangelo, P. J. Characterization of mRNA-cytoskeleton interactions in situ using FMTRIP and proximity ligation. *PloS One* **8,** e74598 (2013).

157. Kiss, G. *et al.* Structural Analysis of Respiratory Syncytial Virus Reveals the Position of M2-1 between the Matrix Protein and the Ribonucleoprotein Complex. *J. Virol.* **88,** 7602–7617 (2014).

158. Muñiz, M. & Riezman, H. Trafficking of glycosylphosphatidylinositol anchored proteins from the endoplasmic reticulum to the cell surface. *J. Lipid Res.* **57,** 352–360 (2016).

159. Müller, A., Klöppel, C., Smith-Valentine, M., Van Houten, J. & Simon, M. Selective and programmed cleavage of GPI-anchored proteins from the surface membrane by phospholipase C. *Biochim. Biophys. Acta* **1818,** 117–124 (2012).

160. Zatsepin, T. S., Kotelevtsev, Y. V. & Koteliansky, V. Lipid nanoparticles for targeted siRNA delivery – going from bench to bedside. *Int. J. Nanomedicine* **11,** 3077–3086 (2016).

161. McKinley, S. A. *et al.* Modeling Neutralization Kinetics of HIV by Broadly Neutralizing Monoclonal Antibodies in Genital Secretions Coating the Cervicovaginal Mucosa. *PLOS ONE* **9,** e100598 (2014).

162. Brandenberg, O. F. *et al.* Predicting HIV-1 transmission and antibody neutralization efficacy in vivo from stoichiometric parameters. *PLoS Pathog.* **13,** (2017).

163. Sievers, S. A., Scharf, L., West, A. P. & Bjorkman, P. J. Antibody engineering for increased potency, breadth and half-life. *Curr. Opin. HIV AIDS* **10,** 151–159 (2015).

164. Karabasheva, D., Cole, N. B. & Donaldson, J. G. Roles for Trafficking and O-Linked Glycosylation in the Turnover of Model Cell Surface Proteins. *J. Biol. Chem.* **289,** 19477–19490 (2014).

165. Arbabi-Ghahroudi, M. Camelid Single-Domain Antibodies: Historical Perspective and Future Outlook. *Front. Immunol.* **8,** 1589 (2017).